THE EFFECTS OF MITRAL ANNULAR DYNAMICS AND PAPILLARY MUSCLE POSITION ON CHORDAL FORCE DISTRIBUTION AND VALVE FUNCTION: *AN IN VITRO STUDY*

A Thesis
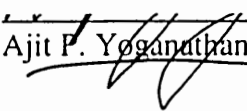Presented to
The Academic Faculty

by

Jorge Hernan Jimenez Mejia

In Partial Fulfillment
of the Requirements for the Degree
Master of Science in Bioengineering
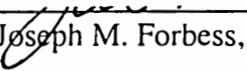
Georgia Institute of Technology

November 2003

THE EFFECTS OF MITRAL ANNULAR DYNAMICS AND PAPILLARY MUSCLE POSITION ON CHORDAL FORCE DISTRIBUTION AND VALVE FUNCTION: *AN IN VITRO STUDY*

Approved:

Ajit P. Yoganathan, Ph.D.

Raymond P. Vito, Ph.D.

Joseph M. Forbess, M.D.

Date Approved: 11/24/03

A la familia, lo mas importante en la vida.

A aquellos amigos que son como hermanos.

ACKNOWLEDGEMENTS

TABLE OF CONTENTS

LIST OF TABLES

LIST OF FIGURES

ABBREVIATIONS

Abbreviation	Definition
MV	Mitral Valve
PM	Papillary Muscle
CO	Cardiac Output
PST	Peak Systolic Tension
MR	Mitral Regurgitation
CDV	Cardiovascular Disease
EDV	End Diastolic Volume
ESV	End Systolic Volume
HR	Heart Rate
APM	Anterolateral Papillary Muscle
PPM	Posteromedial Papillary Muscle
TEE	Trans-Esophagic Echocardiography
FMR	Functional Mitral Regurgitation
MS	Mitral Stenosis
VASAC	Variable Annular Shape Atrial Chamber
CTT	Chordae Tendineae Tension
2D	2-Dimensional
3D	3-Dimensional
SG	Strain Gauge

SUMMARY

Changes in annular geometry and dynamics (2D-area, 2D-perimeter, saddle curvature, and annular displacement) have been observed in patients with functional mitral regurgitation, acute ischemic mitral regurgitation, and different types of cardiomyopathies. In addition, ventricular dilation and sphericity, papillary muscle (PM) contractile malfunction, and abnormal motions of the left ventricle are conditions (associated with mitral regurgitation) which may affect PM position.

The objectives of this study were: 1) to investigate the effects of annular shape and annular motion, on chordal force distribution and mitral valve function; 2) to study the effect of papillary muscle position on chordal force distribution.

Eleven human mitral valves were studied in a physiological left heart simulator with a variable shaped annulus (flat vs. saddle). Cardiac output and trans-mitral pressure were analyzed to determine mitral regurgitation volume. In six experiments, force transducers were placed on six chordae tendineae to measure chordal force distribution. C-ring force transducers were individually sutured onto the following chords: anterior strut chord, anterior marginal chord, posterior intermediate chord, stem of the posterior marginal chord, basal posterior chord, and commissural chord. The experiments were carried out in the normal and pathological papillary muscle positions.

Furthermore, six additional mitral valves were tested using a flexible annulus model. These experiments were conducted in the same left heart simulator, and the same six

chordae tendineae were instrumented with C-rings. The experiments were carried out again in the normal and pathological papillary muscle positions.

Finally, seven human and four porcine mitral valves were sutured to a flat annulus ring and tested in the left heart simulator. These experiments were conducted in eight different PM positions, which were constructed from 5mm vectorial displacements from the normal PM position.

All the experiments were carried out under physiological conditions (cardiac output: 5 L/min, peak trans-mitral pressure: 120 mmHg, heart rate: 70 BPM).

When comparing the flat and saddle shaped configurations, there was no significant ($p=0.17$) difference in mitral regurgitation volume $11.2\pm24.7\%$. In the saddle shaped configuration, the tension on the anterior strut chord was reduced $18.5\pm16.1\%$ ($p<0.02$), the tension on the posterior intermediate chord increased $22.3\pm17.1\%$ ($p<0.03$), and the tension of the commissural chord increased $59.0\pm32.2\%$ ($p<0.01$). Annular shape also altered the tensions on the remaining chords.

In the experiments which used the flexible annulus model, mitral regurgitation volume due to papillary muscle displacement (16.8 ± 1.5ml/beat) was significantly larger than those previously observed using the static annulus models ($p<0.05$). Peak systolic tensions were similar for the intermediate and marginal chords when comparing the results for the static and flexible annuli. The basal chords showed a significantly ($p<0.1$) larger force in the experiments which used the flexible annulus when compared to the forces present using the static annuli.

In the experiments on papillary muscle position, the anterior strut chord showed significant ($p<0.1$) variations in peak systolic tension (PST) for those positions associated

with apical motion of the PMs. The posterior intermediate chord also showed significant variations in PST for positions associated with apical displacement of the PMs. In contrast, both the anterior marginal and posterior marginal chords showed relatively uniform PST for the eight different PM positions, with small but significant ($p<0.1$) variations in tension for positions associated with lateral and apical displacement. The posterior basal and commissural chords were the most sensitive to tension variations due to PM displacement. These chords showed relatively large and significant ($P<0.1$) variations in PST for five of the eight different PM positions.

The results of this thesis provided evidence for the following conclusions: 1) Annular shape alone does not significantly affect mitral regurgitation; 2) A saddle shaped annulus redistributes the forces on the chords by altering coaptation geometry, leading to an optimally balanced anatomic/physiologic configuration; 3) Annular motion makes the mitral valve more sensitive to alterations in papillary muscle position, leading to increased regurgitation under pathological conditions; 4) Under physiological conditions, annular motion and flexibility do not affect PST on the marginal and intermediate chords. The tension on the basal chords varies significantly with annular motion; 5) The chords which insert nearer to the annulus are more sensitive to PM displacement while those further from the annulus, marginal chords, are less sensitive to PM displacement. This functional characteristic of the mitral valve allows it to work within a dynamic environment while isolating leaflet motion.

CHAPTER I

INTRODUCTION

According to the World Health Organization 16.6 million people die each year world wide because of cardiovascular disease (CVD). Of these fatalities, 7.2 million deaths are from heart disease and 5.5 million are from stroke. In 2001, CVD contributed to nearly one third of global deaths [1]. In the United States, CVD is the leading cause of death, and estimated direct and indirect costs of CDV are 351.8 billion dollars [2].

Heart valve disease plays a major role in these statistics. In the year 2000 alone, 87,000 heart valve operations were performed in the United States. Aortic valve disorders followed by mitral valve disorders where the leading causes of death for patients with heart valve disease [2]. The mitral valve is the most complex of the valves in the human heart; therefore, significant research has been conducted to elucidate its function under physiological and pathological conditions.

Traditionally rheumatic fever was synonymous to mitral valve disease, but the reduction in cases of rheumatic fever in developed countries has displaced the focus of interest onto other mitral valve associated pathologies. Ischemic heart disease and cardiomyopathy are common and morbid pathologies that may affect the mitral valve apparatus and its function. Kaplan et. al. 2000 reported changes in mitral annulus geometry and dynamics in patients with dilated cardiomyopathy and ischemic heart disease[3]. These results support findings by Toumandis et. al. 1992 and Flachskampf et. al. 2000, which showed that significant differences existed in annular size and motion in patients with dilated and hypertrophic cardiomyopathy[4][5]. In all these studies, geometrical and dynamical

1

changes on the mitral valve annulus were associated to different degrees of mitral malfunction, characterized by the presence of clinically significant levels of mitral regurgitation.

In a complementary study, Madu et. al. 2001showed how dilated cardiomiopathy reduced papillary muscle contractility [6] and Tibayan et. al. 2003 showed how the endocardial radius of the left ventricle increased under the same pathology [7]. Gorman III et. al. 1997 also showed in an ovine model how the papillary muscles lost contractility and displaced under ischemic conditions [8]. Therefore, ischemic mitral regurgitation and functional mitral regurgitation, pathologies associated with ischemic heart disease and cardiomyopathy respectively, changes in annular geometry, annular dynamics, papillary muscle function and location have been identified.

Changes in papillary muscle function and position are communicated to the annulus and the leaflets through the chordae tendineae. The importance of the chordae tendineae in mitral valve and ventricular function has been known for years. Also, Carabello et. al. 1993 describes how the preservation of the major chords is an important factor in the success of mitral valve repair and replacement procedures [9]. Recently, Messas et. al. 2001 proposed chordal cutting as a correctional procedure for ischemic mitral regurgitation [10]. Therefore, chordal force distribution under physiological and pathological conditions is an important area of study, not only for the understanding of the native mitral valve, but also for the understanding of the underlying mechanics of some of its pathologies and possible correction procedures. Only Lomholt et. al. 2002 has identified the tension on a limited number of chords during the cardiac cycle [11].

Therefore, further knowledge of mitral valve chordae tendineae force distribution is required.

The research presented in this thesis studies the effects of annular shape and dynamics, and papillary muscle position on chordal force distribution and valve function. To independently analyze the variables of interest, *in vitro* experiments were utilized. Experiments were performed on both porcine and human mitral valves in a physiological left heart simulator. Two different atrial chamber models were used. The first allowed to change the shape of the annulus from a flat ring to a three dimensional saddle shape geometry, designed within physiological dimensions. This model was used to isolate the effects of annulus geometry on valve function and chordal force distribution. The second atrail chamber model used a flexible membrane to enable annular displacement, allowing the valve to assume its natural configuration according to its anatomical relations. C-ring force transducers were used to measure chordal tension on individual chords. Trans-mitral pressure, mitral flow, and chordal tension were monitored online. The experiments were conducted for eight different PM positions, which were constructed from 5mm vectorial displacements from the normal PM position. These experiments provided data on chordal force distribution and valve function while varying annular shape, annular motion, and papillary muscle position.

BACKGROUND

2.1 The Heart
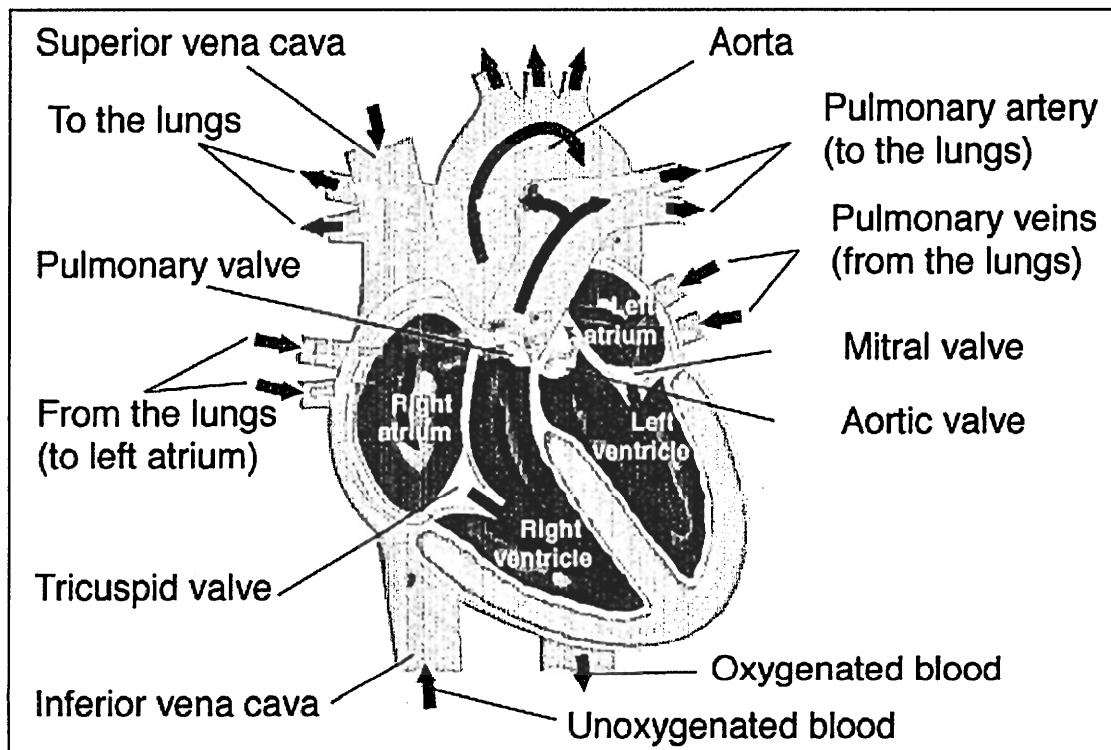
Figure 2.1 Diagram of the Heart, its components and flow of blood.
(http://members.rogers.com/smheart/html/heart_diagram.html)

The human heart is a hollow, cylindrical shaped muscular organ, which constitutes the driving force for the circulatory system. The heart occupies a small region between the third and sixth ribs of the thoracic cavity [12]. The heart to some extent may be considered two independent pumps. Each separate pump is comprised of two separate chambers, a

superior atrium and a lower ventricle. These chambers are separated by atrio-ventricular (A-V) valves, which control flow between the chambers. Semilunar valves in the ventricles control backflow from the arteries. Pump synchronicity is controlled by electrical potentials originating at the sinus node and traveling through the atrio-ventricular bundle [13]. Therefore, the heart is comprised of four valves and four chambers, which pump non-oxygenated blood through the lungs, and then pump this newly, oxygenated blood into the rest of the body (Figure 2.1).

2.1.1 The Right Heart

The right side of the heart is considered a low-pressure system, as its function only requires pressures up to 40mmHg gauge [12]. The function of the right side of the heart is to pump blood returning from the circulatory system into the lungs; therefore, because of the proximity of the lungs, relatively low driving pressures are required to fulfill this function.

As the right side of the heart works under significantly lower mechanical conditions, lesser pathological conditions have been observed in this system. Right heart dysfunction normally is due to congenital or pulmonary pathologies, which may be caused by idiopathic mechanisms or thromboembolic events. Also left heart failure may cause right heart failure in the long run [14].

2.1.2 The Left Heart

Functioning at pressures up to 150mmHg, the left side of the heart has the function of pumping the blood through the circulatory system. The left side of the heart is also

composed of an atrium and a ventricle (Figure 2.1). The left atrium has a volume of approximately 45ml and works at pressures up to 25mmHg. The left ventricle has an approximate volume of 100ml and works normally at a pressure of 120 mmHg; although, pressures may increase to 150mmHg under pathological conditions. Even if the internal volumes of the chambers on the left side of the heart are normally smaller than those in the right heart, the cardiac muscle on the left side is significantly thicker, as larger force is required to pump at higher pressures [12].

Left heart cardiac dysfunction can be due to ischemic heart disease, hypertension, cardiomyopathy, valvular pathology, congenital defects, bacterial and infectious processes, and other pathological factors. Valvular pathologies are predominant in the left side of the heart; this is explained by the increased mechanical loading on these components.

The heart as a whole is a complex and synchronized mechanism. Between its four chambers it holds around 350ml of blood, which is approximately 6.5% of the total blood volume of a typical individual [12]. Because of its limited volume, the heart must cyclically pump to ensure continual renewal of oxygenated blood in the tissues.

2.1.3 The Cardiac Cycle

The cardiac cycle describes the events occurring between the beginnings of two consecutive heartbeats. Each cardiac cycle begging is the sinus node by the spontaneous generation of action potentials [13]. This action potential travels through the atrio-ventricular bundle from the atria to the ventricles. Because of the arrangement of the

conducting system, there is a delay of approximately 1/10 of a second in the passage of the pulse from the atria to the ventricles. Therefore, the atria contract first, completing ventricular filling, and later the ventricles contracts, displacing their blood volume. The interaction between the atria, ventricles and valves is similar for both sides for the heart; therefore, the following detailed explanation of left heart function may be extrapolated to the right side of the heart considering the lower pressures present in this section.
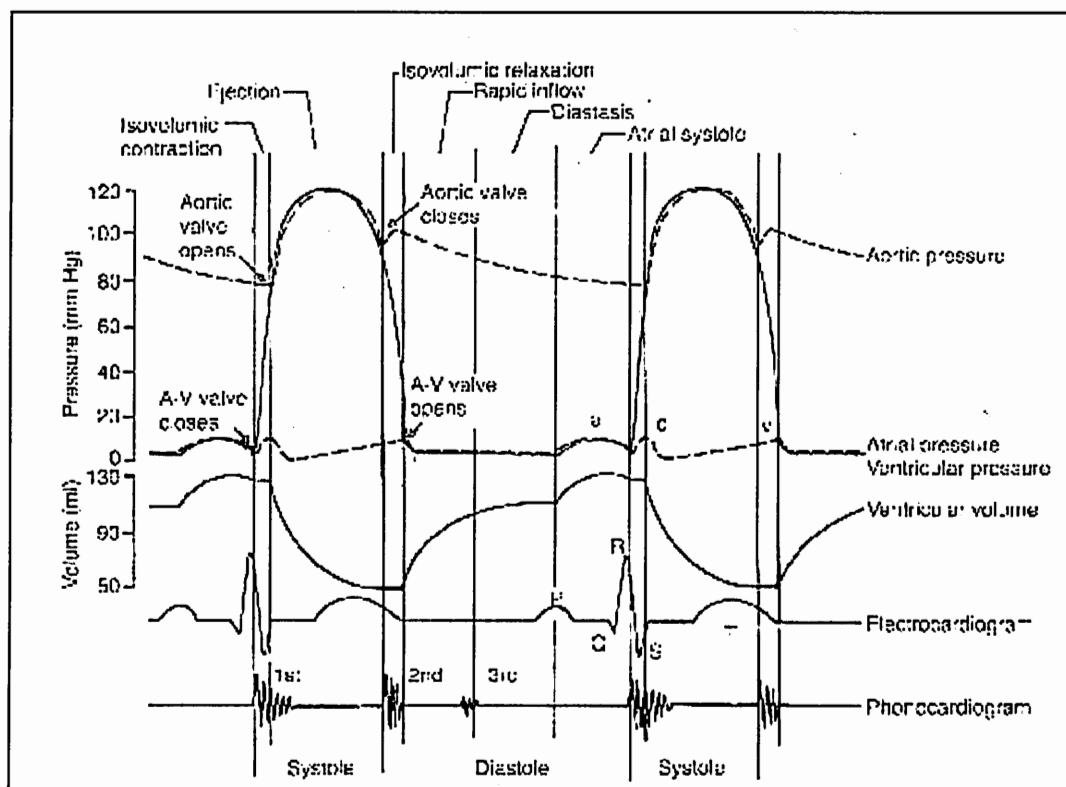
Figure 2.2. The events of the cardiac cycle for left ventricular function (Guyton 1997).

Figure 2.2 describes the sequence of events occurring in the left heat during the cardiac cycle. The cardiac cycle consists of two main sections, a period of relaxation called diastole and a period of contraction called systole. Diastole comprises approximately two

7

thirds of the cardiac cycle (560 ms), while systole comprises approximately the remaining third (300ms). Initially during diastole, the ventricle undergoes a process of isovolumic relaxation, which couples with the rapid inflow of blood from the atria. During this initial sequence, blood flows continuously from the veins into the atria, and then directly into the ventricle through the mitral valve. Approximately 75% of the blood is displaced in this period. The remaining 25% is displaced during atrial systole by contraction of this chamber. Atrial contraction completes ventricular filling and marks the end of diastole. The vortices in active ventricular filling do not cause partial valve closure in mid-diastole [15]. Initial systolic contraction abruptly increases ventricular pressure; therefore, increasing the pressure gradient across the valve, causing the A-V valve (mitral valve) to close. During the next 20 to 30 milliseconds ventricular pressure builds up before the semilunar valve (Aortic valve) opens [13]. Therefore, this period is considered to be an isovulomic contraction. When the left ventricle reaches a pressure of approximately 80mmHg the aortic valve opens, allowing for the ejection of blood into the aorta. Pressure continues to build up during ejection up to 120mmHg. During the initial first third of the ejection period, 70% of the ventricle is emptied, while only 30% is emptied during the last two thirds of ejection. During ventricular systole the mitral valve is closed, thus large amounts of blood accumulate in the atrium. As soon as systole is over, the blood in the atrium pushes the mitral valve open, immediately decreasing the pressure in the ventricle to diastolic values. All events in this cycle are sequentially coupled by the action potential described by the P,Q,R,S and T waves. Cardiac function is quantified in terms of cardiac output (CO). This variable represents

the volume of blood pumped by the heart into the circulatory system per unit time. Cardiac output is calculated through the following equation (equation 1):

$$CO = HR \times (EDV-ESV)$$

In this equation, EDV represents end diastolic volume in the left ventricle and ESV represents end systolic volume in the left ventricle. The difference between these two variables defines the stroke volume (SV). Stoke volume describes, the volume of blood that the heart ejects into the aorta during the cardiac cycle. The CO is calculated by multiplying the SV by the heart rate (HR). The CO is approximately 5 L/min for a typical person.

Underlying these functional characteristics, the heart hosts several electrical, chemical and biological events, which also characterize this infinitely complex life sustaining pumping system.

2.2 The Mitral Valve

Because of its importance within the body, its complexity, and its multiple components, extensive research on the heart has been performed for centuries [16]. Within valve function, special emphasis has been placed on the mitral valve since it is the most heavily loaded and complex of the four valves present in the heart. As shown in these sketches by Leonardo Da Vinci and Andreas Vesalius (Figure 2.3), the basic structure of the valve
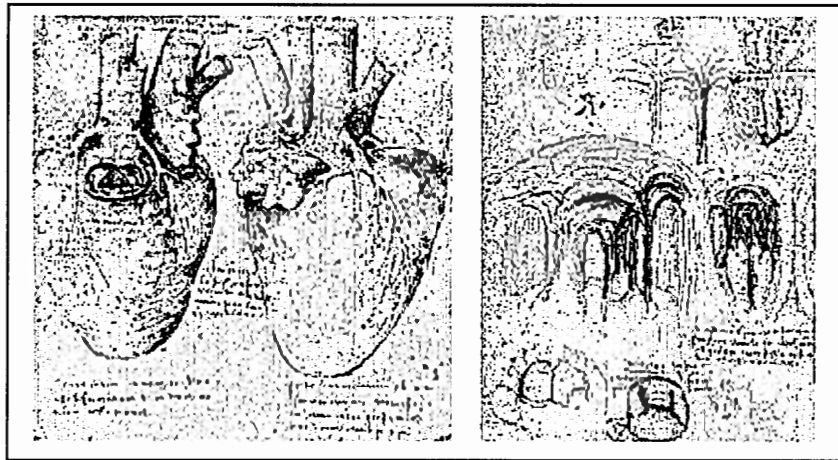
Figure 2.3 Sketches of the human heart by Leonardo Da Vinci and Andreas Vesalius (Jensen et. al. 2000)

was described centuries ago, but only recent and detailed studies have provided important

understanding of mitral valve functional anatomy, loading environment, and mechanics.
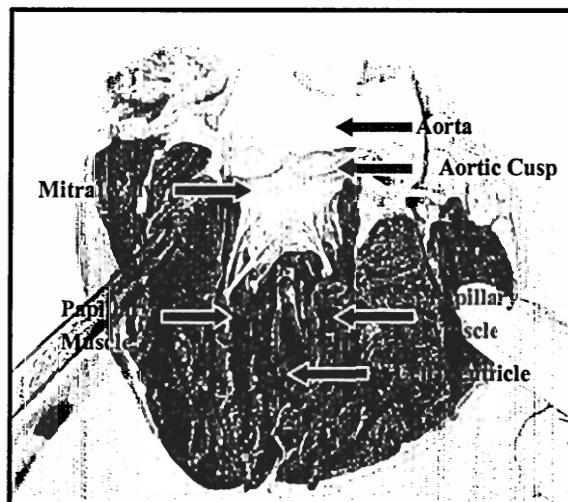
Figure 2.4. Photograph of the mitral valve and its components within the left ventricle.

The mitral valve is a complex unit comprising the annulus, the leaflets, the chordae tendineae, and the underlying left ventricular myocardium [17]. As shown in Figure 2.4, the mitral valve is attached to the left atrium and ventricle through its annulus, while the papillary muscles (PM) extend from the anterolateral and posteromedial sections of the ventricle. The PMs are named according to their location in the ventricle, anterolateral papillary muscle (APM) and posteromedial papillary muscle (PPM).The PMs are communicated to the leaflet by the chordae tendineae, which extend from the bellies of the PMs and insert relatively symmetrically to both leaflets and the commissures. The mitral valve is separated from the aortic valve by the intravalvular curtain. Under normal conditions these valves maintain a 135-degree angle between them. The section of the annulus adjacent to the aortic valve holds the anterior leaflet, which is the largest leaflet, present in the mitral valve. The mitral valve uses residual tissue on the tips of its leaflets as coaptation surfaces, which works as seals. To accomplish its purpose under complex conditions, the mitral valve is redundantly designed, having on average a leaflet surface area two times larger than the area of the mitral orifice [18].

2.2.1 Mitral Valve Leaflets

Although there is large anatomical variability in leaflet anatomy from valve to valve, there are several features which are consistently observed in all normal specimens. The leaflet section of the mitral valve consists of a continuous veil of tissue [17], which inserts into the annulus muscular ring around the entire circumference of mitral orifice.
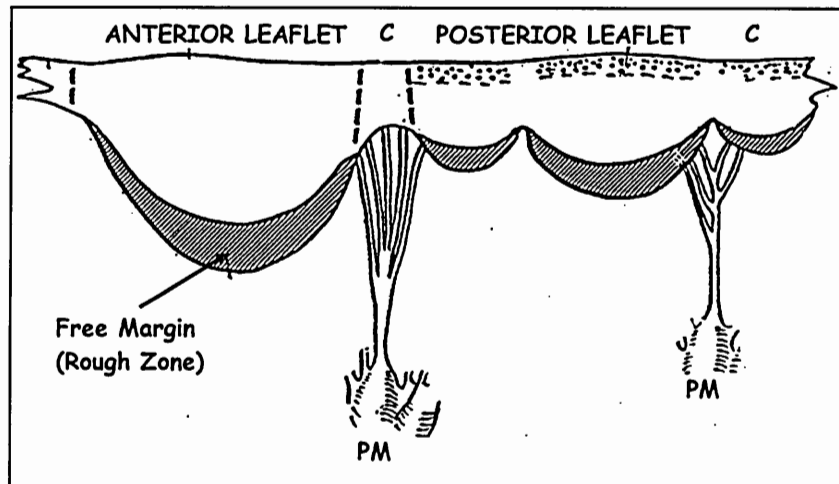
(a)
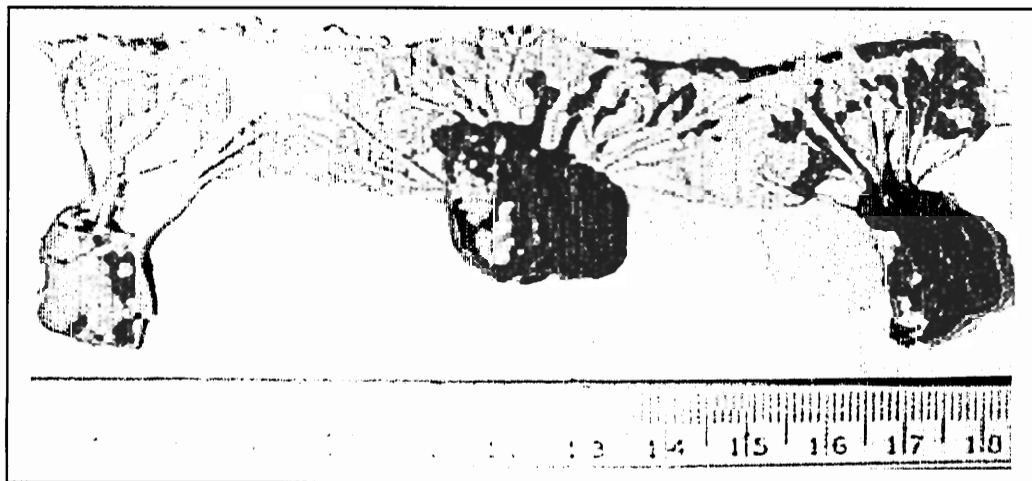
(b)

Figure 2.5 a) Diagrammatic representation of the mitral valve with fan-shaped commissural and cleft cleft chordae tendineae attached. (Raganathan et.al. 1970). (b) Photograph of a dissected porcine mitral valve.

As shown in Figure 2.5, two major leaflet sections may be identified regularly, and because of their location within the valve, they have been named the anterior and the posterior leaflets. These leaflets are separated by two commissural sections located in the

anterolateral and posteromedial sections of the ring. As observed, the commissural sections of the annulus are characterized by fan-like chordae tendineae insertions. The commissural sections of the valve are part of the posterior system; therefore, the mitral valve generally (92% of cases) [17] contains three scallops in its posterior section. The posterior leaflet as a whole contains all three scallops, although, the major central scallop is usually called the posterior leaflet, while the other two are described as commissural scallops and identified by location (postero-medial commissural scallop and anterolateral commissural scallop).

Three major zones can be identified in both leaflets: 1) a rough zone in its distal section, 2) a clear zone proximal to this, and 3) a basal zone. Both, the rough and basal zones receive chordae tendineae insertion, while the clear zone is membranous and relatively smooth [17].

The posterior leaflet, scallops included, attach to the larges section of the mitral orifice perimeter. The posterior leaflet is characterized by its dense insertion of chordae tendineae. Because of this dense insertion of chords, the ventricular surface of the posterior leaflet is extremely wrinkled and dominated by ridges. During coaptation, the central scallop of the posterior leaflet tends to be stretched out and in contact with the anterior leaflet, while the commissural scallops cover the border zone sections between the two leaflets.

The anterior leaflet has a significantly larger area that the posterior leaflet, and during coaptation covers most of the mitral orifice. As the anterior leaflet covers most of the mitral orifice, it is subject to a larger load due to pressure. The anterior leaflet is also subject to a significantly lesser insertion of chords. Two major strut chords insert into the

midsection of the leaflet while several marginal chords insert into its tips. Because of the larger orifice area covered by the leaflet, and the chordal insertion pattern, the anterior leaflet billows during coaptation. The curvature generated by billowing has been shown to be of mechanical importance, as it reduces the stress on anterior leaflet material [19]. Because of its size and function, the anterior leaflet is considered the most important scallop on the mitral valve.

The MV leaflets are also composed of three layers that may be observed under the microscope. An initial endothelial layer on the atrial side, an intermediate layer of fibrous material called spongiosa, and a ventricular endothelial layer. An important characteristic of this arrangement is the underlying collagen microstructure in the intermediate layer. Like all collagenous tissue, the MV anterior leaflet has been shown to be viscoelastic, and further, because of the directionality of the collagen fibers it has been shown to be anisotropic [20][21]. Events such as collagen fiber locking after valve coaptation and their mechanical significance have revealed the specificity of mitral leaflet material to its function.

In addition, mitral valve leaflets are not simple membranes. The presence of nerves, vessels, and smooth muscle cells capable of contraction, makes them complex biological systems. Recent research has shown that smooth muscle cell contraction may contribute to the tone of the aortic leaflets [22]. As these cells are also present in mitral valve, the function of these leaflets may not be passive.

2.2.2 The Mitral Annulus

Although the mitral annulus has been described anatomically as an incomplete and almost diaphanous structure, recent findings have enlightened it as a vital component of the mitral annulus, which promotes efficient valve closure and left ventricular filling during diastole [23]. The sphincteric action of the annulus aids ventricular filling by expanding during diastole, and facilitates leaflet coaptation by contracting during systole. Because of the dynamic nature of the annulus and its enlightened function, recently several studies both in humans and animals have been focused on describing annulus dynamics.

Annular area dynamics is an important parameter not only for the understanding of mitral valve function, but for the design of cardiac implants such as annuloplasty rings. Elaborate animal studies using invasive methods in animal and non-invasive methods in humans have revealed important but sometimes conflicting data on annular size. Initial measurements by Davids and Kinmonth [23] [24] using radiopaque markers around the canine annulus revealed a 30% change in annular area, with annular contraction beginning during atrial systole. Other studies on dogs, using radiopaque markers and echocardiography, sheep using 3-D sonomicrometry, and pigs using echocardiography revealed annulus area reductions ranging from 34% to 12%[23]. Although there was a significant disparity in the magnitudes of the measurement, and the exact timing of the onset of mitral annulus contraction, all of these studies supported the idea of a presystolic mitral annulus contraction. Therefore, animal studies to some extent support the

hypothesis that the mitral annulus begins contraction during atrial systole, and continues to contract through ventricular systole.

In humans, two-dimensional [25] and three-dimensional echocardiography [26] have been the method of choice to study annular dynamics, although in recent years, additional studies have been conducted using MRI [27]. There is a large disparity of measurements of annular size and reduction. As the used techniques are non-invasive, researchers rely on their ability to identify anatomical markers of the annulus, therefore, all of these studies may be hindered human by judgment and error. As with animal measurement, although there was a disparity of magnitude, human studies also agree on the concept of annular contraction at the onset of left atrial systole, continuing through ventricular systole. Systolic annular area in these studies varies from $4.5cm^2$ to $12cm^2$, and diastolic annular area range from $5.2cm^2$ to $12cm^2$ [23].

Another controversial characteristic of the mitral annulus is its shape. Initially, the annulus ring was thought to be a flat structure, but imaging during the cardiac cycle showed apical-basal flexing of the mitral annulus both in animals and in humans. Recent studies have further elucidated the characteristics of annulus shape by demonstrating that the three dimensional curvature of the mitral annulus persists during the whole cardiac cycle [3]. Based on recent studies, the mitral annulus is described as a three-dimensional saddle because it resembles a non-planar, three-dimensional ellipse. In addition to its position, the area, the eccentricity, and the non-planarity or curvature of the MA varies during the cardiac cycle describing a dynamic structure [8] [23] [28-30]. Mitral annular geometry and dynamics have been studied *in vivo* in animals [8] [29-31] and humans [4] [26]

[32]-[34] both in normal and pathologic subjects. Three-dimensional echocardiographic studies on the shape of the mitral annulus have proposed saddle heights from 0.78±0.11cm to 1.2±0.2cm in humans [3] [5]. Another factor related to annular shape, which has been recently studied is the saddle height to commissural ratio. The interest in this parameter is that a computational model of the anterior leaflet showed that a saddle height to commissural ratio of 20%, (approximately what is present in humans and other animals) will optimize mechanical performance by reducing the stress on the anterior leaflet [35].

The mitral annulus does not only contract and bend, but it also moves during the cardiac cycle. The mitral annulus has been observed to displace across the apical-basal axis of the left ventricle. During systole, the mitral annulus moves basaly 10±3mm [5] from its most apical position during diastole.

Considering all the studies shown above, the mitral annulus is not a simple rigid ring which holds the leaflets, as proposed years ago[17], but a important dynamic structure which aids the mitral valve in its function.

2.2.3 The papillary muscles

Two sets of papillary muscles extend from the left ventricle wall: the anterolateral and the posteromedial. From the "bellies" of each papillary muscle, several chordae tendineae extend, which may insert into the valves leaflets or near the annulus, as well as into the left ventricular wall. The tips of the papillary muscle usually point to their respective

commissures [36], sending their chords to relatively symmetrical insertions on the valve. Papillary muscle "bellies" and chordal insertion pattern varies significantly between humans and also between species. According to their complexity, human PMs have been divided into four group types, type I being the simplest and type IV being the most complex. Normal porcine PMs are anatomically simple; therefore, they may be compared to a type I human PM (Figure 2.6). From each "belly", relatively individual excursions of muscle hold individual chords. Even though the PM are geometrically complex, average lengths and dimensions have been recorded in literature.

(a)   (b)   (c)
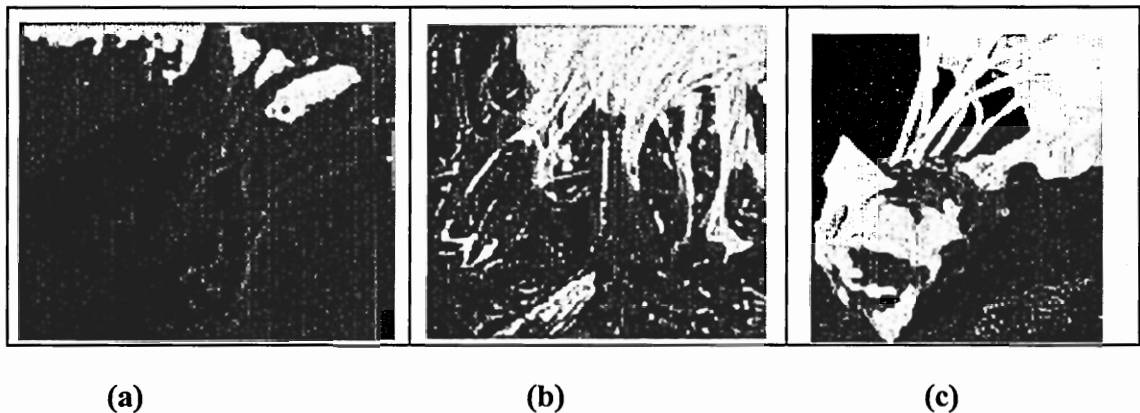
Figure 2.6. Photographs of papillary muscles: a) Simple human papillary muscle b) Complex human papillary muscle c) Porcine papillary muscle.

In healthy sheep, sonomichrometry transducer studies have shown average APM lengths of 23.2mm during diastole and 20.1mm during diastole. Simultaneously, the lengths of the PPM were 25.2mm during diastole and 23.0mm during systole [8]. Therefore, papillary muscle contractions on the order of 2-3mm are present in sheep models. Using transesophagic echocardiography (TEE) studies have been able to assess both length and cross sectional area of the normal human PMs *in vivo* [6]. The average cross-sectional

areas were $1.32\pm0.29cm^2$ for the APM and $0.99\pm0.18cm^2$ PPM at end diastole. At end systole, these areas changed to $1.71\pm0.31cm^2$ for the APM and $1.18\pm0.20cm^2$ for the PPM. In the same study, end diastolic APM length was $3.55\pm0.33cm$ and end diastolic PPM length was $2.91\pm0.20cm$. End systolic APM length was $2.81\pm0.35cm$ and end systolic PPM length was $2.42\pm0.23cm$. As these results show, the PM contract during systole approximately 4mm in humans.

Although these studies show accurate measurements of PM geometry, the actual dynamics of PM motion are still unknown. Limitations in time resolution for the methods employed have not allowed accurate calculations of PM contractility velocity in humans.

2.2.4 Chordae Tendineae

The main function of the chordae tendineae is to prevent leaflet prolapse during ventricular systole. These "tension wires" (as well as holding the leaflets in place during systole) are of great significance in the geometrical conformation of the mitral valve and play an important role in left ventricular function [9]. The chordae tendineae extend from both PMs and insert into different sections of the leaflets. Several anatomical studies have been conducted which characterize the chords in different groups. Normally, chords were characterized by their insertion point in the leaflets. Raganathan et al. 1970 named the chords accordingly: rough, cleft and basal chords. Recently simpler nomenclature has been used to characterize chords [37]:

1. *Primary or marginal*: These chords extend from the PMs, and insert into the free margin of the leaflets.

2. *Secondary or basal*: These chords originate in the PMs and insert into the body of the ventricular surface of the leaflets.

3. *Third order chords*: Which originate in the ventricle wall and insert into the ventricular surface of the posterior leaflets.

Most basal chords insert near the annulus, with the exception of a group of four special chords, which insert in the body of the leaflets between the marginal and basal sections. These chords are called by different names in literature: "stay chords"[37], strut chords, and in the case on the posterior leaflet they may be called posterior intermediate chords. The classification is not only based on anatomical location, but within these groups differences in composition, size, mechanical characteristics and function have been identified.

Marginal chords are significantly thinner than basal chords. Sedransk et al. 2002 observed that on average the marginal chords were 68% thinner than the basal chords, and that the chords on the posterior leaflet were 35% thinner that their counterparts on the anterior leaflet of porcine mitral valves[38]. Using a calibrated optical microscope on porcine chordae tendineae, results from Liao et al 2003 verify the fact that the marginal chords are thinner, assuming circular cross sectional areas and uniform thickness through the chord[39]. The average cross-sectional areas in this study were: marginal chords $0.38 \pm 0.18 mm2$, basal chords $0.71 \pm 0.25 mm^2$, and strut chords $2.05 \pm 0.40 mm^2$. Researchers have described the anatomies of porcine and human mitral valves as very similar. Kunzelman et. al. 1994 showed very similar lengths in porcine and human mitral

valve chordae tendineae [40], but there is limited data on the cross-sectional area of human chords; therefore, most studies relay on the porcine data described earlier.

Although limited mechanical characterization of the chordae tendineae exists in current literature, recent studies have elucidated important differences between chords which may be associated to their function. Uniaxial tensile tests showed how porcine marginal chords failed at significantly lower tension when compared to basal chords, although when considering the relations in cross-sectional area, failure stress followed a different trend for the different leaflets as observed in Table 1[38].

Table 2.1. Failure tension and failure stress for porcine marginal and basal chordae tendineae.

Location		Failure Tension (kg)	Failure Stress (N/mm2)
Anterior	Marginal	0.730±0.098	12.93±1.43
	Basal	2.270±0.264	9.63±0.95
Posterior	Marginal	0.420±0.035	7.98±0.82
	Basal	1.293±0.144	10.69±1.26

Further research by the same group revealed interesting relations between geometry and mechanical characteristics of the chords, which was related to their microstructural composition and arrangement [39].

Table 2.2 Extendibility, Tensile modulus and average chordal size for porcine chordae tendineae.

Chordal Type	Marginal	Basal	Strut	Significance
Extendibility(% strain)	4.3±1.6	8.5±3.0	17.5±3.3	p<0.001
Tensile modulus (MPa)	84.4±21.2	86.1±20.9	64.2±13.5	p=0.002
Average chordal size (mm2)	0.38±0.18	0.71±0.25	2.05±0.40	p<0.001

As shown in Table 2, extendibility increased with diameter, while the modulus of elasticity decreased with increasing diameter. All results showed statistically significant difference between the different types of chords. In this same study, transmission electron microscopy and polarized light microscopy were used to observe the microstructure of the chords. These observations showed how thicker chordae had a smaller crimp period of the collagen fibers, which allowed increased strain on thicker chords before lockup. Although the cross–sectional area occupied by the fibers was constant (49.2% on average), the thicker chords had a larger average fibril diameter but less fibril density. The results presented above show how the chordae tendineae have a very complex material structure, which varies from chord to chord as adaptation to their specific mechanical function. Currently no appropriate data on physiological loading rates or stress- strain curves exists for the chordae tendineae of the mitral valve.

2.3 Mitral Valve Mechanics

The mechanics of the mitral valve as a whole are complex, and limited studies on this subject have been conducted. The annulus, PMs, leaflets, and left ventricular wall are

22

synchronized to maintain a balance within a dynamical environment [41][42]. The overall force on the mitral valve leaflets is dictated by the pressure gradient across the valve. But within the constant motion of all its components, the actual force distribution and specific loading on the annulus, the chordae tendineae and PMs is a complex mechanical problem which requires extensive research.

2.3.1 Leaflet Mechanics

The loading on the leaflets depends on trans-mitral pressure, annular geometry/dynamics, coaptation geometry, chordae tendineae tension and distribution, and contact forces between the leaflets. Of these factors, only trans-mitral pressure and coaptation geometry have been studied in detail. Coaptation geometry and its effect on valve mechanics has been described by several authors in theoretical [43], in vitro [41][44], and in vivo models [45]. Actual leaflets mechanics has only been studied to a limited extent by a small number of researchers [21][22][35].

Although the anisotropic characteristics of valve leaflet materials was established early in mitral and aortic valve research, recent knowledge has elucidated the importance of material characteristics on mitral valve function. Kunzelman et. al. 1993 created a finite element model of the mitral valve that incorporated essential anatomic components, geometries and material characteristics [46]. This model showed how material characteristics and phenomenon like annulus and papillary muscle contraction contribute to an even distribution of stress throughout the valve. The mitral annulus saddle shape induced secondary curvature, was also identified as a stress relieving characteristics using a simplified computational model of the anterior leaflet [35]. This model of the saddle

23

shape of the mitral annulus proposes that a saddle height to commissural diameter ratio of approximately 20% generates the minimum stress configuration for the anterior leaflet, under systolic loading.

Sacks et. al. 2002 and He et. al. 2003 describe not only the anisotropic and viscoelastic characteristics of the anterior leaflet, but also how the underlying collagen matrix influences valve mechanics during coaptation by controlling directional strain through collagen fiber locking. Although recent studies of leaflet mechanics have provided interesting and important information, further studies are required, as many of the computational models and in vitro experiments need additional validation. Also, as most research has focused on the anterior leaflet; therefore, studies on the posterior leaflet are limited.

2.3.2 Chordae Tendineae Mechanics

Leaflet coaptation geometry is highly dependent on chordal insertion characteristics and chordal tension distribution. Nazari et. al. 2000 describes theoretically how the stress distribution on the leaflets of the valve is directly related to chordae tendineae distribution. This study describes how during coaptation the load on the leaflets is transferred sequentially to increasingly larger chords, leading to an optimal mechanical configuration during peak systole [43]. He et. al. 2000 proved how a characteristic triangular structure between different chords is fundamental to valve function, and that the disruption of these triangles may lead to mitral regurgitation [47]. Nielsen et. al. 1999 using an in vitro model showed how tension on the chords that insert into the leaflet are directly responsible for coaptation geometry and valve function. These studies described

the importance of chordal force distribution on valve mechanics; but only one study has been able to measure the force distribution on chordae tendineae in an *in vivo* model [11]. Lomholt et. al. 2002 showed that the dynamic tension on the secondary chords was three times as large as that present in the primary chords. Actual measurement showed peak systolic tension of 0.7N for the secondary chordae tendineae, while the average load on the primary chords was only 0.2N. Data on basal and commissural tendineae has not been recorded. In addition, limited mechanical characterization of chordae tendineae material has been conducted. In general, the underlying collagen matrix is responsible for the viscoelastic and anisotropic characteristics of chordae tendineae [39]. In addition, structural differences also lead to different mechanical behavior for different types of chords (Table 2.1 and Table 2.2). Further research which describes material behavior for chordae tendineae under physiological loading is required, as current studies have only considered failure stress and simplified material characteristics [38] [39].

2.3.3 Papillary Muscle Mechanics

The overall load on the chordae tendineae is sustained by the PMs; therefore, PM contraction in conjunction to leaflets mechanics determine the force distribution on the chordea tendineae. An *in vitro* study of porcine mitral valves showed loads on the PMs in the order of 4.4N for the PPM and 4.1N for the APM [16], although this model did not simulate PM contraction. Therefore, these results represent only the force present in the PMs due to valve closure, but they do not consider annular motion or mechanics, ventricular motion or PM contraction.

Although a recent advanced computational model has incorporated PM mechanics, chordal tension, leaflet mechanics and fluid mechanics [48]. Further research on PM loading, leaflet mechanics, chordal force distribution, and chordal/leaflet interaction is required, not only to validate these type of studies, but to provide further understanding of the native physiological and pathological mitral valve. Understanding of these mechanics is necessary for the design of new cardiac implants and surgical repair procedures.

2.4 Pathologies of the mitral valve

Due to the characteristics of mitral valve function, mitral valve pathologies are described as complex and often morbid. There are several pathologies which directly affect the mitral valve by infectious processes or trauma, but there are other cardiac pathologies that even though they are not directly located on the valve often affect its function. As the mitral valve's function is to control the flow between the two-left heart chambers, pathologies may be grouped in two different functional groups. The first group is stenosis, which describes the total or partial obstruction of the mitral orifice affecting ventricular filling. The second group is associated with malfunction during valve closure. When the mitral valve does not close adequately, the higher pressure in the ventricle during systole generated backflow jets into the atrium, this condition is called mitral regurgitation (MR). Mitral regurgitation may result from congenital deformation, disease,

or when in absence of structural valvular abnormalities, this condition is referred to as functional mitral regurgitation (FMR).

Both mitral stenosis (MS) or MR are products of several different causes, and may exist simultaneously under specific conditions. Under MS or MR, the heart has to work harder as the efficiency of cardiac function is reduced. Efficiency is reduced by the reduction of stroke volume. In the case of MS, stroke volume is reduced because of the inappropriate filling of the ventricle. When associating cardiac efficiency to mitral regurgitation, there are several terms that must be considered. Normally during systole, there is a small amount of backflow through the valve as its leaflets are closing; this is called mitral closing volume. After valve closure, backflow into the atrium is termed leakage volume, which is associated to mitral valve dysfunction as the valve normally seals perfectly. The sum of the closing volume and the leakage volume is called regurgitation volume and represents all the negative flow through the mitral valve during a cardiac cycle. The ratio of regurgitation volume to stroke volume is defined as regurgitation fraction, which is an important parameter in mitral valve incompetence diagnosis. Clinically significant regurgitation fractions are above 20% [41].

When the heart cannot compensate for the improper function of the mitral valve, cardiac output is reduced and therefore the body is subject to an inadequate supply of oxygen to the tissues. Patients with mitral valve disease will appear fatigued, present palpitation or suffer from chest pains [16], but under severe pathologies were cardiac function as a whole is compromised, mitral valve disease may prove to be deadly.

For several decades mitral valve disease was equated to rheumatic fever, as it was the most common pathology. Rheumatic fever causes the formation of small thrombi on the

valves surface, which leads to leaflet thickening or chordal shortening [17]. The combination of lesions in both the leaflets and chords may produce MS, MR or a combination of both. Other diseases that may affect the mitral valve are bacterial endocarditis [49] and Whipples disease [17]. Recently, because of the reduction in cases of rheumatic fever, other pathologies have become the center of mitral valve incompetence research. Ischemia, trauma, and cardiomyopathy have all been related to mitral valve incompetence.

2.4.1 Mitral Valve Incompetence and the Mitral Annulus

The mitral annulus as an important component of the mitral apparatus, has been related to several pathological conditions in which its size, dynamics, and shape may vary.

Dilation is an important and common condition in the mitral annulus, which has been related to several pathologies. Dilated cardiomyopathy, ventricular remodeling, and dilation after myocardial infarction have been associated with increases in annular area and subsequent regurgitation [3][4][5][8]. Flachakampf et. al. 2000 used three-dimensional Transesophagic echocardiography to reconstruct the mitral annulus of normal and pathological subjects. This study reported annular areas from 11.8 ± 2.5 cm^2 in normal patients to 15.2 ± 4.2 cm^2 in patients with dilated cardiomyopathy [5]. In an ovine model of normal and Ischemic hearts, increases in annular area were observed by Dagnum et. al 2000, after coronary occlusion. Researchers measured the commissural to commissural and septal-lateral diameters of the mitral valves of these sheep. The results showed significant increases in both diameters, during diastole and systole. During systole, the mitral annulus commissure-to-commissure diameter was 33.7 ± 1.4mm before ischemia,

28

and 34.6±1.7mm during ischemia. The septal- lateral diameter also increased from 24.3±1.2mm before ischemia to 27.4±1.8 after ischemia [45].

Clinically, annular dilation is generally accompanied by other alterations of the mitral valve apparatus and the left ventricle (Ventricular dilation, reduced ventricular contraction, PM displacement, etc.). Hence, *in vivo* it is not possible to quantify the individual contribution of annular dilation and these other factor to mitral regurgitation. To solve this problem He et. al. 1999 designed an in vitro study which isolated the effect of annular dilation on mitral valve function. This study showed conclusively that dilating the annulus by a factor 1.75 induced mitral regurgitation without PM displacement, while PM displacement induced MR at significantly lesser levels of annular dilation [18].

Other more subtle changes in annular geometry have been observed in patients with mitral regurgitation. Changes in annular geometry (increased 2D-area, increased 2D-perimeter, decreased saddle curvature) were observed in patients with functional mitral regurgitation [3]. The patients in this study of FMR had as primary pathologies dilated cardiomyopathy and ischemic congestive heart failure. In this study there was a significant decrease in saddle height between normal and FMR patients. Flachskampf et. al. 2000 presented in a clinical study of dilated and hypertrophic cardiomyopathy. This study reported changes associated with annular shape, specifically annular saddle height. Saddle height decreased from 1.2±0.2mm in normal patients to 0.76 ± 0.1mm in patients with hypertrophic cardiomyopathy [5]. Therefore, changes in saddle height or curvature have been described as a possible cause of MR. Researchers base this hypothesis on the

decreased septal-lateral diameter associated with saddle curvature, which may aid in valve closure.

Flachskampf et. al. 2000 and Toumanidis et. al 1992, in independent clinical studies, showed decreases mitral annulus apico–basal motion in patients with mitral regurgitation [4][5]. In Flackskampf's study, decreases of approximately 7mm in annular displacement are associated with dilated cardiomyopathy. The study by Toumanidis showed variations in annular motion associated with several cardiac pathologies that resulted in subsequent MR. In this study, annular motion was combined with annular area to calculate the volume traveled by the mitral valve during the cardiac cycle. Changes in this volume were directly associated to mitral regurgitation.

There are several repair procedures associated with restoring the size and function of the mitral annulus. The most common procedure is the insertion of an annuloplasty ring. The ring is sutured around the mitral annulus restoring to some extent its size. There are several types of rings that are described by geometry and flexibility. Rings are described as rigid or flexible according to their flexibility, and complete or partial according to geometry. The first annuloplasty rings were rigid and complete, these rings are still used today and their latest versions include apical-basal curvature to restore the saddle shape of the mitral valve. Newer flexible rings have been designed as a result of studies which show the important of annular dynamics in mitral valve function. These rings try to maintain annular bending and contraction during the cardiac cycle. But, results on their effectiveness in maintaining annular dynamics are contradictory in current literature

[50][51]. Different groups have studied several brands of rings finding disparities in their dynamic characteristics. Most rings severely reduce mitral annular dynamics, as they must have a somewhat rigid nature to hold the annulus from dilating again. Partial rings were developed in order to prevent obstruction of the aortic outflow track since complete rings may alter the mechanical characteristics of the aortic root. Also, improper ring placement and selection has been shown to induce systolic anterior motion in valves with oversized anterior leaflets.

Alternative methods for mitral annulus repair have been developed in recent years. When dealing with annular dilation and leaflet malcoaptation, the Alfrieri Stitch is another commonly used new procedure. In this procedure the tips of the anterior and posterior leaflets are sutured together in order to correct coaptation. A recent study by Nielsen et. al. 2001 measured the tension on the suture after the Alfieri procedure in order to assess its feasibility [52]. This procedure may be accompanied by annulopasty ring insertion. The need of the annuloplasty in the Alfrieri Stitch procedure is still under debate.

.

2.4.2 Papillary Muscle Displacement in Mitral Regurgitation

Though mitral leaflet malcoaptation is the end point through which mitral regurgitation (MR) occurs [44], several topological changes caused within the left ventricle have been associated with this malfunction of the mitral valve [53]. Ventricular dilation [54-56] and sphericity [57-59], papillary muscle contractile malfunction [31], annular dilation [18] [60], and motion abnormalities of the left ventricle have been associated with leaflet mal-coaptation and therefore MR. Ventricular dilation, ventricular sphericity, or PM malfunction may cause PM displacement. Although left ventricular dysfunction in most

31

cases is accompanied by several alterations of the mitral apparatus, PM displacement or discoordination have been identified as major and direct contributors to MR. Dilated cardiomyopathy and ischemic heart disease are the pathologies most commonly associated with PM displacement.

Gorman et. al. 1997 used an *in vivo* ovine model of ischemic mitral regurgitation to observe geometrical alterations of the different components of the mitral valve after infarction [31]. This study showed that significant mitral regurgitation occurred even though annular area increased only 9.2±6.3%. After infarction the posterior papillary muscle moved 1.4±0.6mm closer to the annulus, while the anterior papillary muscle moved 0.9±0.7mm from the annulus. In addition, losses of contractility on the order of 2mm were also observed in the PMs. Papillary muscle displacement induced tenting and bulging of the mitral leaflets and subsequent regurgitation.

Bulged/tented leaflet geometries have been observed in other studies of MR where PM displacements on the order of 1 to 2.5mm induced significant MR[8]. These results describe the dynamic and fragile balance between the components of the mitral valve. The findings from the aforementioned studies of ischemic mitral regurgitation, were confirmed by Nielsen et. al. 1999 and He et. al. 2003 using two different *in vitro* models. Both of these models showed how papillary muscle misalignment caused significant regurgitation in native porcine mitral valves [44][53].

Tibayan et. al. 2003 measured ventricular curvature and principal strains in an ovine model of dilated cardiomyopathy using an array of radiopaque markers, under biplane video fluoroscopy. The results of this study showed increases of approximately 5mm in

endocardiac ventricular curvature resulting in ventricular dilation and sphericity [7]. As the PMs are attached to the ventricular wall, their bases are subject to these displacements. Dilated cardiomiopathy has also been associated with losses of PM contractility on the order of 2-3mm from clinical studies in humans [6]. The loss of contractility implies additional dislocation of the papillary muscles. In addition, dilated and hypertrophic cardiomyopathies have been linked to mitral regurgitation [2][4][5][32]. Therefore, mitral regurgitation resulting form cardiomyopathy has been associated to PM displacement induced by ventricular alterations. This regurgitation may increase if annular dilation is also present under the aforementioned pathology.

Surgeons and clinicians have proposed several procedures to correct MR due to PM displacement. One solution is to reshape the ventricle in ischemic mitral regurgitation, but this requires extensive surgical manipulation [61]. Another proposed procedure is based on cutting a limited number of chords, which have severely altered tension configurations, in order to restore to some extent valve function [10]. Ventricular restraints may also be used after ischemic events to reduce remodeling and dilation, which in turn limits PM displacement [62]. In general, most procedures, which try to restore PM position or its effect on chordal force are not well established and require further research before massive implementation.

CHAPTER III

HYPOTHESIS AND SPECIFIC AIMS

Valve replacement is still used for some severe mitral valve pathologies. However, recently mitral valve repair has flourished because of advances in surgical techniques. Annuloplasty ring insertion, chordal cutting and translocation, ventricular remodeling, and ventricular restraints are procedures that have recently been developed for mitral valve repair. Most of these procedures are still under development and require further knowledge on mitral valve function under normal and pathological conditions. In the last 5 years several studies have improved basic understanding of mitral valve function. However, further research on the detailed function and mechanics of the individual components of the valve is necessary to improve the efficiency of these techniques; and therefore, the longevity and quality of life of mitral valve patients.

3.1 Hypothesis

3.1.1 Hypothesis 1

Physiological variations in mitral valve annular geometry and dynamics will modify chordal force distribution, but will not significantly affect mitral valve function.

3.1.2 Hypothesis 2

Papillary muscle relocation affects tension on the individual chords depending on their

insertion point on the valve (marginal, intermediate, or basal), hence, altering chordal force distribution.

3.2 Specific Aims

3.2.1 Specific Aim 1 – Hypothesis 1

To investigate the effect of mitral valve annulus shape on valve function and chordal force distribution. To achieve this aim, a variable annulus shape atrial chamber was constructed. This model was able to change the shape of the annulus from a flat ring to a three dimensional saddle while maintaining a constant three dimensional perimeter. It was important to maintain a constant perimeter so that the valve was not dilated when shifting shape. The geometrical specifications of the saddled annulus were designed within physiological ranges present during peak systole. The atrial chamber was coupled to a left heart simulator capable of physiological flow and pressure waveforms. Mitral regurgitation was induced by symmetrical displacement of the papillary muscles. Mitral valve function was assessed by analysis of the flow waveform, quantifying mitral regurgitation as the negative flow through the valve. Simultaneously, six chordae tendineae were instrumented with miniature force transducers. Chordae tendineae tensions were monitored using these transducers during the entire cardiac cycle for both annulus configurations. Regurgitation volume and chordal force distribution was obtained for the two annulus configurations, enabling a direct comparison of these variables for the two different annulus conditions.

3.2.2 Specific Aim 2 – Hypothesis 1

To investigate the effect of annular motion and flexibility on mitral valve chordal force distribution and valve function. Initial experiments showed that suturing a valve onto a flexible membrane and allowing it to deform while tethering the papillary muscles, generates a saddled annulus configuration because of chordae tendineae length. Therefore, to accomplish this aim, an atrial chamber with a flexible membrane supporting the annulus was constructed. This model allowed the annulus to deform and simulated annulus apical-basal motion within physiological ranges. Trans-mitral pressure, mitral flow, and chordae tendineae tension on six chords were monitored online during these experiments. These experiments provided information on mitral flow and chordal force distribution with a dynamic annulus. The effects of annular dynamics were analyzed by comparing these results to those obtained with static annuli as in specific aim 1.

3.2.3 Specific Aim 3 – Hypothesis 2

To understand how papillary muscle displacement affects tension on the different types of chordae tendineae. To attain this aim, both human and porcine mitral valves were evaluated in a physiological left heart simulator. Six chordae tendineae were instrumented with C-ring force transducers, which allowed online monitoring of chordal tension. C-rings were individually sutured onto the following chords: anterior strut chord, anterior marginal chord, posterior intermediate chord, stem of the posterior marginal chord, basal posterior chord, and commissural chord. The valves were evaluated under physiological flow and pressure conditions. The experiments were conducted for eight different PM positions, which were constructed from 5mm vectorial (apical, lateral,

36

posterior) displacements from the normal papillary muscle position. The simulated papillary muscle positions represent displacements of the papillary muscles which have been observed clinically with ischemic heart disease, dilated or hypertophic cardiomyopathy. Data from these experiments show how the marginal, intermediate, and basal chords react to apical, lateral, posterior or combinatorial displacements of the papillary muscles.

CHAPTER IV

MATERIALS AND METHODS

4.1 Mitral Valves
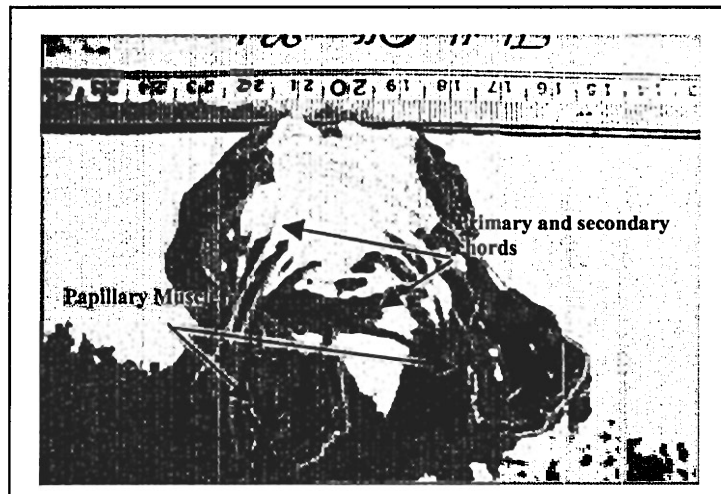
Figure 4.1. Intact human mitral valve with primary and secondary chordae tendineae and preserved papillary muscle sections.

Fresh porcine MVs from a local abattoir, fresh human MVs from Emory University and MVs from frozen human hearts provided by Corazon Technologies Inc. (CA, USA) were used in this study. Porcine mitral valve sizes were assessed using an annuloplasty ring sizer (Edwards Life sciences, CA, USA). The hearts from Emory University were obtained from heart transplant recipients with Institutional Review Board approval following the guidelines for the protection of study volunteers in research. Diseased mitral valves were excluded from this study. Valves with normal anatomical features and similar orifice areas ($6.8\pm0.4cm^2$) were used. Experiments involving measurements of

chordae tendineae tension only used valves with simple (Type I and Type II) PM insertion patterns (Figure 2.6). The reasons for the selection according to PM structure were that complex PMs could not be appropriately coupled with the ventricle model, and simple human papillary muscles are similar to porcine PMs. Valves were extracted from the hearts, preserving the complete mitral apparatus. (Figure 4.1)

During extraction, all chords that inserted into the leaflets or the annulus from the PMs were preserved. Chords which inserted from the PMs into the ventricle wall were severed. The extracted valves were preserved in saline solution (0.9%) to keep them moist during valve preparation and instrumentation. Valves were maintained in a refrigerator over night following preparation since extraction, instrumentation, and experimentation could not be completed in the same day due to time constraints. At least 15mm thickness was conserved in the PMs. This muscle volume allowed the valves to be couple to the left ventricle simulator. Six human valves were used for specific aim1, six human valves were used in specific aim 2, and four porcine and seven human valves were used in specific aim 3.

4.2 In *Vitro* Flow Loop

The *in vitro* experiments were carried out in the modified Georgia Tech left heart simulator. The simulator uses a pressure driven compressible bladder type pump, which is controlled and synchronized by a pulse generating computer system. Compressed air is fed to the system main line at 40 psi by a portable compressor (Thomas Ultra Air Pac, Model T-2820, Thomas compressors & vacuum Pumps, WI, USA). The air in the system

is controlled by solenoid valves which are synchronized using a generic driver and a pulse timer unit (TeleVideo Model 910, Televideo Inc, CA, USA). The function of this controlled air supply is to cyclically compress a silicon bladder, which provides the driving force for the loop simulating ventricular pressures. The solenoid valves in the system were synchronized to maintain a total cycle time of 860ms, with systolic (compression) duration of approximately 300ms, and diastolic (expansion) duration of 560ms.

Trans-mitral pressure was measured using a differential pressure transducer (model DP15-24 Tl, Valydine Inc., Northridge, CA) coupled to an amplifier/signal conditioner (model CD23, Validyne Inc., Northridge, CA). The trans-mitral flow rate was measured upstream from the valve using a cannular type electromagnetic flow probe (model EP680
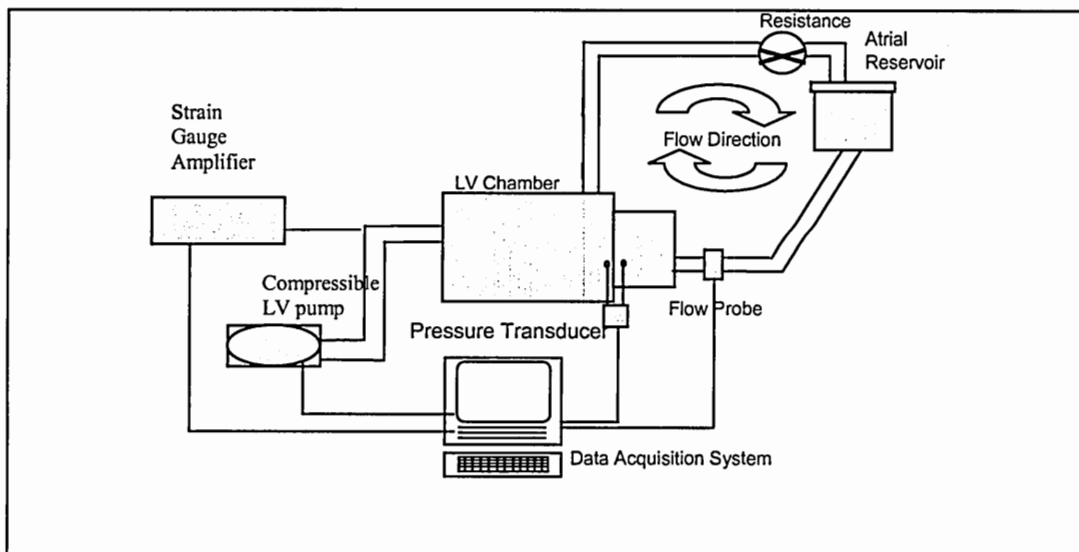
Figure 4.2. Schematic of the Georgia Tech physiological left heart simulator.

Carolina Medical Instruments Inc. King, NC) connected to an analog flow meter (model FM501, Carolina Medical Instruments Inc. King, NC).

As observed in the diagram (Figure 4.2), the left heart simulator is composed of a reservoir, an atrial chamber, a ventricular chamber and bladder, a resistance and connective tubing. The system is filled with 0.9% saline as blood analogue. Initially the atrium is filled by fluid from the reservoir by gravity; the liquid column in the reservoir is set to simulate atrial pressures. Fluid from the atrium flows into the ventricle through the native mitral valve. The bladder compression system then builds up pressure in the ventricular chamber forcing the fluid out through the aortic valve. Sections of tubing leaving the ventricle are compliant to simulate the aorta. Flow is controlled in this section of tubing using a manual clamp simulating circulatory systemic resistance. After the resistance, the fluid returns to the reservoir were it may initiate another cycle. This system is capable of physiologic and pathophysiologic flow and pressure waveforms. The left heart simulator has been described in previous articles and documents [16][18][63].

4.3 Ventricle chamber

The left ventricle chamber of the simulator is a quasi-rectangular acrylic chamber (Figure 4.3). The transparent nature of the chamber allows optical access to assess and record valve function. The upper frontal section of the chamber, which holds the aortic valve, forms a 135-degree angle with the frontal face of the chamber to emulate the geometrical positioning of the mitral and aortic valves. A 27mm Bjork-Shiley convexo-concave

mechanical valve is used in the aortic position. Two syringes connected through valves on the lid of the model are used as air compliance in order to reduce fluctuations in the
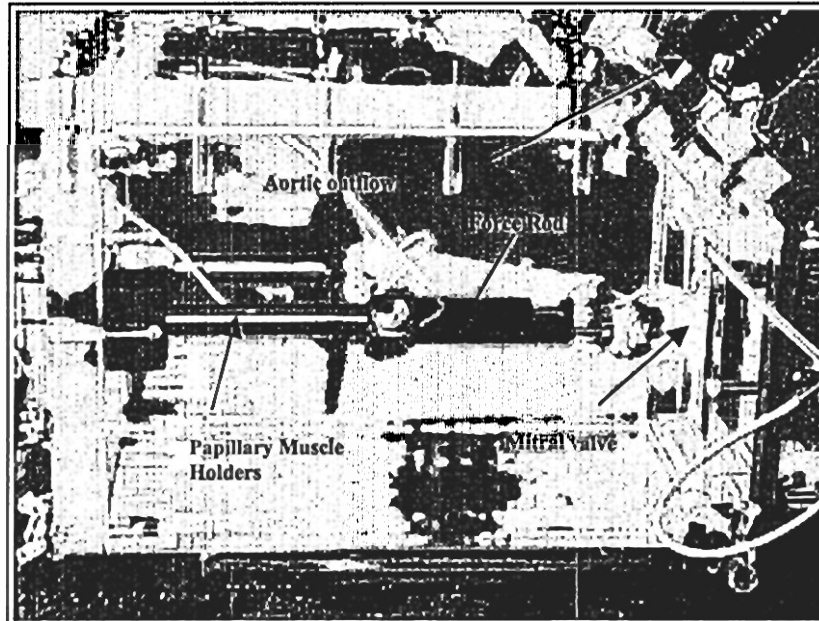
Figure 4.3. Photograph of the left ventricle chamber with papillary muscle positioning system and a native mitral valve (Jensen 2000).

pressure waves. The ventricular chamber has a papillary muscle holding system which allows three dimensional displacements.

4.4 Papillary Muscle Positioning System

As shown in Figure 4.4, the PM positioning system is composed of a main arm, an elevator, and a force rod. The main arm of the holding system slides through a tight fitting on the back plate of the ventricular chamber; allowing motion in the apical- basal

42

direction and also rotation. The elevator system is coupled to the main arm at 90-degrees. A hexagonal bolt through the middle of the elevator may be rotated; thereby, moving the force rod across the elevator. The aplica-basal sliding of the main arm, its rotation, and the rotation of the elevator screw allows this system to move the PM three dimensionally.
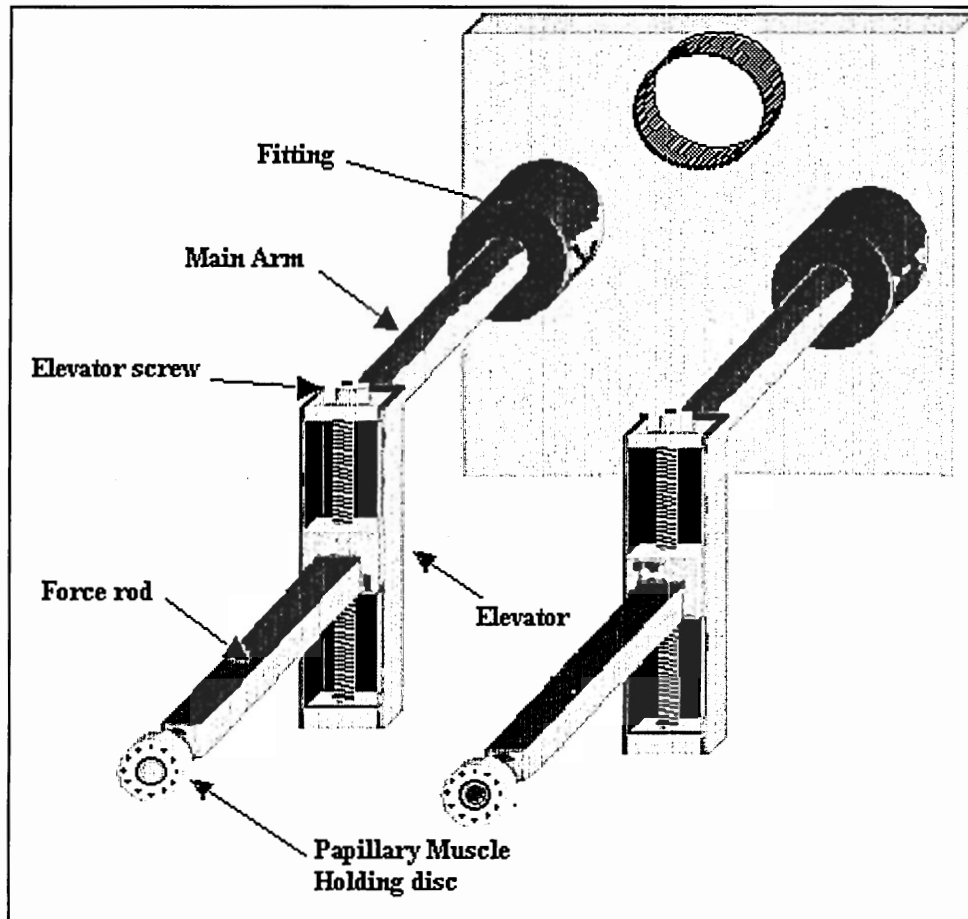
Figure 4.4 Assembly of the components of the papillary muscle positioning system. (Jensen 2000).

Exact positioning inside the flow loop is obtained by the controlled movement of the different components.

Displacements in the apical- basal direction are evaluated directly using a caliper or ruler and measuring the distance which the main arm slides from the backboard from one position to another. Lateral and anterior-posterior displacements are calculated from the interaction of the elevator and the rotation of the main arm. The rotation of the main arm is measured outside the loop using a protractor (Figure 4.5.a).
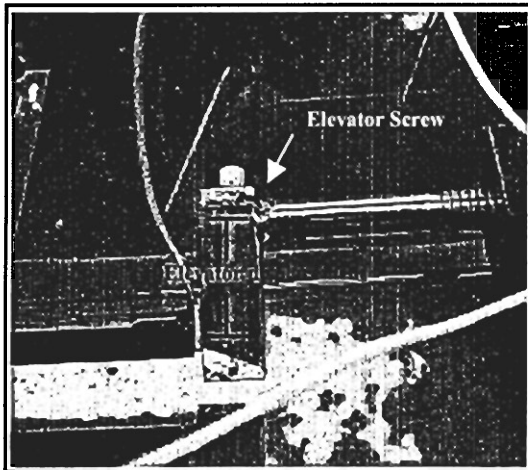
<div align="center">(a)</div>
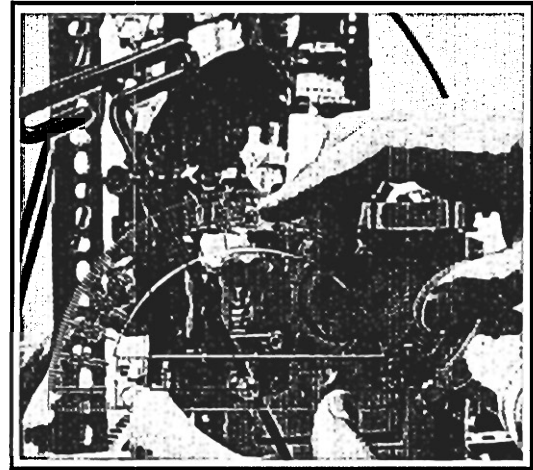
<div align="center">(b)</div>

Figure 4.5. (a) By rotating the elevator screw, the force moves through the elevator shaft. (6) Main arm rotation angle is measured with a protractor outside the flow loop.

The exact displacement of the elevator (Figure 4.5.b) is calculated from the rotation of the positioning screw (0.91mm/turn). It is necessary to use trigonometric equations to calculate the displacement in the elevator and the rotation angle required to attain exact positions. This is accomplished by using the cosine rule (equation 2):

$$a^2 = b^2 + c^2 - 2*b*c*\cos(A) \tag{2}$$

Using this system, exact displacements from a reference position may be obtained. A shortcoming of this method is that the ventricle chamber has to be open in order to move the positioning screw and change location.

4.5 Standard Atrial Chamber and Annulus Plate – Specific aim 3

The standard atrial chamber for the Georgia Tech left heart simulator has a rectangular volume of $229cm^2$ and a 2.5cm diameter inlet (Figure 4.6). The back board has an exit orifice of 4.5cm diameter in which the upper plate is attached to a cylinder used as air compliance. A valve on the right lateral wall is used to connect the pressure transducer, and a valve on top of the model is used to extract air during setup. This model uses a flat ring back plate to hold the mitral annulus. Details on the models construction and geometry are available in a previous publication [16].
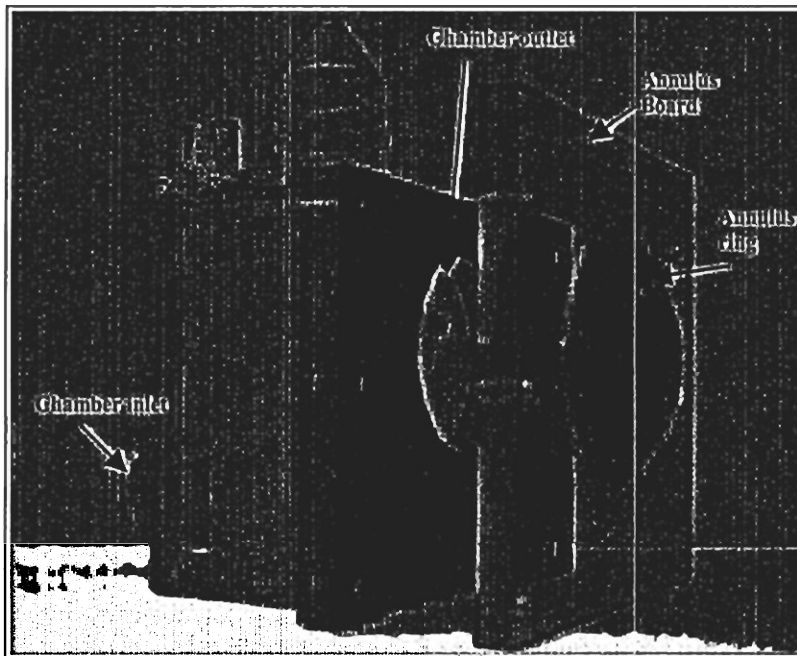
Figure 4.6. Standard atrial chamber for the Georgia Tech left heart simulator.

Both the variable shape annulus chamber and the flexible annulus atrial chamber are based on the standard Georgia Tech atrial chamber described previously. The basic differences lay in the mechanisms constructed around the annulus.

4.6 Variable Shape Mitral Annulus Chamber (Flat – Saddle) – Specific Aim 1

A variable annular shape atrial chamber (VASAC) was constructed to obtain the different annular geometries during the *in vitro* experiments (Figure 4.7). This chamber was used along with the Georgia Tech left heart simulator. Detailed blue prints of this chamber are available in Appendix A.
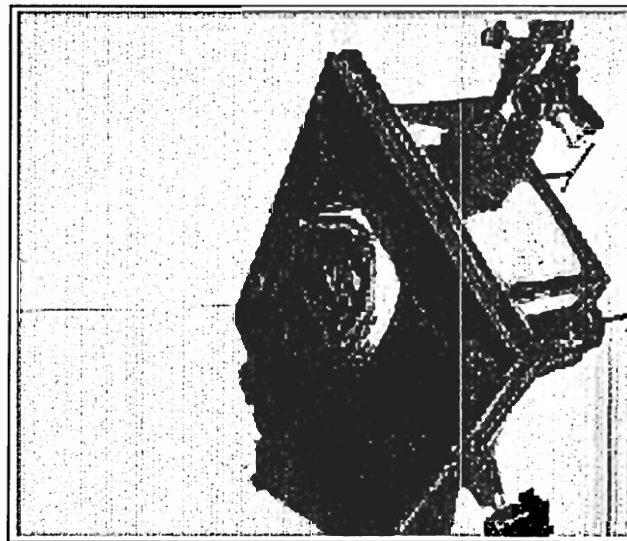
Figure 4.7. Photograph of the variable shape annulus chamber in the saddle configuration.

The atrial chamber was constructed of 3mm transparent acrylic plates, enabling visualization and echocardiographic imaging of the valve through a frontal window 5cm

away from the annulus. The chamber has a rectangular volume of 229cm^2, and an inlet diameter of 2.5cm. The annulus ring was composed of a multi-link chain which deformed three dimensionally (Figure 4.8), but retained an approximately constant 3D perimeter
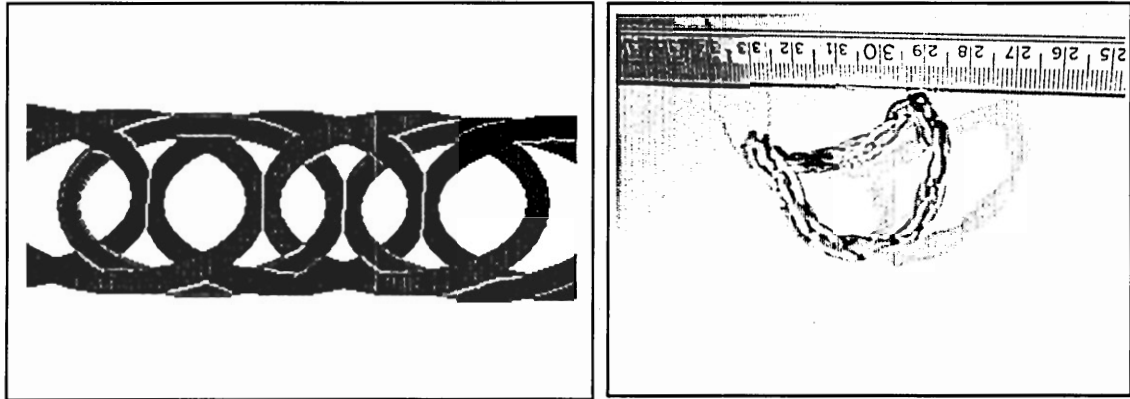
(a)   (b)

Figure 4.8. (a) Schematic of the linking pattern of the chain used for this model. (b) Photograph of the multi-link chain forming a three-dimensional saddle geometry.

(maximum perimeter variation = 3%). The chain structure is characterized by a connection pattern were to sequential links (identified in Figure 4.8a by color), are joined together by two other individual links, which are also sequentially connected to each other. The chain had a perimeter of 11cm, and each segment of chain was joined by three parallel links. In the flat configuration, the commissure-commissure diameter was approximately 3.6cm and the septal lateral diameter was 2.3 cm. A 2cm section of chain links were welded together using epoxy (Epoxy bond, Atlas Minerals & Chemicals, PA,USA) to generate the D-shaped geometry characteristic of the mitral annulus orifice. Two straight control rods, connected at one end to the center of the commissural sections

of the annulus, were used to modulate annular shape. These control rods slide through couplings in the frontal wall of the chamber. This mechanism is maintained water tight by o-rings. Moving the control rods in the forward direction pushed these sections of the annulus forward, transforming the initially flat ring into a geometry similar to that of a saddle.
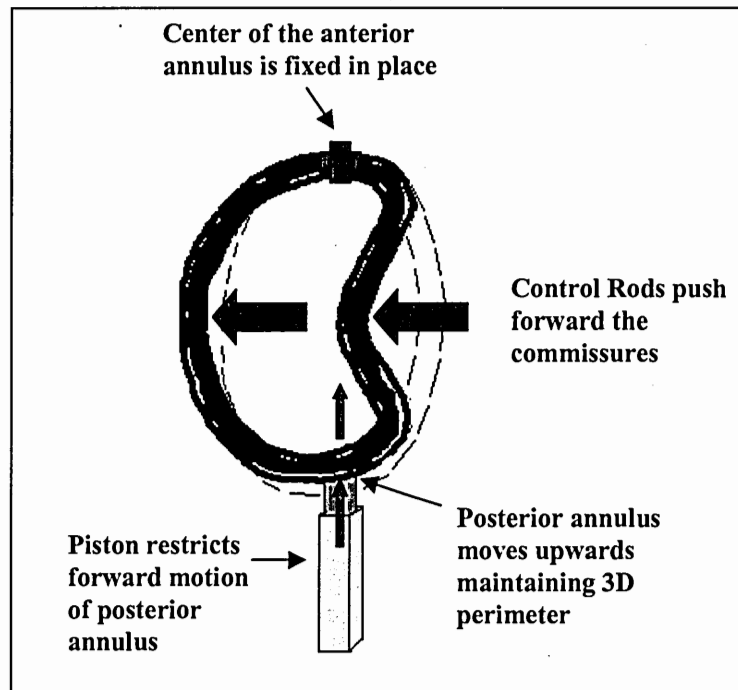
Figure 4.9. Diagram of the mechanism which shifts the shape of the annulus from a flat ring to a 3D saddle.

The annulus was held fixed at the middle of its anterior section and was connected to a small metallic piston at the midpoint of the posterior section (Figure 4.9). The piston was a 1.5cm long steel rod with a diameter of 3mm. The shaft was a hollow square bronze rod, with a length of 2cm and an internal side length of 3.8mm. Therefore, the piston mechanisms provided a loose fit allowing easy motion of the piston. Because of this

design, when the rods were pushed forward to generate the saddle, the commissural section protruded into the ventricular cavity and the anterior section of the annulus was fixed in place (Figure 4.10). Since the perimeter was constant, the posterior section of the
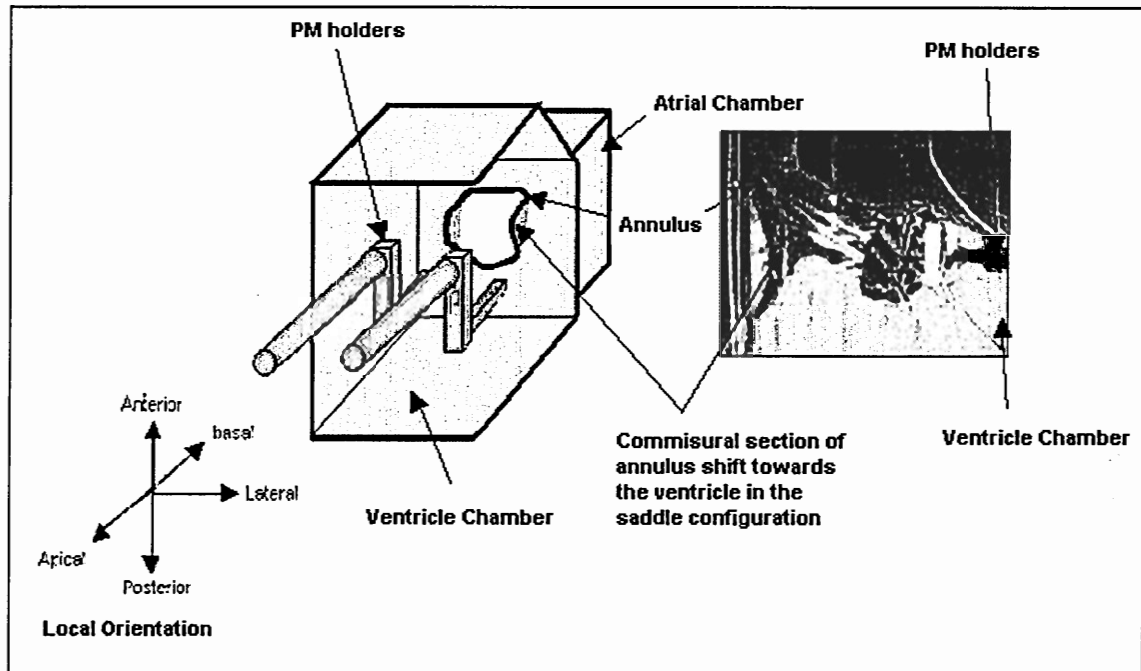
Figure 4.10. Schematic of the saddle shape configuration setup and local orientation.

annulus moved upward, reducing the septal – lateral diameter of the valve. The piston was used so that the posterior section of the annulus did not move apically, only septal-laterally. This variation in annular septal-lateral diameter is observed in the native mitral valve when going from a semi-flat structure in diastole to a three dimensional saddle in systole [3]. The whole ring is wrapped in a Dacron cloth allowing for extra support and the suturing of the valve.

The annulus was also sutured to a red silicon membrane (1.5mm thick) which deformed when shifting annulus shapes. This membrane kept a water tight seal around the annulus ensuring that fluid only went through the valve. The space behind the membrane in the saddle configuration was filled with plasticine to avoid membrane motions which may promote inaccurate readings in the flow transducer. When in the flat configuration the membrane bulged forwards because of the plasticine.

Annular geometry varied from a completely flat ring with an approximate orifice area of $6.8cm^2$ to a saddle shaped geometry with saddle height of 9mm. This resulted in a reduction of septal-lateral diameter of 3mm, and a projected two-dimensional orifice area of $5.4cm^2$. A saddle height of 9mm was selected because it represents an intermediate point within a disparity of measurements recorded in previous studies by other researchers [3], [33]. The annular area and annular area variation were within ranges observed clinically during the cardiac cycle [3] [33].

4.7 Flexible annulus model – Specific aim 2

A flexible annulus model was incorporated into the standard atrial chamber in order to simulate annular flexibility and displacement. The standard Georgia Tech simulator atrial chamber was coupled to two 10cm×11cm (5mm and 8mm thick) acrylic plates through four 2.7cm long (1cm × 1cm) square beams (Figure 4.11). Bolts extending from the beams, were locked with nuts onto the atrial chamber, so that these to parts may be separated in order to replace the membrane if necessary. The two plates have rectangular orifices 7cm × 6cm, which allow membrane movement. Between these two plates, a
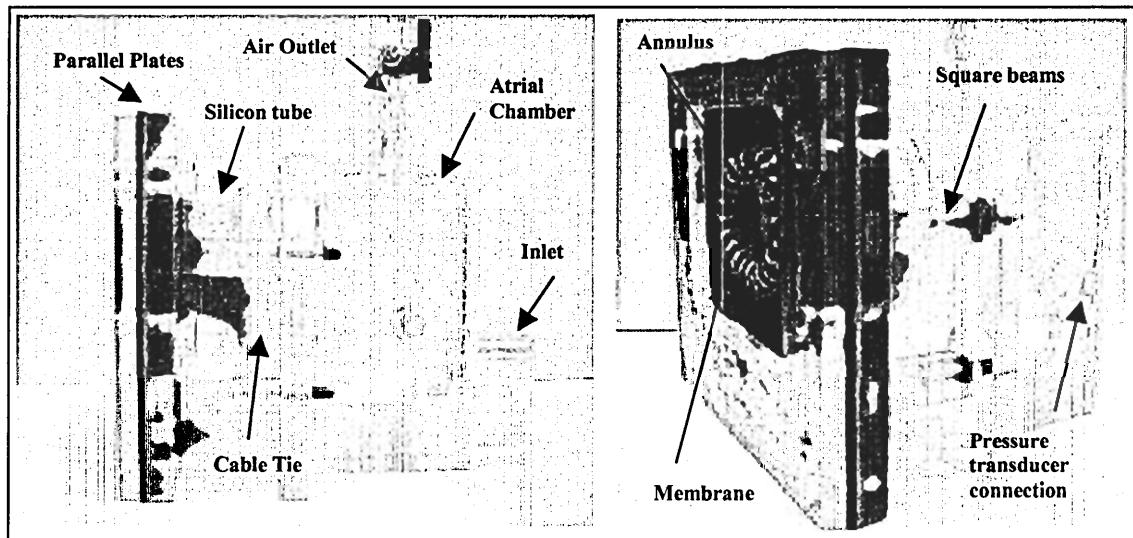
Figure 4.11. The flexible annulus model and its different components.

1.5mm thick silicon membrane was locked in place using a bonder (Krazy glue, Elmer's Products, OH, USA). The membrane is also help in place during the experiment because of the compression induced by the four wing nuts which lock the atrial chamber on the ventricular chamber in the model. The flexible membrane and the annulus are connected to the standard chamber by a silicone tube. This tube has a diameter of 3.5cm, a length of 2.8cm, and wall thickness of 0.5mm. The silicon tube is attached to the membrane by 2-0 sutures (braided silk, Ethicon, NY, USA) and transparent silicone (Silicone II, General Electric, NC, USA). The other end of the silicone tube was attached to the atrial chamber using a plastic cable tie (clamp ties, CTT60R, Cole-Parmer Instrument Co, USA), which held the silicon tube onto the atrial chamber outlet (Figure 4.11). This connection between the chamber and the membrane was selected so that the movement of the membrane would not produce inaccurate mitral flow readings. If the membrane had been

attached directly to the atrial chamber, the movement of the membrane would displace

fluid volume altering the flow curves in the transducer. The annulus on this model was
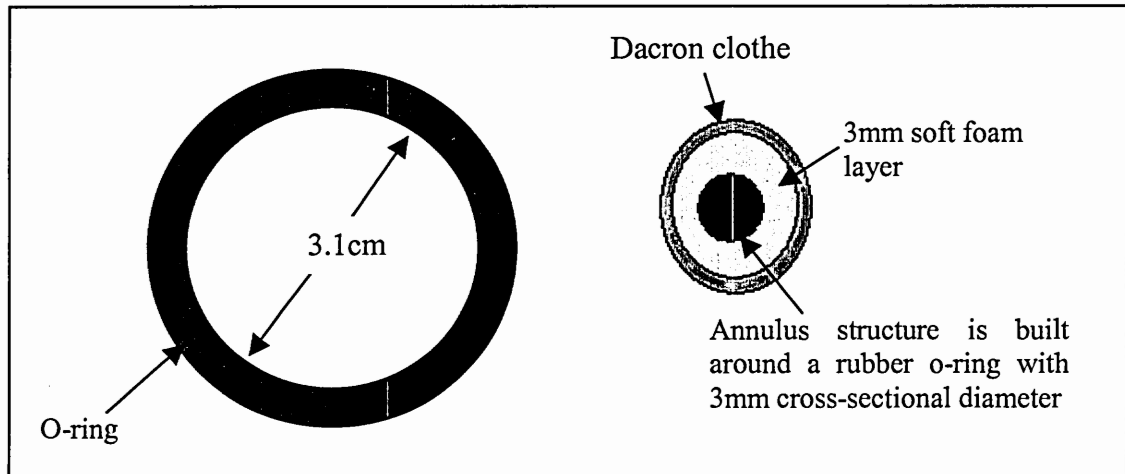
Figure 4.12. Schematic of the components of the annulus of the flexible atrial chamber.

designed to be soft and flexible. The annulus was constructed with a rubber o-ring. The

o-ring had a diameter of 3.1cm, with a 3mm circular cross section (Figure 4.12). The o-

ring was covered with a layer of 3mm soft foam, which was then encapsulated in Dacron

cloth using 3-0 suture (braided silk, Ethicon, NY, USA). Generating the D- shape

characteristic of the mitral annulus, the Dacron cloth was then sutured onto the membrane

using the same 3-0 suture. When the annulus was in place, the Dacron cloth and the area

connecting to the membrane were sealed using transparent silicone.

Initial tests were carried out with this model to assess if membrane displacement was

within physiological ranges. The mitral orifice was sealed and the atrial chamber was

coupled to the heart simulator. The pressure in the ventricle was increased up to

120mmHg, and at this point the membranes displacement from its initial position was

measured. The membrane displaced 8mm, which is within ranges observed clinically [5].

Detailed blue prints of this chamber are available in Appendix A.

4.8 Strain Gauge Transducers and Force Rods
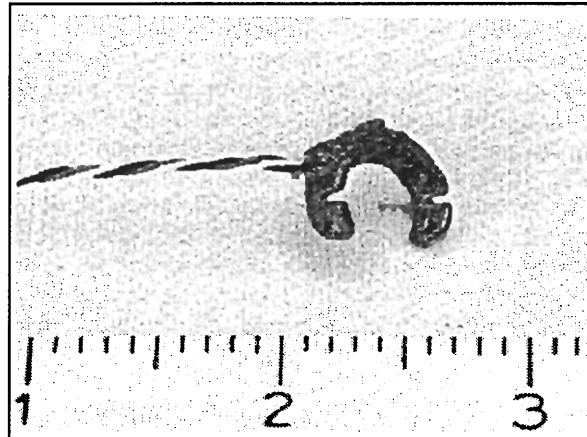
Figure 4.13. Scale photograph of a c-ring force transducer.

C-shaped transducers with strain gauges were used to measure the tension on individual

chordae tendineae during the dynamic testing of the valve. The aforementioned c-ring

transducers were constructed of a c-shaped brass ring 6mm in diameter, 2mm wide, and

0.5mm thick (Figure 4.13). Two strain gauges (model: EA-06-031DE-350,

Measurements Group, Raleigh, NC) were attached to the inner and outer surfaces of the

ring, comprising a Wheatstone half-bridge. The overall weight of the transducer was less

than 80 mg. The strain gauges were coupled with an in-house amplifier box comprising

the remaining half of the Wheatstone bridge. The transducers were coated to maintain

electrical stability while testing inside the 0.9% saline solution media. The sensitivity (0.5

Newtons/Volt aprox.) and linearity (0-5 Newtons) of individual transducers was tested

prior to and after each experiment. The minimal measurable difference in tension for these transducers was ($0.5N/V*1.22mv = 6.1x10^{-4}N$) when coupled to the DAQ 1200 PCMCIA data acquisition card (National Instruments, TX, USA).The voltage baseline was zeroed immediately before dynamic testing. Applications of these c-rings force transducers have been presented in previous publications [11], [42]. Details of c-ring construction and function are shown in Appendix B.
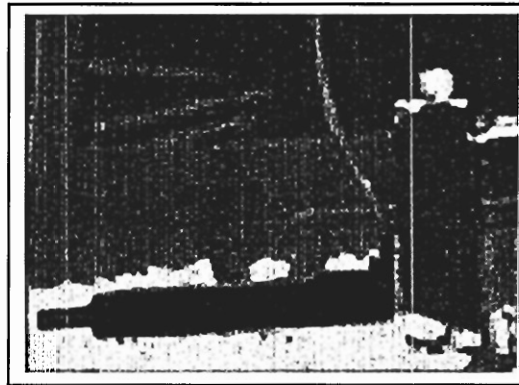
Figure 4.14. Force rod mounted on the papillary positioning system.

The modified Georgia Tech left heart simulator used force rods (Figure 4.14), enabling the system to measure the total force applied on each papillary muscle. The rods were constructed of hollow brass tube with Kulite semiconductor strain gauges (Type AGP 350-90, Teledyne Brown Eng.) arranged as Wheatstone bridges to measure both tension and bending moments. The rods are coated with Conathane EN-12 Part B polyurethane casting resin, which maintained the electrical integrity of the rod when testing in saline solution. These rods were coupled to an independent in-house amplifier connected to a voltmeter (FLUKE 27, Everett, Washington). The sensitivity and linearity of the rods was tested before the experiments. This system was used as a reference ensuring a comparable

force on both PMs and maintaining approximately the same force conditions when changing annular shape. The detailed construction and function of these rods has been described in previous publications [16],[63].

4.9 Echocardiographic Imaging and Video

A Diagnostic Ultrasound System SSA-270A with a 3.75MHz phased array transducer (Toshiba Corporation, Japan) was used to evaluate valve performance. Ultrasound gel (Aquasonic 10, Parker Laboratories, NJ, USA) was used between the atrial window and the ultrasound transducer to enhance the images of the valve. The imaging depth of the transducer was 5cm to 8 cm from the valve's annulus and reached an additional 6-8 cm downstream of the valve. Initially 2D-B-mode images of the mitral valve were acquired to observe the movement of the leaflets and closure characteristics. Image depth setting on the machine ranged from 12cm to 15cm, and gain was adjusted according to image quality. 2D-B-mode images from the front of the atrial chamber are similar to those obtained *in vivo* from an esophageal view [16]. These images were important in assessing proper closure of the valve and location of the coaptation with respect to the septal-lateral diameter.

Color 2D-B-mode Doppler velocity mapping was used to monitor valve function and regurgitation. Color images of the flow through mitral valve were obtained at the same depth as the normal 2D-B-mode images. A scan window width angel of approximately 30 degrees was used for these images. The presence of bubbles and the absence of particle inside the fluid limited the quality of these images. Color Doppler images showed

anterograde flow (away from the ultrasound probe) in blue and retrograde flow (towards the ultrasound probe) in red. Therefore, the presence of red jets across the valve while closed was characterized as regurgitation. Both echocardiographic images and lateral views of the valve in the simulator were stored on video. A digital camera (Sony Digital Handycam, Model DCR-TVR 310, Sony Corporation, Japan) was used to record these images.

4.10 Instrument Calibration
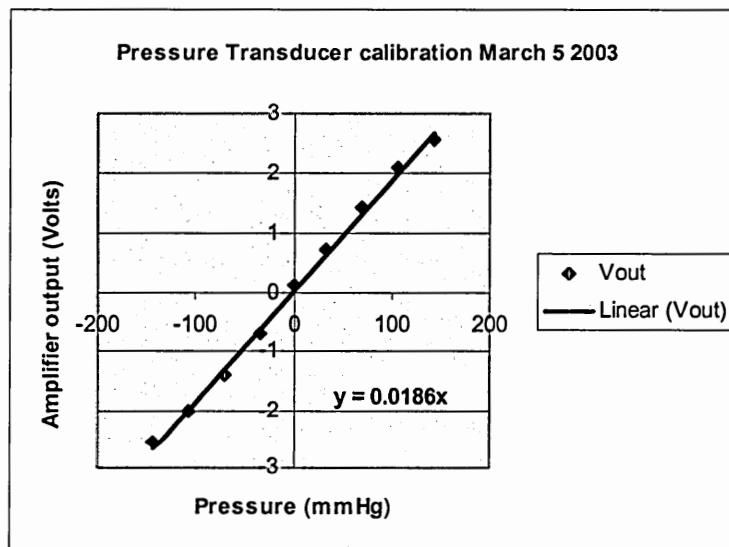
Figure 4.15. Calibration curve for trans-mitral pressure transducer.

The trans-mitral pressure transducer was calibrated using a differential water column. Each chamber was calibrated independently and the voltage output of the pressure transducer amplifier was recorded and plotted against the water column differential

pressure to obtain the sensitivity of the system. An example of a calibration curve for this transducer is presented in Figure 4.15.
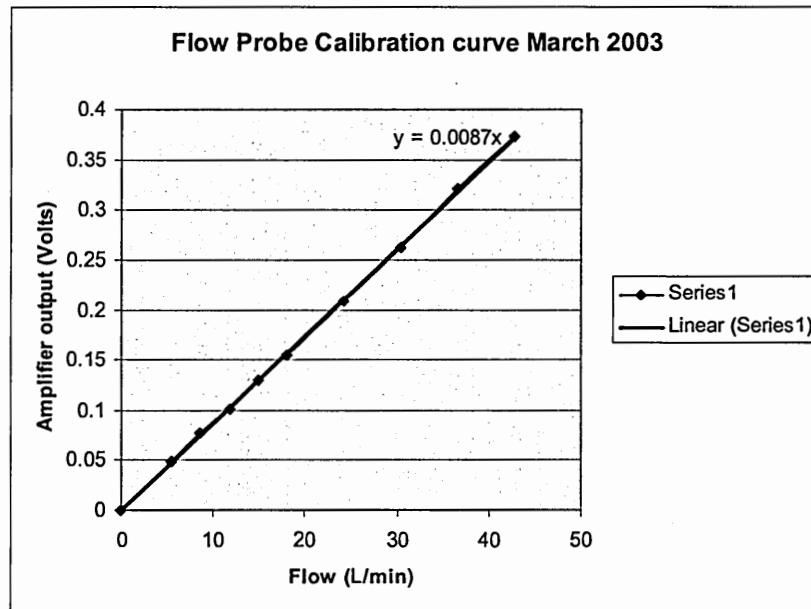
Figure 4.16.Typical calibration curve for the left heart simulator flow prove.

The flow transducer was also calibrated using a precision flow rotometer. Both the rotometer and the flow transducer were connected in series to a steady flow pump in a loop. Average flow in the system was varied and the output of the voltage of the flow amplifier and the rotometer flow were recorded. Figure 4.16 shows a typical calibration curve for the flow probe.

Detailed calibration procedures for both the flow and the pressure transducer are available in a previous publication [16].

The c-ring tension transducers were calibrated before and after each experiment. After each c-ring was zeroed in the amplifier, known weights were suspended to induce a voltage variation. Output voltage was plotted against applied tension to obtain the
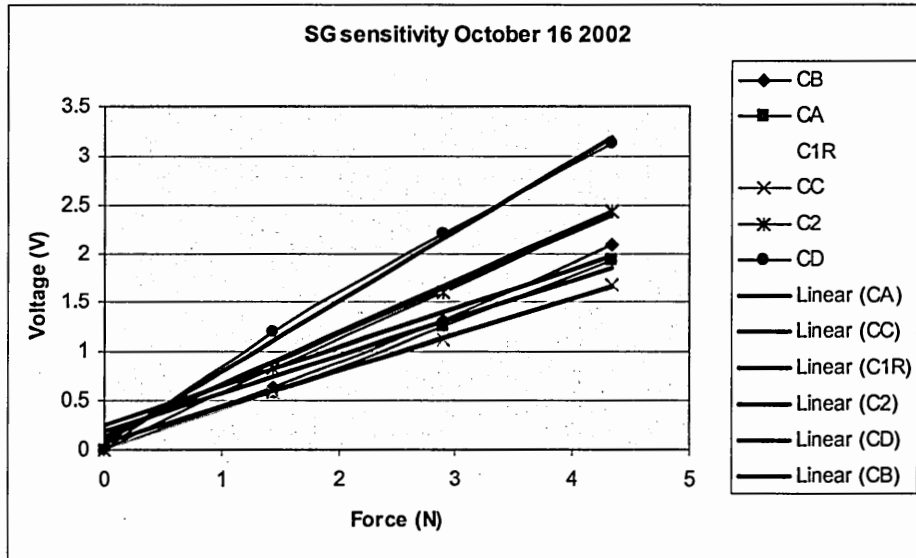
Figure 4.17. Sensitivity curves for c-ring force transducers (October 16/ 2002).

sensitivity of each c-ring (Figure 4.17). Details on calibration and c-ring behavior are presented in Appendix B.

4.11 General Experimental Protocol

After valve extraction, the PMs were wrapped with Dacron cloth maintaining the chordae distribution intact. This Dacron cloth was then sutured onto PM holding disks designed to attach to the left heart simulator. Each valve was then sutured onto the annulus of the appropriate atrial chamber model according to the specific experiment that would be performed (Standard flat annulus, variable annulus shape model, or flexible annulus model) using 3-0 sutures (braided silk, Ethicon, NJ, USA). During suturing, special attention was placed on preserving the annular perimeter to avoid dilation or contraction.
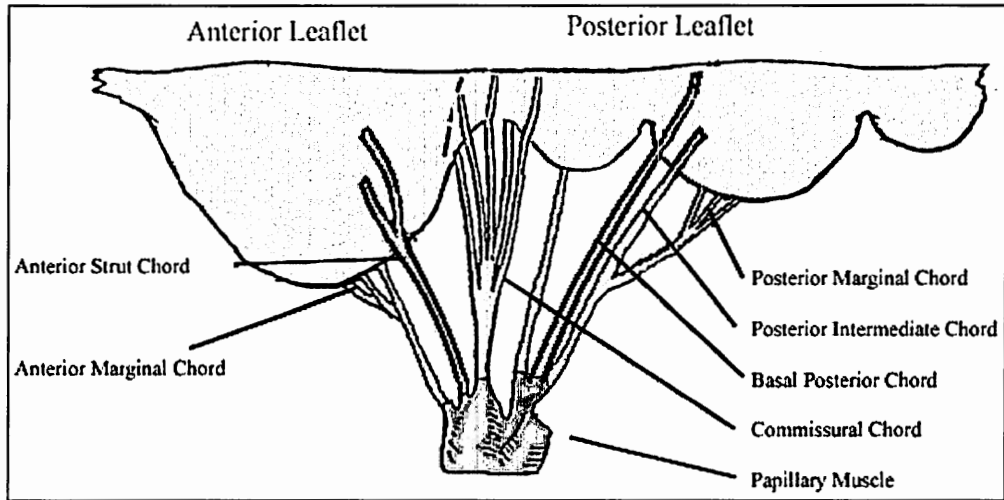
Figure 4.18. Diagram of an extended mitral valve identifying the chordae tendineae selected for tension measurements.

Figure 4.19. Mitral valve sutured onto the standard annulus board. Red arrows indicate c-ring force transducer. Four transducers are attached to chords extending from the anterior papillary muscle, while two are implanted on chords from the posterior papillary muscle.

Six c-rings were individually sutured onto the following chords: anterior strut chord, anterior marginal chord, posterior intermediate chord, stem of the posterior marginal chord, basal posterior chord, and commissural chord (Figure 4.18). It was not possible to attach all c-rings onto chords extending from a single papillary muscle because of spatial constraints that could cause c-ring entanglement (Figure 4.19). Chords were selected according to thickness and implantation feasibility. When suturing the c-rings onto the chords, 5-0 sutures (braided silk, Ethicon, NJ, USA) were used to fasten to the chord preventing the ring from slippage or detachment. Details of the attachment method are presented in appendix A.
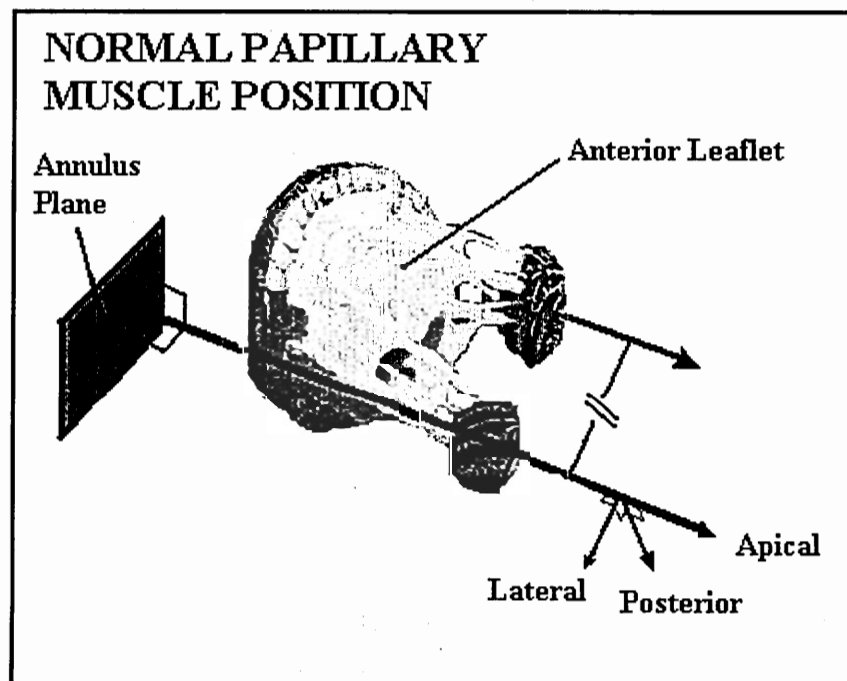
Figure 4.20. Descriptive diagram of the normal papillary muscle position.

The atrial chamber, containing the sutured MV was positioned in the left heart simulator.

The c-ring cables were then connected to the in-house c-ring amplifier box using the same channels they were calibrated with. The PMs were attached to the force rods and the left heart simulator was then filled with 0.9% saline solution. All transducers and c-rings were zeroed and connected to an in-house interface box; which was then connected to a laptop computer.

After preparing the system, the valve was placed in the defined normal PM position (Figure 4.20). The normal position was defined by[44]:

- *Basal-apical location*: The papillary muscle rods were moved towards the annulus to a point where slack was observed in all the chordae tendineae. The papillary force rods were zeroed at this location. Each force rod was pulled backwards until a change in voltage of 0.02volts (0.09Newtons) was achieved for that particular rod. This was the minimal significant change that may be observed by the system. This defined a position with no slack or apparent tension on the chordae tendineae.

- *Lateral Location*: The papillary muscles arranged parallel to each other and directly aligned with the valve's annulus on each commissure. The commissural chords inserting in the annulus were vertically perpendicular to the annular plane.

- *Septal-lateral location*: The rods were moved septal laterally until an even extension of the commissural chords inserting into the annulus was observed. Normally, this point was a couple of millimeters below the annular height midpoint.

Valve function in the normal PM position was confirmed under pulsatile flow by observing appropriate leaflet coaptation using 2D echocardiografic images, and color

Doppler images of the flow. Valve function was filmed through the ventricular chamber using the digital camera. When using the flexible annulus model (specific aim 2), additional images of the base of the annulus were recorded (perpendicular to its motion) in order to measure annular displacement.
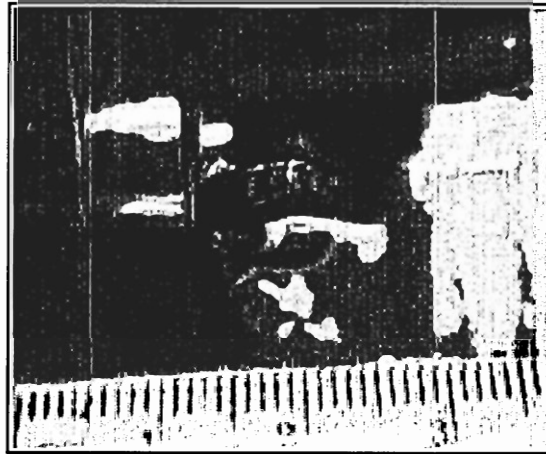
Figure 4.21. Lateral view of the atrial side of the flexible membrane used as reference to observe annulus displacement.

As observed in Figure 4.21, a ruler was placed near to the silicon tube that connected to the base of the annulus. The motion of the annulus was recorded in video. A software package (WinTV 2000 Version 3.39, Hauppauge computer works, NY) was used to convert the video images to AVI files using a PCI interface board (WinTV GO, Hauppauge computer works, NY).Using the same software, JPEG frames of the minimum and maximum apico-basal annulus displacement positions were generated from the AVI files. The limit between the membrane and the tube was used as reference to measure annulus displacement. Annulus displacement was calculated from these images using Sigma Scan Pro software (Sigma Scan Company, version 6.0, NY). This software provided pixel coordinates of reference points for the two JPEG frames. The know

distance from the ruler in the images was used to calculate the displacement in millimeters.

The simulator ran under physiologic conditions with the valve in the normal position (cardiac output: 5 l/min, peak trans-mitral pressure: 120 mmHg, heart rate: 70 BPM, systolic duration: approx. 300ms). Flow, tension, and pressure curves were saved on a laptop computer for offline processing. Data representing ten cardiac cycles for each variable was stored.

4.11.1 Specific Aim 1- Using the Variable Shape Mitral Annulus Chamber

After the initial set of recordings with the flat annulus, the shape of the annulus was shifted to the saddle configuration. The papillary muscles were then displaced apically to compensate the forward movement of the commissural section of the annulus in the saddle configuration. The force rods were used to ensure that the same force was applied on the papillary muscle in both the flat and saddle configurations. All the previously described data acquisition, video, and Doppler recordings were performed at this new annulus configuration using the same physiological flow conditions (Cardiac output: 5 l/min, peak trans-mitral pressure: 120 mmHg, heart rate: 70 BPM, systolic duration: 300 ms).

After completing all recordings and storing the appropriate curves on the computer, both PMs were moved 5mm apically, 5mm laterally, and 5mm posteriorly from the normal position. This constituted the symmetrically tethered papillary muscle position, which was used to induce mitral regurgitation. All the previously described data acquisition,

63

video and Doppler recordings were performed at this new PM position using the same physiological conditions for both the flat and saddle annulus configurations.

4.11.2 Specific Aim 2- Using the Flexible Annulus Model

Using the flexible annulus model, and after the initial set of experiments in the normal PM position; Both PMs were moved 5mm apically, 5mm laterally, and 5mm posteriorly from the normal position. This constituted the symmetrically tethered papillary muscle position, which was used to induce mitral regurgitation. All the previously described data acquisition, video and Doppler recordings were performed at this new PM position using the same physiological conditions.

4.11.3 Specific Aim 3- Using the Standard Atrial Chamber

Table 4.1. Vectorial decomposition for the different papillary muscle positions.

Papillary Muscle Position	Apical Displacement (mm)	Lateral Displacement (mm)	Posterior Displacement (mm)
000	0	0	0
005	0	0	5
050	0	5	0
055	0	5	5
500	5	0	0
505	5	0	5
550	5	5	0
555	5	5	5

After the initial set of recordings, the PMs were displaced to eight different papillary muscle positions. The reference for all these displacements was the normal PM position.
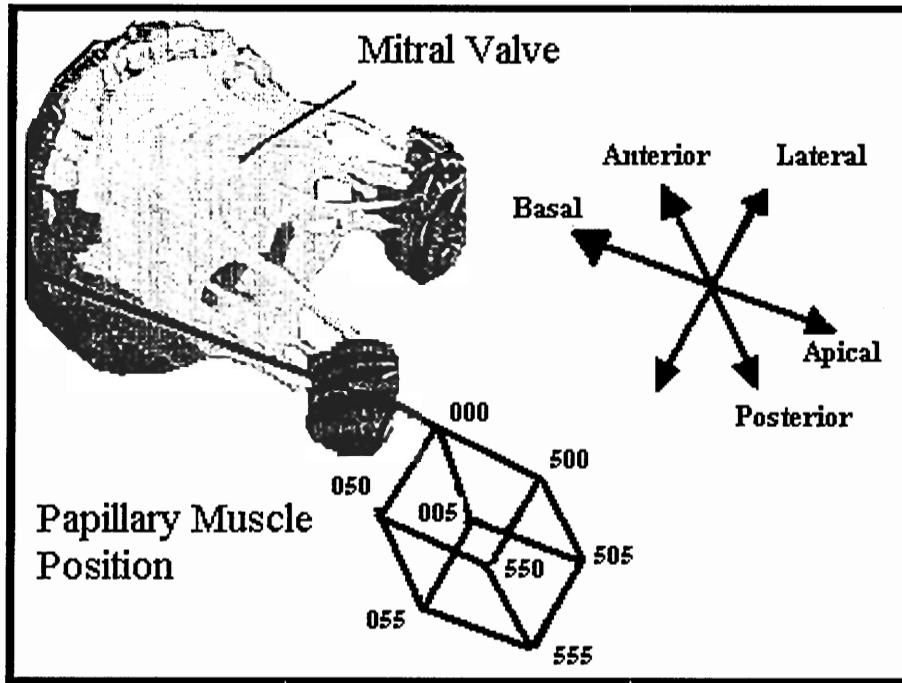
Figure 4.22. Spatial reference system based on the normal papillary muscle position. The edges of the cube represent the eight different experimental positions used in the study.

All displacements were symmetrical; therefore both PMs were displaced equally to reach each position. Only symmetric positions were tested because it was not possible to attach all six c-rings on the same PM; therefore, special care was taken on having the same average force on the PM in the normal position. The eight different positions are presented in Table 3, with their corresponding vectorial displacement from the normal position. A schematic of the spatial reference system is presented in Figure (4.22). All recordings were repeated for all the different PM positions maintaining the physiological flow and pressure conditions previously described.

4.12 Data Analysis and Acquisition

To acquire data, the left heart simulator uses an in-house interface box, which receives analog voltage signals from the transducers. The interface box transfers these signals to a PCMCIA data acquisition card (Daq-card 1200, National Instruments, TX, USA). This card has eight different channels, which may be synchronized by a trigger. During the experiments one channel was used for flow, a second channel was used for pressure and the other six channels transferred readings of chordal tension. DAQ-ANAL 2.1, an in-house data collection program based on LabVIEW 5.0 was used to store the flow, pressure, and chordal force curves on a laptop computer. This program acquired data every 2ms from the eight channels. The program automatically stored data for ten cardiac cycles for each variable. The curves for the ten stored cardiac cycles were averaged and analyzed offline using the data analysis tool of DAQ-ANAL, which generated excel spreadsheets. The data analysis tool also allowed the user to delete curves that appeared to be deficient before averaging. Excel was employed to analyze, plot, and store the averaged curves of each of the variables. Macros in excel were used to correct the diastolic baseline for all the curves and find the peak values for each variable during the cardiac cycle. The data acquisition system and the Daq-Anal 2.1 software have been described in detail in a previous publication [16].

4.13 Statistical Analysis

All data are reported as the mean $\pm$ 1 standard deviation unless otherwise stated. Means were generally compared using two-tailed t tests for paired comparisons in experiments

when the valve was used as its own control to reduce natural variability. When comparing data with different sample sizes or when appropriate, unpaired two-tailed t tests were used. The Anderson- Darling test was used to observe if the chordae tendineae tensions were normally distributed. This test was performed for the tension data in the normal papillary muscle position, which is representative of normal valve function. Statistical analysis was carried out using Minitab (version 13.32) software.

CHAPTER V

PRELIMINARY EXPERIMENTS

5.1 Anatomical Measurements

The basal chords from six human mitral valves were measured. The valves were sutured to a flexible membrane held by a rigid circular metallic ring. The papillary muscles were positioned so that there was no slack in the chords inserting near the annulus of the valve. The lengths of the individual basal chords were measured from the origin in each papillary muscle to their point of insertion. Only chords inserting into the base of the leaflets were measured in order to analyze the geometry generated on the annulus when these chordae were under tension. The lengths of the chords were recorded in an insertion map of the valve. After these measurements, the flexible membrane was moved 1cm
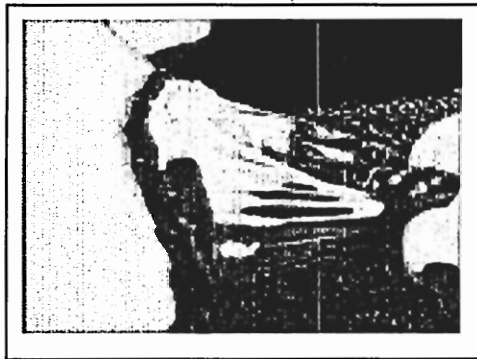
(a)   (b)

Figure 5.1. A) Mitral valve sutured on a flexible membrane. B) The saddle configuration is present in the annulus when the basal chords are extended.

away from the papillary muscles to observe the geometry generated on the annulus (Figure5.1a). The membrane was used to hold the valve, while enabling the annulus to deform according to chordal lengths.

5.2 Results of Anatomical Measurements and Observations
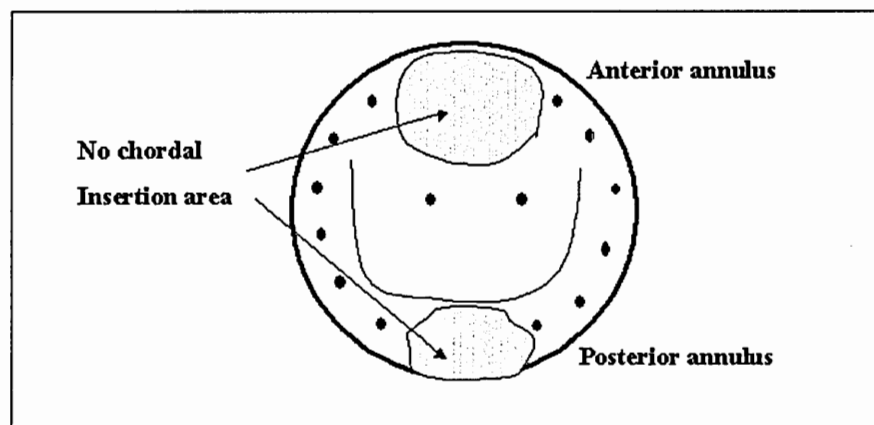
Figure 5.2. Diagram of the chordae tendineae insertion pattern.

The anatomy of all valves showed dense chordae insertion in the commissural regions near the annulus when compared to the other areas of the mitral valve. The midsections of the base of the anterior and posterior leaflets showed no direct insertions. The base of the anterior leaflet presented a larger area free from basal insertions when compared to the base of the posterior leaflet, as shown in Figure 5.2. The chordae inserting into the central commissural areas adjacent to the annulus (27.5 ± 0.9mm anterior PM, 25.6 ± 0.7mm posterior PM) were significantly shorter than those inserting above and

below this location (36.5±3.5mm anterior PM, 37.0±3.8mm posterior PM. Average lengths for the anterior PM are presented in Figure 5.3.
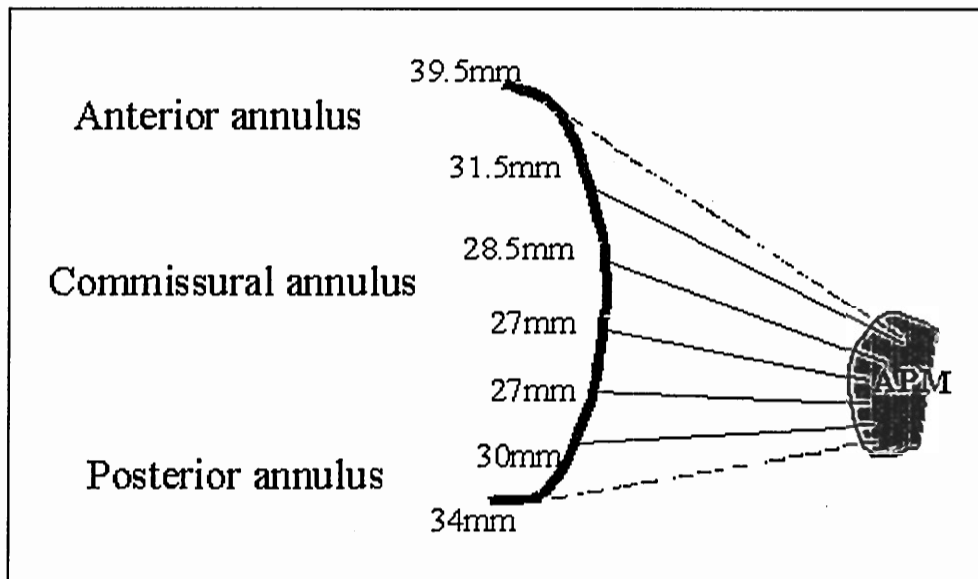
Figure 5.3. Lateral diagram of the mitral valve with average chordal lengths.

The mitral valves mounted onto the flexible membrane showed a saddle shape annular configuration when the PMs were moved away from the annulus (Figure 5.1.b). The different lengths of the basal mitral chords and their insertion pattern are responsible for the saddle curvature.

CHAPTER VI

RESULTS

6.1 Overview

The results for this study are divided into three main sections according to each specific aim. In all experiments, data for each variable were acquired for ten cardiac cycles and averaged using the DAQ-ANAL data analysis tool [16]. The results were statistically analyzed using the student t-tests to assess statistical significance. For specific aim 1 and specific aim 3, paired t-tests were used to compare the measurements to reduce differences associated with natural variability between valves. Since experiments in specific aim 1 were performed using fixed annuli, the results for specific aim 2 were compared to those in specific aim 1 to asses the effects of introducing annular displacement on chordal tension and mitral regurgitation volume. Since the valves used for specific aims 1 and 2 were different, there was no natural pairing; therefore, unpaired student t-tests were used for these comparisons. All the chordae tendineae tensions for the normal papillary muscle positions were tested for normality using the Anderson-Darling test. This test showed a normal distribution of the data ($p<0.001$).

In this study, measurements were only excluded because of the technical limitations of the transducers. Peak systolic tension measurements under 0.01N were discarded, as they could not be distinguished from electrical crosstalk. The C-rings were calibrated before

and after each experiment to assess transducer functionality and linearity. Measurements for individual chords were discarded after each experiment only if the transducer showed malfunction during post-experimental calibration.
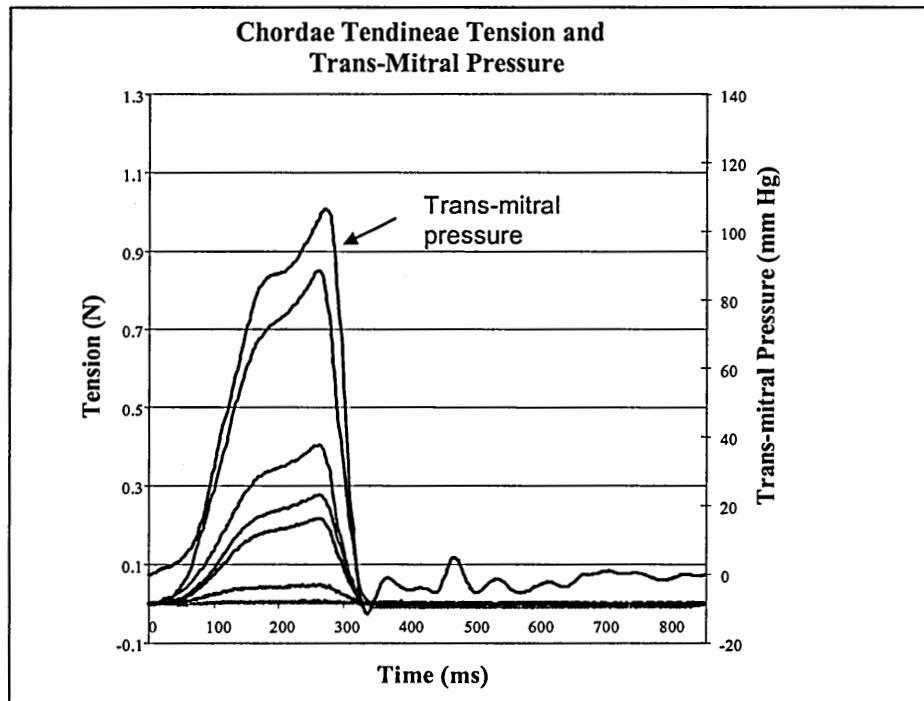
Figure 6.1. Typical plot of chordae tendineae tension and trans-mitral pressure during one cardiac cycle. The graph shows how tension curves follow the trans-mitral pressure curve.

As shown in Figure 6.1 the chordae tendineae tension (CTT) curves followed the trans-mitral pressure curve. This characteristic was observed for all valves (porcine and human) studied. Chordae tendineae tension curves were plotted against time during one cardiac cycle. Diastolic tension was considered as baseline for the CTT curves [11] [42]. Representative plots of chordae tendineae tension and trans-mitral pressure for the three specific aims are presented in Appendix C. Data on mitral regurgitation volume and peak

systolic tension (PST) for all experiments are presented in Appendix D. Raw data and processed excel spreadsheets for all experiments are cataloged and available on CD1.

6.2 Experimental Conditions

All the experiments in this study were conducted under physiological conditions described in the Methods section. Average trans-mitral pressure was 120±1mmHg and cardiac output was 5.0±0.1L/min. The peak trans-mitral flow rate was 18.6±2.2L/min, while mean systolic duration was 283±20ms. Pressure and flow curves for the system had physiological characteristics as observed in Figure 6.2.
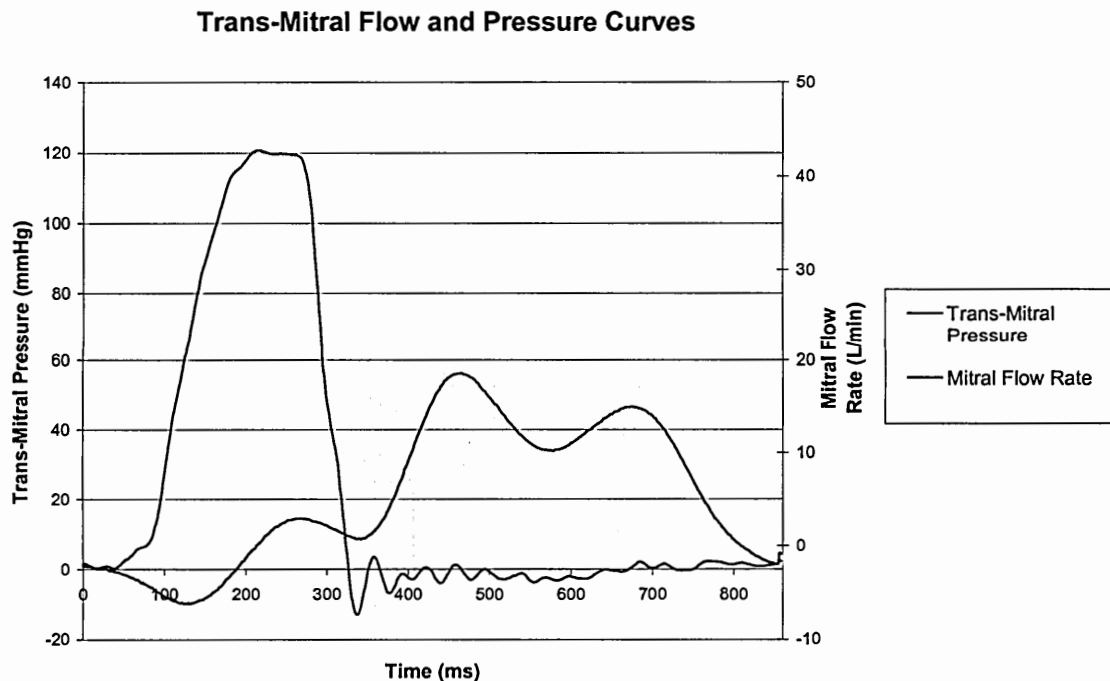
Figure 6.2. Physiological mitral flow and trans-mitral pressure curves from the left heart simulator.

6.3 Results for Specific Aim 1: Effect of Annular Shape

6.3.1 Valve Function

Eleven human valves were studied at 120±2mmHg peak trans-mitral pressure and cardiac output of 5.0±0.1 L/min using the variable annulus shape atrial chamber.

In the defined normal PM position, for both the flat and saddle annular configuration, the valves coapted well showing no regurgitant orifices along the coaptation line or leakage in the echocardiographic images. Apical posterior lateral displacement of the PMs induced tented leaflet geometries, reproducing configurations observed clinically [10],[60]. Mitral regurgitation jets were observed using the Toshiba color Doppler system in both annular configurations, with PM displacement (Figure 6.3 and Figure 6.4).
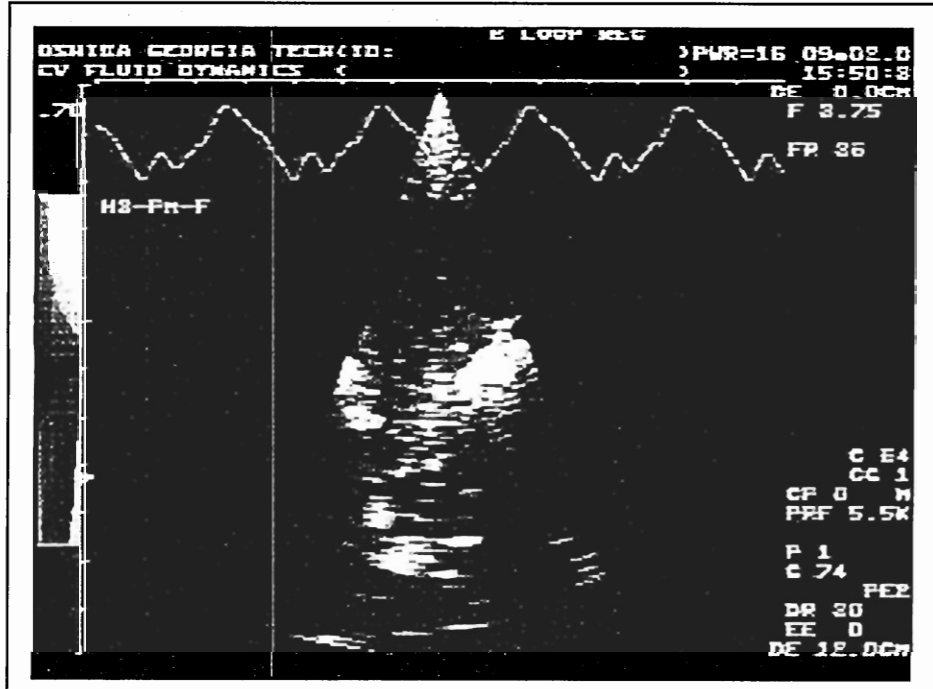
Figure 6.3. Color Doppler images of valve 3 in the flat annulus configuration. Regurgitation jets (red) are observed in the atrium as they flow through the valve.
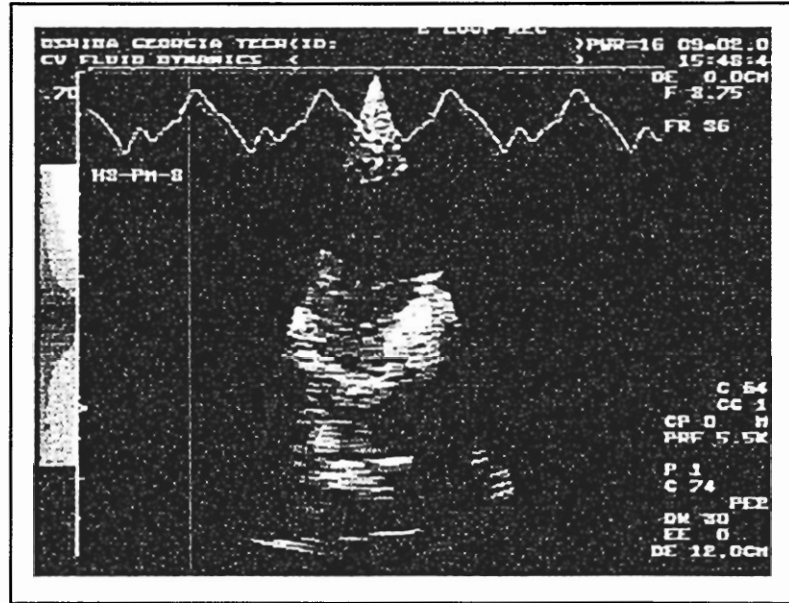
Figure 6.4. Color Doppler images of valve 3 in the flat annulus configuration. Regurgitation jets (red) are observed in the atrium as they flow through the valve.
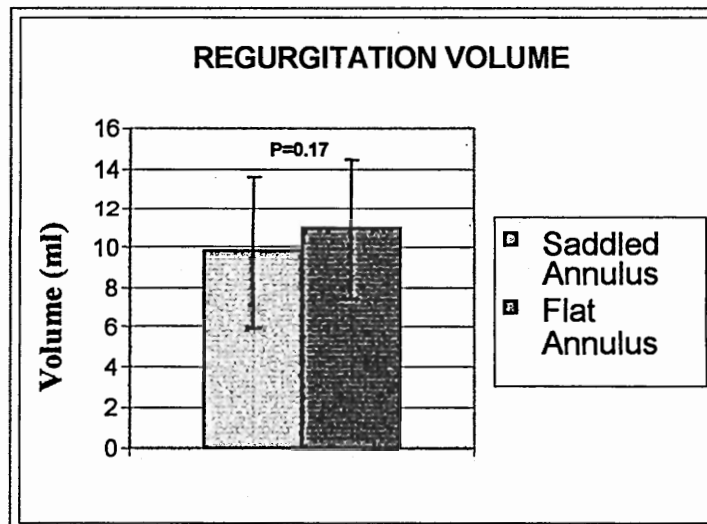
Figure 6.5. Regurgitation volumes for the flat and saddled annulus configurations.

Mitral regurgitation volume was calculated by integrating the systolic section of the flow curve, which included both the closing and leakage volumes. Apical posterior lateral papillary muscle displacement was used to reproduce a severe pathological position. During apical posterior lateral PM displacement, the mean regurgitation volume was 9.8±3.8ml/beat for the saddle configuration and 10.9±3.5ml/beat for the flat configuration (Figure 6.5). No significant difference in mitral regurgitation between the saddle and flat annular configurations was observed (p=0.17, n=11).

6.3.2 Chordae Tendineae Tension

Six of the eleven valves were instrumented with C-rings for the chordal force distribution experiments in specific aim 1. Chordal tension was compared using the peak systolic tension (PST) values for individual chords. Of the six human valves tested with C-rings, data from the posterior marginal chord from valve 1 was discarded because of a strain gauge malfunction detected during the experiment and confirmed during the post-experiment C-ring calibration protocol. Table 6.1 presents a summary of chordae tendineae peak systolic tensions for specific aim 1. This table shows the average PST for the individual chords of the six valves, for both the flat and saddle annulus configurations. The p-values for the paired t-test statistical comparison of the forces on the individual chords, for the flat and saddle annulus configurations are also presented. When comparing the peak systolic tensions on the different chords, the secondary chords (anterior strut and posterior intermediate chords) bore the larger loads on each of their respective leaflets when compared to the primary chords (anterior marginal and posterior marginal chords).

Table 6.1. Summary of chordae tendineae peak systolic tension results and statistics for the flat and saddle annular configurations.

CHORD	NUMBER OF SPECIMENS	PEAK SYSTOLIC TENSION FLAT ANNULUS (Newtons)	PEAK SYSTOLIC TENSION SADDLED ANNULUS (Newtons)	PERCENTUAL DIFFERENCE (%)	STATISTICAL SIGNIFICANCE P-Value
Anterior Strut	6	1.22±0.52	0.95±0.35	18.5±16.1	0.018
Posterior Intemediate	5	0.25±0.14	0.30±0.18	-22.3±17.1	0.022
Posterior Marginal	4	0.03±0.04	0.06±0.05	-137.8±188.6	0.12
Basal posterior	6	0.19±0.10	0.31±0.25	48.5±89.9	0.122
Anterior Marginal	6	0.31±0.17	0.35±0.16	-58.5±111.4	0.145
Commissural	5	0.17±0.18	0.11±0.20	59.0±32.3	0.008

The anterior strut chord had a tension 0.74±0.46 N higher than the anterior marginal chord. As a result, the load on the anterior strut was approximately three times the load observed on the anterior marginal chord. The load on the posterior intermediate chord was 0.18±0.16N higher that the load on the posterior marginal chord. The commissural chord had a tension considerably smaller than that of the secondary chords, but close to that associated with the posterior basal chord.

Differences when comparing the PST in the two different annular configurations in the normal PM position were measured as a percentage change using the flat annulus as a control. This eliminates to a certain extent the effects of the natural variation between individual valves. For all valves, the tension on the anterior strut chord was lower in the saddle configuration when compared to the flat configuration. The average difference of the force on this chord was 18.5±16.1%, which was statistically significant ($p<0.02$,n=6). The average difference in the posterior intermediate chord was 22.3±17.1%, with higher tensions being present in all the valves for the saddle configuration. This result was also statistically significant ($p<0.03$,n=5). Although all valves showed an increase in tension for the posterior marginal chord in the saddle configuration, this change was not statistically significant ($p=0.12$, n=4). Measurements on basal chords also showed an increase in tension in the saddle configuration for five valves. The average increase was 48.5±89.9%, although not statistically significant ($p=0.12$, n=6). In contrast, measurements on the commissural chord showed a decrease in tension in the saddle configuration for all valves. The average variation in force for this chord was 59.0±32.2% ($p<0.01$, n=5). For the anterior marginal chord, two valves showed a decrease in tension in the saddle configuration, while four valves presented an increase in tension. The

average increase in tension for the saddle configuration was 58.5±111.4%. However, this increase was not statistically significant (p=0.15, n=6).

When comparing the force distribution among the chordae tendineae, the flat annulus configuration showed a higher variability of tension between the different chords STDEV= ±0.47N, when compared to the saddle configuration STDEV= ±0.36N.

6.4 Results for Specific Aim 2: Effect of Annular Displacement
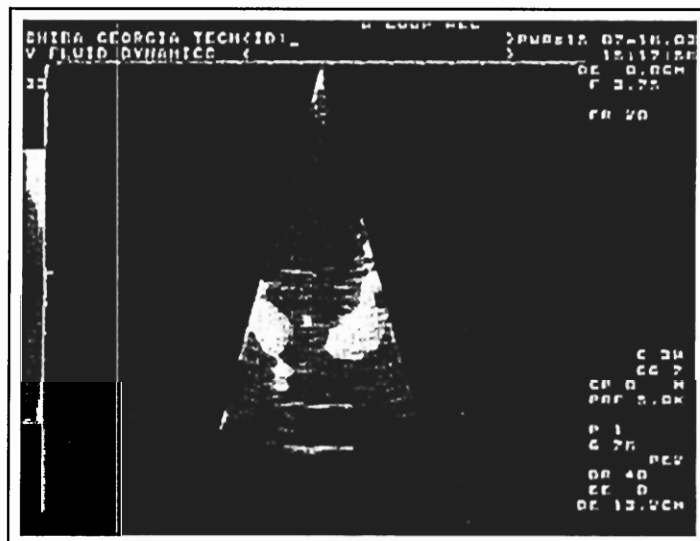
Figure 6.6. Doppler image of valve 3 in the normal papillary muscle position. The mitral valve is fully closed with no observable regurgitation jets (red). Flow from the reservoir into the atrium during filling is represented by blue areas.

Six human mitral valves were used in this set of experiments for specific aim 2. Experiments involving annular displacement used the flexible annulus model atrial chamber. Annular displacement was calculated from the video images of the base of the annulus, which showed membrane displacement (Figure 4.21). The average apico-basal

displacement of the annulus during the cardiac cycle was 3.8±0.6mm (normal PM position). In the displaced PM position (position 555), the average displacement of the annulus during the cardiac cycle was 2.6±0.6mm. The difference in annular displacement was statistically significant (p<0.02).

6.4.1 Valve Function

In the normal PM position, all valves closed well with no observable leakage in the Doppler images (Figure 6.6). The closing volume of the valves was calculated from the systolic area under the flow curves. The average closing volume of the valves for specific aim 2 was 3.4ml/beat larger than the closing volumes of the valves for specific aim 1 in the normal PM position. During, apical–lateral-posterior displacement of the papillary muscles, tented leaflet geometries were generated on the mitral valve, as
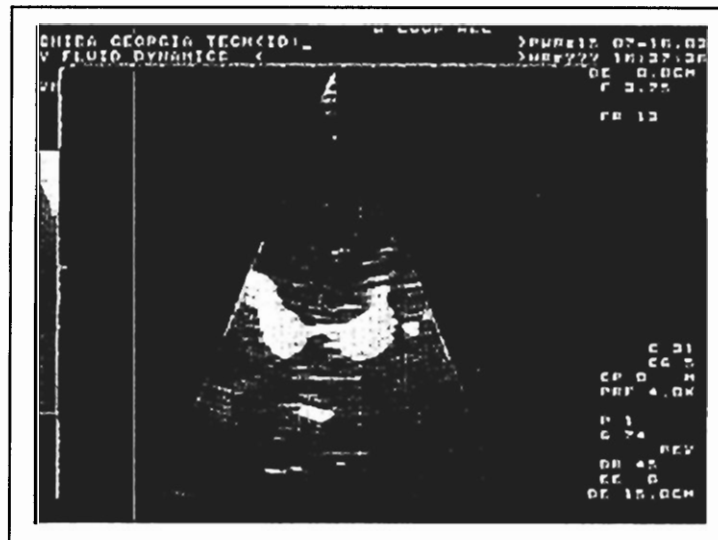
Figure 6.7. Doppler image of valve 3 subjected to papillary muscle displacement. The mitral valve is closed, but with observable regurgitation jets (red).

previously observed in specific aim 1. The coaptation abnormalities lead to regurgitation jets which were recorded in the color Doppler images of the valves during systole (Figure 6.7). Regurgitation volumes were calculated from the negative flow volume of the mitral flow curve.

The average regurgitation volume was 16.8 ± 1.5ml/beat. This volume was significantly higher than the volumes calculated in specific aim 1 for both the saddle and flat annulus configurations ($p < 0.05$). Average regurgitation volumes for the flat annulus, saddled annulus, and flexible annulus are presented in Figure 6.8.
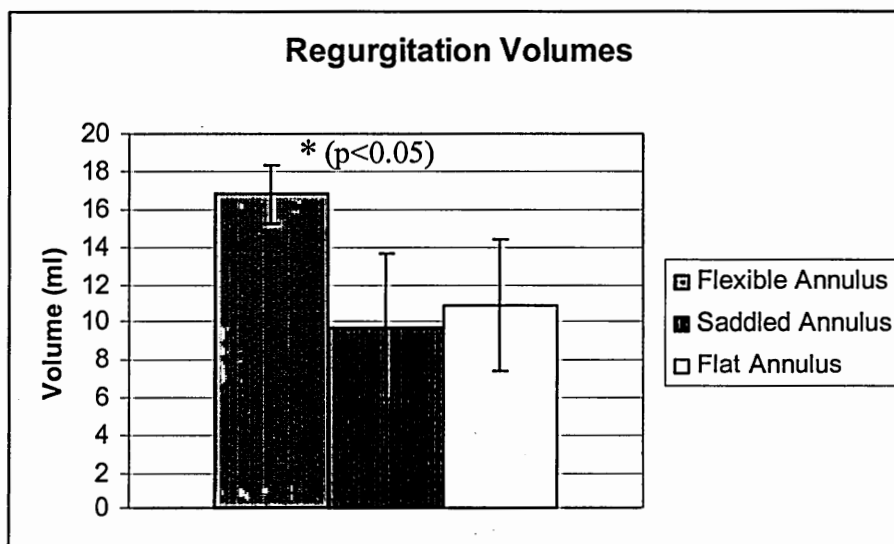
Figure 6.8. Average regurgitation volumes for the flat, saddled, and flexible annulus. The results show a significant increase in regurgitation volume for the flexible annulus.

6.4.2 Chordae Tendineae Tension

For specific aim 2, six chordae tendineae of six different human valves were instrumented with C-ring force transducers. Experiments were conducted for all valves in

81

the normal PM position. Chordae tendineae tension measurements of the posterior marginal chord from valve 2 and valve 6 were discarded because of strain gauge malfunction. The measurements for the anterior strut of valve 6, basal posterior chord valve 1, and the anterior marginal chord from valve 2 were also discarded because of C-ring malfunction. All other measurements were used and statistically analyzed.

The PST distribution among the marginal and strut chords followed the same trends which were observed in specific aim 1. The anterior strut chord had a PST of 1.11 ± 0.57N (n=5) while the anterior marginal (n=5) chord had a significantly (p=0.025) smaller load (PST= 0.18 ± 0.16N). On the posterior leaflet, the posterior intermediate chord (n=6) carried an average PST of 0.29 ± 0.14N, while the posterior marginal chord held a significantly (p=0.03) lesser PST of 0.08 ± 0.11N (n=4). The posterior basal and commissural chords held similar loads. The posterior basal chord had a PST of 0.48 ± 0.25N (n=5), while the commissural chord had a PST of 0.40 ± 0.31N (n=6). The difference in tension between them was not statistically significant (p=0.62).

Table 6.2. Average Peak systolic tension values for individual chords using the flexible annulus model.

Chord	Peak Systolic Tension Flexible Annulus (Newtons)
Anterior Strut	1.11±0.57
Anterior Marginal	0.18±0.16
Posterior Intermediate	0.29±0.14
Posterior Marginal	0.08±0.11
Basal Posterior	0.48±0.25
Commissural	0.40±0.31

A summary of the PST for the different chords using the flexible annulus model are presented in Table 6.2 and Figure 6.9.
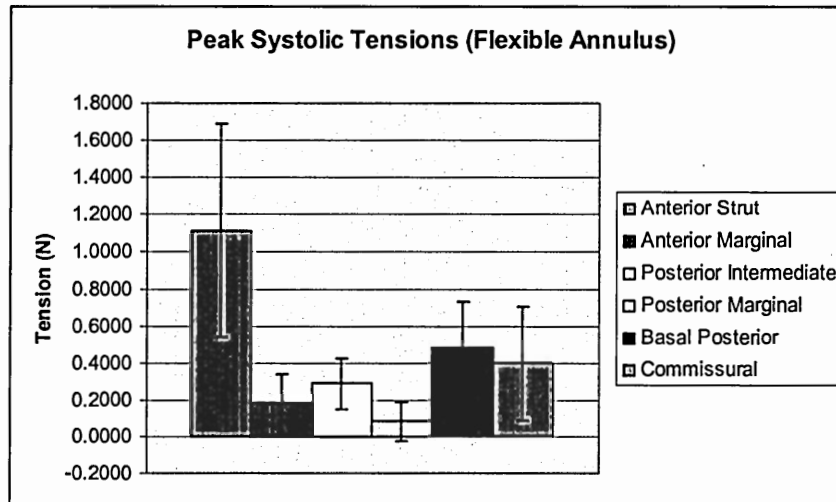
Figure 6.9. Graph of average peak systolic tension values for individual chords using the flexible annulus model.

Table 6.1 and Table 6.2 show the loads on the individual chords in specific aim 1 and specific aim 2. The results showed similar PST for most of the chords. Statistical comparison for the anterior strut chord and the posterior marginal chord, for the different annular configurations, showed no statistically significant difference ($p > 0.64$). The load for these two chords was relatively similar for all annular configurations. Although the results for the marginal chords for the different annulus configurations showed an apparently smaller average load using the flexible annulus model, this difference was not statistically significant because of the large standard deviations ($p > 0.1$). The basal posterior chord had a significantly larger load in the flexible annulus configuration ($p \leq 0.05$) when compared to the saddle annular configuration. This difference was not significant when comparing the flexible annulus to the flat annulus.

Table 6.3. Peak systolic tension results for the different types of chords on the flexible, flat, and saddled annuli.

Chord Type	Peak Systolic Tension Flexible Annulus (Newtons)	Peak Systolic Tension Flat Annulus (Newtons)	Peak Systolic Tension Saddled Annulus (Newtons)	Statiscical Significance Flexible- Flat (p-value)	Statiscical Significance Flexible- Saddled (p-value)
Maginal Chords	0.14±0.14	0.20±0.20	0.23±0.19	0.41	0.24
Intermediate Chords	0.66±0.57	0.78±0.63	0.65±0.44	0.66	0.97
Basal Chords	0.44±0.27	0.18±0.14	0.22±0.24	0.03	0.07

Even though, the commissural chord appeared to have larger loads in specific aim 2, this comparison was not statistically significant (p>0.1). As shown initial comparison of the individual chord for specific aims 1 and 2 showed only one statistically significant difference, therefore additional comparisons were conducted.

Further comparative analysis of the PST for specific aims 1 and 2 were conducted after dividing the six chords into three groups. The chords were grouped according to their location on the leaflet into marginal chords (anterior marginal chord and posterior marginal chord), intermediate chords (anterior strut chord and posterior intermediate chord), and basal (commissural chord and basal posterior chord). This chordal grouping and nomenclature is commonly used in literature and also address functional and structural conditions within the chords [38][39]. Table 6.3 presents the average PST for the different types of chords under the different annulus configurations.

The results of the comparison between the different types of chords for the different annuli, show very similar values for the intermediate chords (flexible annulus PST = 0.66±0.57N, flat annulus PST = 0.77±0.63N, saddled annulus PST = 0.65±0.44N). Therefore, the statistical comparison for the intermediate chords in the different annular configurations showed no significant difference (p<0.65). The marginal chords had peak systolic tensions of 0.14±0.14N for the flexible annulus, 0.20±0.20N for the flat annulus, and 0.23± 0.19N for the saddled annulus. The difference between these results was also not statistically significant (p> 0.2). In contrast, the basal chords showed significantly larger PST values in the flexible annular configuration (PST= 0.44±0.27N) when compared to the flat annular configuration (PST = 0.18±0.14N), and the saddle annular

configuration (PST = 0.22 ± 0.24N). The p-values for these comparisons were (p<0.02) and (P<0.07) respectively.

6.5 Results for Specific Aim 3: Effect of Papillary Muscle Position

Seven human and four porcine valves were studied using the left heart simulator with the standard atrial model for specific aim 3. Peak systolic tension measurements under 0.01N were discarded, as they could not be distinguished from electrical crosstalk. The C-rings were calibrated before and after each experiment to assess transducer functionality and linearity. Measurements for individual chords were discarded after each experiment if the transducer showed malfunction during post-experimental calibration. Data for positions 005 and 505 were not obtained for all valves because of geometrical restriction in the PM displacement apparatus. This restriction related to valves with unusually long chordae tendinea . Only these factors account for the reduced number of specimens in some data sets; no other criterion was used to discard measurements. All valves coapted well in the normal PM position. No chordal rupture was observed with any of the valves studied.

6.5.1 Peaks Systolic Tensions for Porcine and Human Mitral Valves

Peak systolic tension values of porcine and human MVs were compared for the normal PM position. A summary of the PST values for the two groups and their statistical comparison is shown in Table 6.4. As observed, there was no significant difference between the two groups for any of the six chordae tendineae.

Table 6.4. Average peak systolic chordae tendineae tension values for human and porcine mitral valves, and their statistical comparison in the normal papillary muscle position.

| Chord | Specimen | | T-test |
| | Porcine | Human | |
	PST (N)	PST (N)	p-value
Anterior Strut	1.02±0.61	1.16±0.57	0.74
Anterior Marginal	0.26±0.18	0.41±0.23	0.26
Porterior Intermediate	0.43±0.48	0.30±0.18	0.70
Posterior Marginal	0.29±0.30	0.25±0.25	0.89
Basal Posterior	0.21±0.27	0.22±0.14	0.92
Commissural	0.06±0.03	0.21±0.27	0.23

6.5.2 Variation in Peak Systolic Tension Due to Papillary Muscle Displacement

Variations in PST due to papillary muscle displacement utilize the normal papillary muscle position as reference unless otherwise stated. Paired t-tests were used to compare the values of PST for the different PM positions. A summary of the PST results is presented in Table 6.4.

6.5.2.1 Anterior Strut Chord

As observed in Figure 6.10 there was a slight decrease in PST when the PMs were moved posteriorly to position 005. The average PST for the anterior strut chord in this position was 0.61±0.47N; however, this variation was not statistically significant (p=0.18). When the PMs were moved to position 050 and position 055, PST for this chord did not change significantly from that measured in the normal position (PST=1.12±0.54N). In contrast, when the PMs were moved to position 500 (PST=1.42±0.78N), position 550 (PST=1.50±0.73N), and position 555 (PST=1.52±0.94N), there was a significant (p<0.05) increase in PST. Comparing position 505 (PST=0.93±0.87N) to position 500, there was a decrease in PST (p<0.1).

Figure 6.10. Average peak systolic tensions for the anterior strut chord in the different papillary muscle positions.
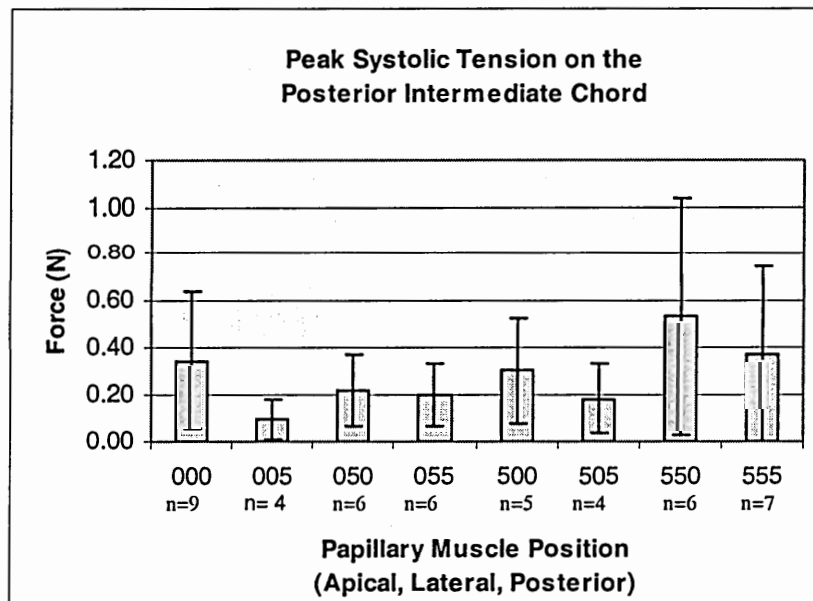
Figure 6.11. Average peak systolic tensions for the posterior intermediate chord in the different papillary muscle positions.

6.5.2.2 Posterior Intermediate Chord

The average PST on this chord in the normal PM position (PST=0.34±0.29N) had a slight decrease (p=0.14) associated with the posterior displacement of the PMs when going to position 005 (PST=0.09±0.08N) as observed in Figure 6.11. For positions 050 (PST= 0.21±0.15N) and position 055 (PST= 0.20±0.13N), there was no significant change in PST. For position 500 (PST 0.30±0.22N) there was a small but significant (p<0.05) decrease in chordal tension. The reduction in tension was emphasized (p<0.01) by the posterior displacement from the last location to position 505 (PST= 0.18±0.15N). On the contrary, the tension had a significant (p<0.02) increase for position 550 (PST= 0.53±0.51N). Position 555 showed a similar tension (PST= 0.37±0.36N) to the tension present in the normal PM position.

6.5.2.3 Anterior Marginal Chord

For the anterior marginal chord, there was no significant (p>0.1) difference in PST for position 005 (PST = 0.25±0.09N), position 500 (PST = 0.28±0.13N), position 505 (PST = 0.018±0.71N), and position 555 (PST= 0.27±0.19N) when compared to the tension present in the normal PM position (PST = 0.36±0.22N). For positions 050 (PST = 0.25±0.10N), position 055 (PST= 0.28±0.11N), and position 550 (PST = 0.22±0.13N), all associated with lateral displacement, there was a small but significant (p<0.08) reduction in tension as described in Figure 6.12.

89
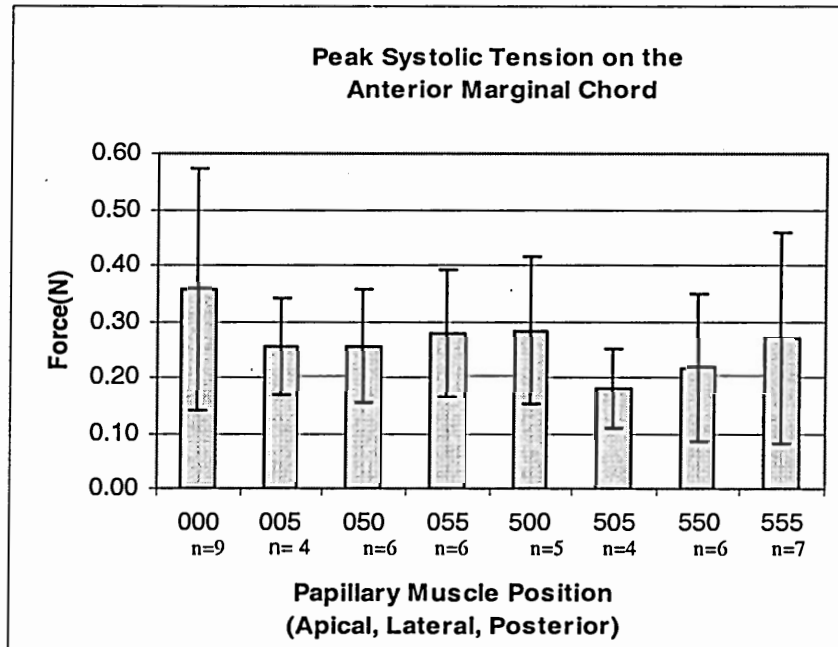
Figure 6.12. Average peak systolic tensions for the anterior marginal chord in the different papillary muscle positions.
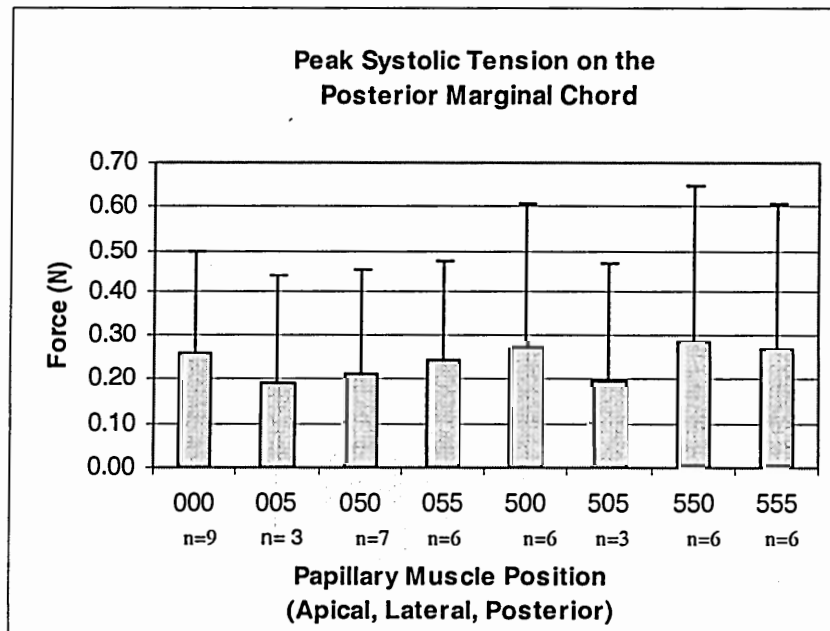
Figure 6.13. Average peak systolic tensions for the posterior marginal chord in the different papillary muscle positions.

6.5.2.4 Posterior Marginal Chord

As shown in Figure 6.13, the PST on the posterior marginal chord was relatively uniform for all positions. The variation in tension was only significant ($p<0.05$) for position 550 where there was a slight increase in tension (PST = 0.29 ± 0.36N) when compared to the normal position (PST= 0.26 ± 0.24N). A slight increase ($p=0.11$) was observed in position 500 (PST = 0.27 ± 0.34N) when compared to the normal position.

6.5.2.5 Basal Posterior Chord

The basal posterior chord was very sensitive to changes in PM position; there were six different positions with statistically significant variations. As observed in Figure 6.14, there were large variations in the mean values for PST. Position 005 (PST = 0.08 ± 0.04N) and position 050 (PST = 0.1 ± 0.06N) showed a decrease in tension ($p<0.1$) when compared to the normal PM position (PST = 0.21 ± 0.18N). Position 500 (PST = 0.29 ± 0.19N) and position 550 (PST = 0.38 ± 0.29N) showed relatively large and significant increases in tension ($p<0.05$), while position 505 (PST = 0.21 ± 0.07N) showed a small but significant ($p<0.05$) decrease in tension. When comparing position 500 with position 505, there was a decrease in tension associated with the posterior motion of the PMs.

6.5.2.6 Commissural Chord

The commissural chord showed high sensitivity to PM displacement as observed in Figure 6.15. Position 005 (PST = 0.04 ± 0.04N), position 050 (PST = 0.05 ± 0.04N),
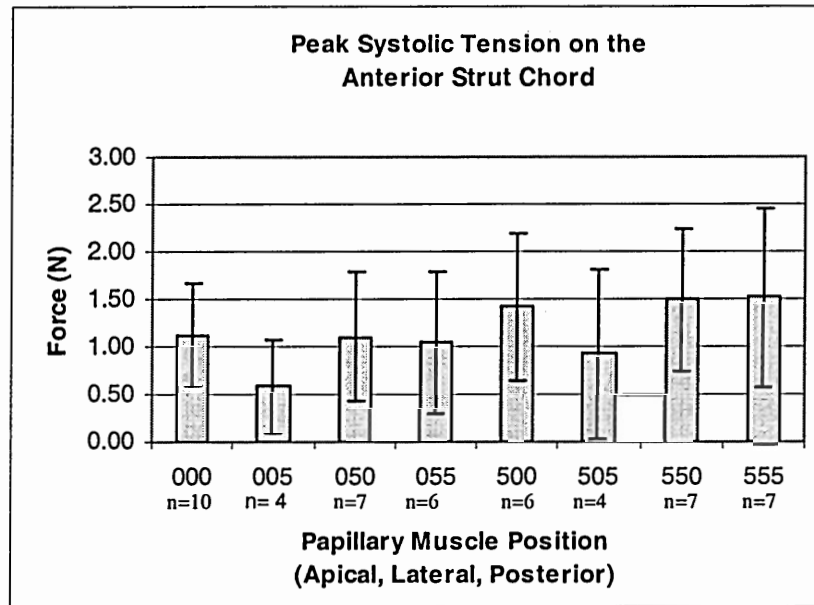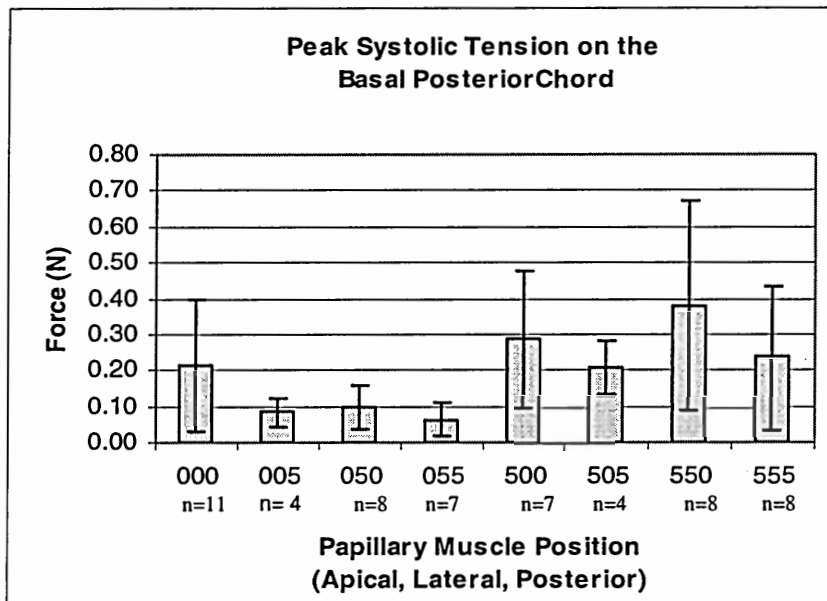
Figure 6.14. Average peak systolic tensions for the basal posterior chord in the different papillary muscle positions.
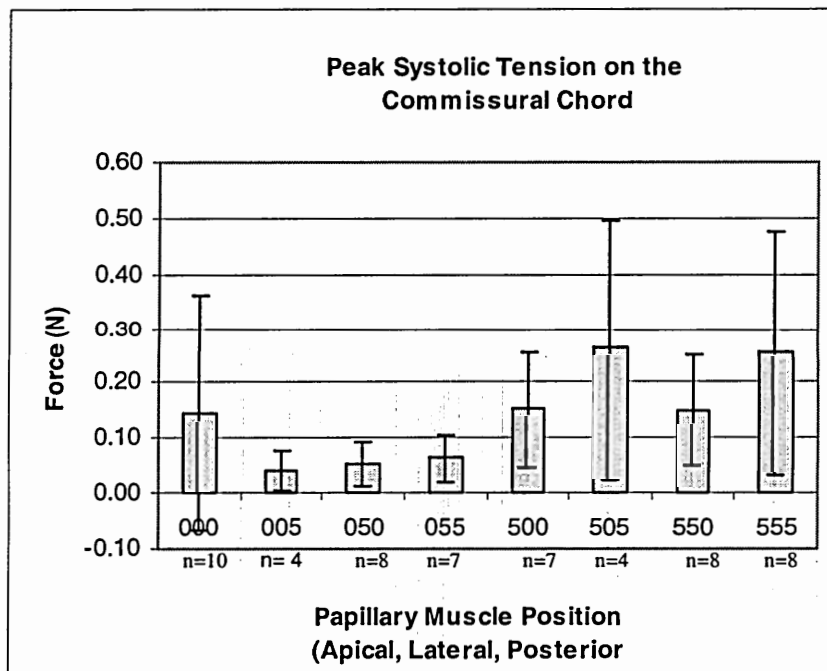
Figure 6.15. Average peak systolic tensions for the commissural chord in the different papillary muscle positions.

and position 055 (PST = $0.06\pm0.04N$) showed decreases in tension ($p<0.1$) when compared to the normal position (PST = $0.15\pm0.21N$). In contrast, position 500 (PST= $0.15\pm0.10N$) and position 550 (PST $0.15\pm0.10N$) showed small but statistically significant increases in force ($p<0.05$). Position 505 (PST= $0.26\pm0.24N$) and position 555 (PST = $0.25\pm0.22N$) showed large but statistically insignificant increases in force because of the large standard deviations in the measurements.

When comparing PST for the different PM positions for each individual chord, the results showed the smallest percentage standard deviation in PST for the posterior marginal chord ($\pm 15\%$). This may be observed in Figure 6.13 were all bars tend to be relatively uniform. The anterior marginal chord also showed relatively small variations from the average PST for all positions ($\pm20\%$). The anterior strut had a variation in PST of $\pm27\%$ and the posterior intermediate chord had a variation in PST of $\pm 49\%$. The largest variations in PST between PM positions are present in the basal posterior chord ($\pm56\%$) and in the commissural chord ($\pm61\%$) as observed in Figures 6.14 and 6.15.

CHAPTER VII

DISCUSSION

7.1 General Observations

The importance of this *in vitro* study lies in the analysis of the effects of isolated variables on mitral valve function and chordal force distribution. Identifying how annulus dynamics and papillary muscle position affects the mitral valve (MV), will provide further understanding about valve function under both normal and pathological conditions. In general, the results of this study show how the structure of the mitral valve allows it to work in a complex mechanical environment by isolating valve closure from the changes that may occur around it.

The regurgitation volumes measured in both specific aims 1 and 2 are clinically small, representing a range of regurgitation fractions of 14% to 22%. These are small considering the large PM displacements used under the pathological conditions. Generally under pathological conditions, several alterations occur simultaneously (annular dilation, papillary muscle dis-coordination, ventricular malfunction, etc.); therefore, varying a single variable within the valve, as in this study, may lead to lesser regurgitation volumes. In parallel, symmetric displacements of the PMs have been shown to cause less regurgitation than asymmetrical displacements [44]. Therefore, the strict control in the symmetrical displacement may have also lead to smaller regurgitation volumes.

94

Papillary vectorial dislocation of 5mm may appear to be large. However, losses of PM contractility in the order of 2-3mm have been observed in humans with cardiomyopathy [6], and increases of end systolic LV endocardial radius of 5mm have been observed in ovine dilated cardiomyopathy models [7]. Therefore, coupling displacements due to loss of PM contraction, ventricular dilation, ventricular remodeling, and the larger size of the human heart when compared to sheep models, PM dislocations of 5mm are within pathological range for humans.

Considering that the annular models are designed to emulate conditions during systole, and that the main function of the chords is to prevent leaflet prolapse. This study focused on the variation in tension that occurs during systole and assumed that the chords were buckled or had non-significant tension during diastole. Therefore, diastolic tension was considered as baseline. Previous experiments showed that chordal tension is flow rate independent; linearly dependent on pressure [67]; and peak systolic tension values depend on the pressure gradient across the valve and valve geometry. Furthermore, the trans-mitral curve also reaches a plateau during most of systole. Therefore, peak systolic tension was selected as the descriptive parameter of chordal force distribution during systole. In addition, the only previous *in vivo* study [11] only presented data on peak systolic tension. Therefore, comparison of this parameter between this in vitro model and in vivo experiments provided validation of the results.

The tension for the primary (marginal) and secondary (intermediate) chords in the defined normal conditions was within ranges observed previously *in vivo* in animal studies. For the secondary (intermediate) chord, the *in vivo* porcine model had an average peak systolic tension (PST) of 0.7N[11]. The results for the present study showed forces of

0.66±0.57N for the flexible annulus, 0.78±0.63N for the flat annulus, and 0.65±0.43N for the saddle shaped annulus. For the marginal chords, the *in vivo* model provided an average force of 0.2N[11]. The results of the present study showed forces of 0.14±0.14N for the flexible annulus, 0.20±0.20N for the flat annulus, and 0.23±0.19N for the saddled annulus. Therefore, peak loads were within physiological ranges for these chords. There are no known data on chordal tension for the basal chords.

7.2 Specific Aim 1

7.2.1 Mitral Annulus Shape

The results of the anatomical measurements describe an increase in length of the basal chords from the commissural to the anterior and posterior segments of the annulus, which are larger than those determined by pythagorean relations. When the chordae tendineae are extended and the annulus is relatively free to deform, the mitral annulus generates a saddle shaped configuration. Chordae tendineae lengths are approximately constant during the cardiac cycle, and there is a higher density of basal chords inserting into the commissural section of the annulus. As a consequence, when under systolic pressure, the mitral valve is pushed backwards. The free posterior and anterior sections of the annulus deflect into the atrium, while the commissural sections are held relatively in place by the PMs and corresponding chords. Annular flexing/bending and anatomical relations may partially explain the saddle shape of the annulus, but the shape of the mitral annulus is not a simple symmetric elliptical saddle, but a complex asymmetrical saddle structure. Other phenomenon such as myocardial contraction, aortic expansion, PM contraction,

and ventricular motion may affect the shape of the annulus [23], [29]. Therefore, the complex inter-relation between these mechanisms warrants further investigation.

7.2.2 Valve Function

Geometrical variations in mitral annular shape have been observed in patients with pathologies such as functional mitral regurgitation [3], hypertrophic obstructive and dilated cardiomyopathy [5], and models of ischemic mitral regurgitation [3][61]. Loss of saddle curvature has been described as a possible cause for mitral regurgitation in animal and human studies [3][61]. Patients with FMR showed loss of curvature in the saddled annulus, which subsequently may increase annular area because of reduced flexing. *In-vitro* studies have shown that only increases in projected area over a factor of 1.75 will induce mitral regurgitation without PM displacement [18]. Therefore, area changes associated with a loss of curvature are not sufficient to induce regurgitation. The loss in curvature in FMR patients may be related to changes in ventricular and PM dynamics since loss of annular displacement, curvature, and dynamical change have also been observed in regurgitation associated pathologies [3] [4] [30]. Therefore, loss of annular curvature and regurgitation may not hold a cause consequence relationship, but both may have similar origins. This may explain why variation of annular shape alone (flat- saddle) did not induce mitral regurgitation as represented by the results of this study. A possible explanation of the reduction in saddle height in patients with cardiomyopathy and ischemic heart disease is that in both of these pathologies there is to some extent a loss of ventricular muscular function. This loss has several consequences, one of which is a loss in the sphincteric capabilities of the muscles around the annulus. Kaplan et. al. 2000

showed that pathologies such as ischemic heart disease and cardiomyopathies do not only affect the annulus by dilation, but they also reduce its capability to contract [3]. Kaplan and colleagues also showed that variations in 2D perimeter are larger than variations in 3D perimeter during annulus contraction [3]; therefore, a large component of the reduction in annulus area is flexure. The saddle shape of the annulus is preserved during the cardiac cycle, but its height and curvature are enhanced by several factors including the sphincteric contraction of the annulus.

Saddle curvature is increased because of annular contraction

The saddle is the natural shape of the mitral valve because of relations in chordal length
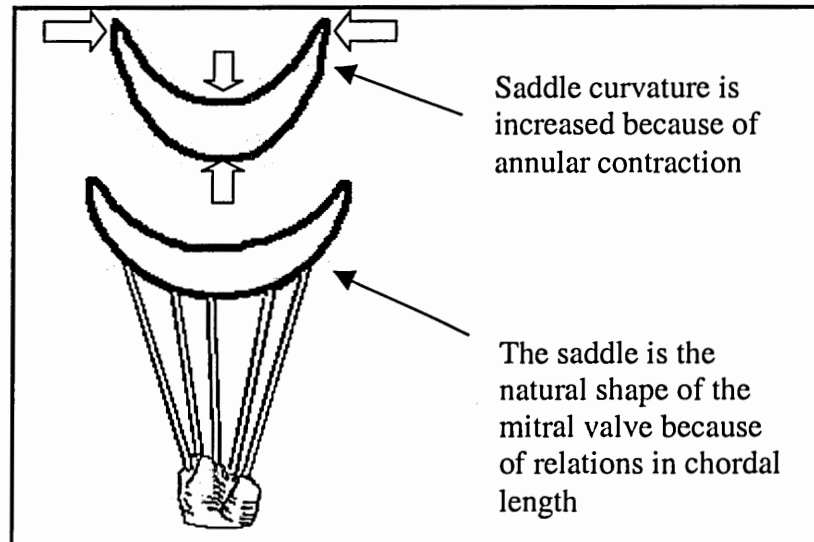
Figure 7.1. Diagram explaining increased saddle curvature during the cardiac cycle.

As represented in Figure 7.1, if there is a loss in annular contraction, the final saddle height of the annulus is reduced. Therefore, losses in ventricular function associated with the described pathologies may explain the reduction in saddle height observed in these patients.

7.2.3 Chordae Tendineae Force Distribution
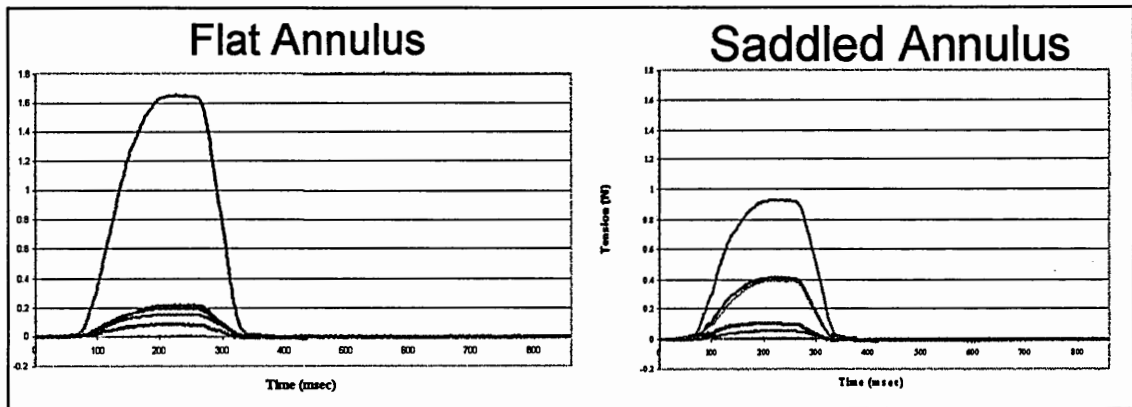
Figure 7.2. Comparative diagrams of force distribution in the flat and saddle annular configurations for valve 2.

The results showed for both configurations, force distributions characterized by the secondary chords carrying most of the load on their respective leaflets. This phenomenon has been observed and analyzed by other researchers [11] [38] [43]. The saddle configuration showed a more evenly distributed force as illustrated by the variance of the tensions on the different chords. This phenomenon may also be observed in Figure 7.2 where the tension curves for the different chords are closer for the saddle configuration. Therefore, the saddle configuration optimizes the force distribution on the valve since a larger number of chords are extended and the load is divided more evenly among them.

The forces on the MV and its apparatus are determined by several factors: valve geometry, leaflet area, trans-mitral pressure, and contact forces along the coaptation line. In parallel, leaflet curvature has been shown to be important in valve mechanics, as

billowing (primary curvature) and saddle curvature (secondary curvature) may reduce stress on the leaflets [19] [35].
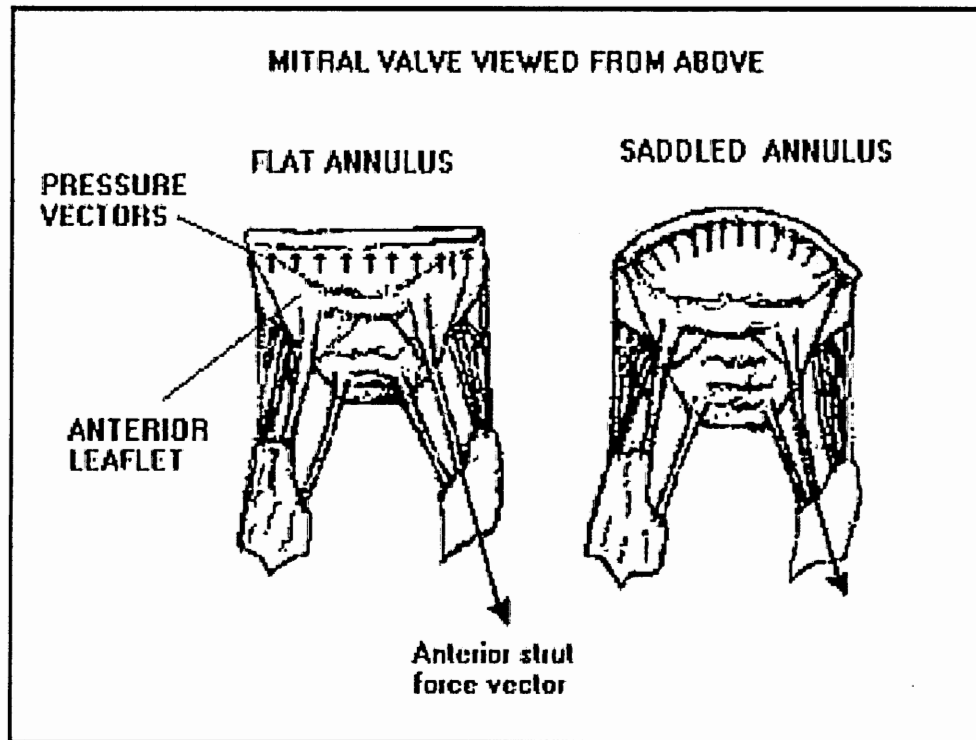
Figure 7.3. Pressure vectors acting on the mitral valve anterior leaflet in a flat and saddled configuration. Pressure vectors are redirected towards the sides of the valve in the saddle configuration decreasing the resultant force in the direction of the anterior strut.

The reduction in force for the anterior strut chord may be explained by a redistribution of the force vectors caused by pressure because of the secondary curvature generated by the saddle (Figure 7.3). Since pressure acts perpendicularly to the surface, due to the secondary curvature of the saddle more force vectors are directed towards the commissural direction and less in the apical direction. The anterior strut chord is directed

mostly in the apical direction implying that its tension will be reduced if the apical force component generated by pressure decreases. Chords extending in other directions must then balance the new by redirected components of the force. These redirected vectors may explain the increase in force on the other chords.

The peak systolic tension of the anterior marginal chord did not vary significantly, and this variation followed different trends for different valves. The peak systolic tension values for the posterior marginal chord were small and near the limit of the C-ring crosstalk range; all the values above the crosstalk threshold followed the same trend of increased force. This variability may be explained by the fact that marginal chords insert on the outer edge of the leaflet implying that tension on this chord is predominantly determined by trans-mitral pressure, contact forces, and coaptation line geometry and location. Leaflet curvature may have a lesser effect on the marginal chords than on the secondary chords.

During coaptation, the posterior leaflet central scallop is extended for the most part and it is smaller than the anterior leaflet. Therefore, the effects of force redistribution are probably less than those seen on the anterior leaflet. Meanwhile, the relative distance from the PMs to the anterior and posterior segments of the annulus is increased by the saddle geometry. This increase in length, coupled with the decreased effect of the saddle curvature may explain the increased tension on the posterior intermediate chord.

The basal posterior chord inserts directly above the posterior section of the annulus. The increased distance between the PMs and the annulus may account for the increased tension on this particular chord in the saddle configuration.

101

7.3. Specific Aim 2

7.3.1 Annular Displacement

Although during preliminary studies the membrane on the flexible model showed displacements in the physiological range (8mm with a free membrane), the actual displacement during the experiments was 3.8±0.6mm on average, therefore, approximately 4mm smaller than those observed clinically in patients[5]. In humans the left ventricle contracts helically towards the atrium, thus moving the base of the papillary muscle towards the annulus. In addition, the annulus also moves upwards into the atrium [4]. Since research has shown that the distance between the tips of the papillary muscles and the respective commissural sections of the annulus is relatively constant[55], the difference between annulus displacement and ventricular displacement is compensated by PM contraction. Therefore, in the heart, the mitral apparatus as a whole undergoes translation towards the atrium during systole. In the *in vitro* model used in this study, there was no ventricular displacement or PM contraction. Therefore, the annulus displacement observed is a product of elongation in the PMs and extension of the chordae tendineae since the rest of the system is rigid. Hence, the reduced motion of the membrane during experiments was a direct result of motion restriction due to the stiffness of the basal chord, and the limitations of the model.

When the papillary muscles were displaced, the motion of the membrane was reduced to 2.6±0.6mm. The reduction of annulus displacement within the model is explained by the redirection of the basal chords. The motion of the membrane is limited by the stiffness of

the basal chordae tendineae. Therefore, when the PMs are displaced laterally or posteriorly, the basal-apical component of the elongation in these chords (which limits annular motion), is reduced as the chords now extend more laterally and posteriorly, therefore, less in the apico-basal direction.

Although other variables such as ventricular function and papillary muscle contractility are present in the human heart, reduced annular displacements in pathologies such as cardiomyopathy and ischemic heart disease [4] may be partially explained by the motion of the papillary muscles. This phenomenon was observed in this study. Although in the heart, as previously explained, there is an overall translation of the valve in space, the length of the commissural chord is constant. Therefore, lateral displacement should decrease annulus displacement. Considering that in these pathologies, the ventricle may be dilated with a reduction in contractility and torsion of the wall [7], ventricular dysfunction may also explain the reduction in PM contractility in dilated cardiomyopathy. Reduced repositioning of the ventricle with respect to the annulus would warrant less PM contraction to maintain the tension on the commissural chords.

7.3.2 Valve Function

Although Doppler images showed no leakage jets in the normal position, the closing volume of the valves in specific aim 2 had on average 3.4ml/beat higher closing volumes than those observed in specific aim 1. This discrepancy is a consequence of differences between the annular models. In the flexible annular model, there is a volume displaced by the closed valve when the annulus moves towards the atrium. The area behind the annulus (silicone tube 7.07cm^2), with an average annulus displacement of 3.8mm will

account for an approximate volume of 2.7ml/beat. Therefore, the difference in closing volumes between valves in specific aim 1 and 2 is an artifact of the flexible annulus model. This artifact will also affect the comparison between the results of mitral regurgitation (with papillary muscle displacement) for specific aims 1 and 2.

After correcting the regurgitation volumes due to PM displacement by 2.7ml, the average regurgitation volume with the flexible annulus model was 14.1 ± 1.5ml (before correction 16.8 ± 1.5ml/beat). This correction reduced the difference with the volumes observed in specific aim 1(Saddle 9.8 ± 3.8ml/beat, Flat 10.9 ± 3.5ml/beat); however, there still was small but significant ($p < 0.05$) increase associated with the flexible annulus. Previous research in an ovine model has shown that PM dislocations on the order of 1mm to 2.5mm may induce significant regurgitation [8]. In the static models, larger dislocations on the order of 5mm produced relatively small regurgitation volumes, but this volume was increased with a dynamic annulus. Therefore, the mitral valve is probably more sensitive to alterations within a dynamically complex environment as in the heart.

7.3.3 Chordae Tendineae Force Distribution

The experiments with the dynamic annulus showed significantly larger tension on the strut chords than on the marginal chords of their respective leaflets. The marginal chords carried the smallest loads. The commissural and posterior basal chords carried intermediate loads. This distribution was similar to the distributions obtained using the static models (specific aim 1).

Initial comparison between the individual chords, for specific aim 1 and 2, only led to a significant difference in loads for the basal posterior chord. The commissural chord

showed apparent differences between the static and flexible models, but the limited number of samples lead to a low statistical significance. To improve the statistical results and observe differences in tension between the different type of chords; the chords were grouped as marginal, intermediate and basal. This grouping describes differences in insertion location, function, and structural characteristics [39].

Comparison of PST between the static (specific aim 1) and the flexible annulus configurations (Figure 6.3) showed no significant differences in loads for the intermediate and marginal chords. Loads were very similar for the intermediate chords for the different annuli. The marginal chords showed a larger but not significant difference. This difference is probably related to the variability in the specimens and limitations of the C-rings. The basal chords (commissural and posterior basal) did show a significant increase in PST for the flexible annulus configuration. This increase in tension is specifically associated with the function of these chords. The basal chords insert near the annulus, and function to maintain a relatively constant distance between the annulus and the papillary muscles. In the static model, this distance was fixed which explains the relatively small peak tensions. If they inserted directly into the annulus no apparent increase in tension would be observed in the static models; but since they insert just above the annulus there was some tension increase during systole. In the flexible annulus model these chords are responsible for limiting the movement of the membrane and therefore maintaining valve integrity. Therefore in the flexible annulus model, a larger force is observed which is directly proportional to the area of the membrane and the pressure in the ventricle. In the heart, the area surrounding the annulus (relatively parallel to the annulus plane) upon which the pressure acts is smaller than that of the membrane.

Therefore, the absolute tension in these chords may be lower than that presented in the results of this study. Also, the papillary muscles are directly responsible for the control of the distance between the annulus and the ventricular wall, and therefore control the tension in these chords. It is difficult to assess the physiological accuracy of the tensions measured in this study for the basal chords as there are no *in vivo* data on the tension of the basal chords and the effects of papillary muscle regulation. Although the magnitude in force may not be confirmed, the function of these chords is well described by this study. In addition, the relative insensitivity of the marginal and intermediate chords to annulus motion, describes how these chordae tendineae which control leaflet motion (intermediate and marginal) are isolated from their surroundings. This characteristic enables the mitral valve to function in the heart independent of its moving and variable environment within the functional range of the basal chords.

7.4 Specific aim 3

7.4.1 Inter- Species Variability

The results of this study show no significant difference in chordal force distribution for porcine and human valves. Porcine and human mitral valves have been shown to be similar in chordal lengths, and chordal distribution patterns show only slight differences [40]. However, further research on this subject is warranted because of the large standard deviations and the limited sample size.

7.4.2. Effects of Papillary Muscle Displacement of Chordal Force

During the cardiac cycle, the valve is in a very dynamic environment described by annulus displacement, ventricular motion, and PM contraction. Within this environment, the basal chords try to maintain a constant distance from the tips of the PMs to the annulus, aiming to maintain overall valve geometry and isolate the motion of the leaflets from ventricular and annular motion. As the leaflets must maintain appropriate coaptation in the complex environment, the geometrical and anatomical construct of the valve must ensure that the chords controlling coaptation, are less sensitive to the changing environment around them. Therefore, as expected, the intermediate chords are less sensitive to changes in PM position than the basal chords; while the marginal chords are the least sensitive of all chordal types to PM position variations. These characteristics are clearly shown in the graphs of the average forces for the different positions presented in the results section for specific aim 3. These results again show how nature uses a functionally optimal design with flexibility and redundancy to maintain appropriate function under complex conditions.

Posterior displacement of the PMs shifts the coaptation line downwards, increasing the area of the mitral orifice covered by the anterior leaflet, and therefore, increasing its resultant force. Consequently, the apparent decrease in PST when going from position 000 to position 005 and from position 500 to position 505 is probably not significant, especially since all the valves studied did not follow the same trend. Another experimental factor that may explain this phenomenon, is that position 005 and position 505 were the last to be tested. At the end of each experiment, there was some observable plastic deformation in the chords. This deformation may decrease the observable force in

these last two positions. Apical displacement, as expected, did significantly increase the tension present in the anterior strut chord.

Posterior PM displacement appeared to decrease the tension in the posterior intermediate chord. Posterior motion of the PMs shifts the coaptation line posteriorly reducing the area of the orifice covered by the posterior leaflet, and decreases the insertion angle of this chord. Both of these alterations may reduce the resultant tension vector. The decrease in tension associated with position 500 may not appear reasonable at first glance, but may be explained by the insertion pattern of the posterior leaflet. Between the insertion location of the posterior intermediate chord and the posterior annulus, several more chords insert. When the PMs are displaced apically, the chords nearer to the annulus are pulled forward, displacing this segment of the leaflet. This forward motion may therefore decrease PST on the posterior intermediate chord. Combined apical-lateral displacement induced a significant increase in tension due to the stretching and redirection of the posterior intermediate chord. This effect was reduced in position 555 because of the posterior motion associated with this position.

As observed in Figure 6.12, the force on the anterior marginal chord is relatively homogeneous for the different positions. Although the results appear to show a decrease in tension for all positions, paired statistical analysis showed significance in position 050, position 055, and position 550 which are all associated with lateral displacement. The mitral valve has several marginal chords on the anterior leaflet with significant branching; therefore, load from the laterally displaced chords may be absorbed by others. Marginal chord tension depends on several factors such as contact forces and coaptation line geometry. As these characteristics have a high degree of variability and the detailed

108

features of leaflet tip coaptation are difficult to observe, the behavior of these chords is difficult to assess. Therefore, more experiments should be conducted to eliminate the effects of variability and to obtain more statistically significant results.

As observed in Figure 6.13, the behavior of the posterior marginal chord was similar to that of the anterior marginal chord in the relative homogeneity of tension for all positions. In general, the tension measurements for this chord were small in magnitude and highly variable from valve to valve. Detailed conclusions are difficult to asses because of limitations similar to those presented for the anterior marginal chord.

The tension on the commissural and basal posterior chords was highly sensitive to PM displacement. Because of the rigid nature of the model used in this study, any motion of the PMs will affect their distance to the annulus, as both of these positions are fixed during the cardiac cycle. Both the commissural and basal posterior chords insert on the leaflet just above the annulus. Therefore, they are subject to tension changes due to systolic pressure as they hold a small section of leaflet. If they inserted directly in the annulus there would not be a change in tension during systole, as the distance between the PMs and the annulus is fixed in the static annulus model used for specific aim 3. Posterior displacement reduced the tension on the basal posterior chord as it redirects its insertion angle, reducing the septal lateral component of force. Since the apical component should be constant as it is dependent on pressure, the overall resultant tension should decrease. As previously explained, apical displacement shifts the posterior leaflet and causes a reduction in tension on the posterior intermediate chords. Therefore, the basal posterior chords are subject to increased tension to compensate for the decrease in load on the posterior intermediate chord under apical displacement. Lateral displacement

109

had a conflicting trend between valves as well as positions for the basal posterior chord. When going from position 000 to position 050, there was an apparent decrease in force, but from position 500 to position 550 there was an apparent increase. Therefore, the effects of lateral displacement on this chord are not clear and the results may represent changes not associated with simple geometric variations, but may be related to complex chordal interactions.

The commissural chord selected for these experiments inserted near the annulus and below the septal-lateral midpoint of the valve (posterior section of the valve). Therefore, trends in force variation due to PM displacement are similar to those present in the basal posterior chord. Although apical motions clearly show the same trend of increase in tension in this chord, the more lateral and less posterior insertion results in a different trend when dealing with the effects of lateral and posterior displacement of the PMs.

7.5 Clinical Relevance

The clinical relevance of this study lies both in the cardiac implant field as well as in the surgical field. Annulus shape does not significantly improve valve closure. Therefore, reconstructive surgeries should not be as concerned with the reshaping of the annulus, but should try to resize it when dilated and maintain its flexibility. Loss of saddle curvature is a consequence of underlying ventricular abnormalities. Thus, surgical corrections must restore ventricular function and shape, which will in turn restore to some extend annular dynamics. A ventricular reconstruction procedure, which apparently restores ventricular torsion and dimensions, is under clinical trials [62]. These types of procedures are

110

necessary not only to restore ventricular function but also to restore mitral valve function. Considering the results, which clearly show that the shape of the annulus alters the force distribution among the chords, implants such as annuloplasty rings must take into account the effect of their implantation on chordal force distribution. Increased tension on the chords under cyclic loading implies under engineering standards a lower life expectancy for the chords because of possible tissue damage. On the other hand, reduction in force may increase the life expectancy of the chord, but if severe, this reduction may induce negative effects on valve function. As annular shape varies from valve to valve, annuloplasty rings should deform easily to maintain the physiologic loading on individual chords.

As shown by the results of this study, the loss of annulus displacement does not induce mitral regurgitation, but is a secondary effect because of disruptions in the underlying ventricular and papillary muscle function. Therefore, PM relocation procedures may correct mitral regurgitation in pathologies were ventricular topological changes are observed and at the same time may restore annular motion. Actually, the motion of the annulus may increase the closing volume of the valve. This increase is small and therefore is not an important factor in cardiac output. However, annulus motion does increase the mitral valve's sensitivity to PM dislocations. Therefore, implants which reduce mitral valve motion may not have a negative effect on valve closure. Implants which maintain the general geometrical relation between the annulus and PMs may significantly reduce mitral regurgitation even if they lessen some of its dynamics.

As described in the introduction, several pathologies associated with PM malfunction and ventricular remodeling may displace the PMs during systole, changing the coaptation characteristics of the valve. Previous research has shown that PM displacement is an important factor in mitral regurgitation [18] [44]. The effects of PM displacement are transmitted to the leaflets through the chords. Therefore, physicians have proposed surgeries such as chordal cutting or translocation as a solution to different types of regurgitation. For the most part, surgeons have observed that cutting the primary (marginal chords) induces severe regurgitation, but that in some pathologies cutting the secondary (intermediate chords) may decrease leaflet tenting leading to better coaptation and decreasing regurgitation [10]. Some surgeons are reluctant to use these procedures because cutting the large secondary chords may induce significantly higher loads on other chords that may eventually fail due to structural deterioration. As shown by the results, the secondary chords do carry the highest loads and therefore are structurally relevant to mitral valve function, and possibly ventricular function. Therefore, the increased load generated by cutting these chords warrants further detailed/fundamental studies, both *in vitro* and *in vivo*.

This study also provides important information, which may be used to assess the feasibility of chordal translocation procedures. The results show how different types of chords (marginal, intermediate, and basal) are subject to different degrees of loading. Previous research has shown that marginal, intermediate, and basal chords have different microstructures, which translate to differences in mechanical properties [39]. Therefore, chords that are translocated to repair a damaged valve, should probably be of the same type as the chord they will replace. Also since chordal types are designed for bearing

different loads, a translocated chord, if not of the appropriate type, may rupture under its new loading conditions completely obliterating the objective of the surgery.

In general, changes in mitral annular shape and displacement evaluated in this thesis may be linked for the most part to topological changes in the ventricle, although other factors such as loss of PM contractility are also significant. Therefore, further research towards the development of new surgical procedures or design of implants, which correct alterations in ventricular function and geometry are warranted.

7.6 Limitations

There are several limitations associated with both the apparatus and the methodologies used in this thesis. An initial limitation of this study was the limited population of human MVs. Unfortunately; this is the situation involving any study that utilizes human organs/tissues. To increase the number of specimens, porcine mitral valves were used. Porcine mitral valves have been shown to have similar anatomy and function to human mitral valves, to the extent that they have been used as grafts in replacement procedures. Papillary muscle insertion patterns and chordal characteristics varies severely among humans, mitral valves have been classified in four different groups according to the complexity of their PM characteristics. Type I PM mitral valves have the simpler PM insertion pattern while type IV valves have the most complex PM insertion pattern. Only human mitral valves with simple insertion patterns were used in this study, as they may be easily adapted to the left heart simulator. Also, the porcine PM insertion pattern is

quite simple. Thus, porcine valves can be better compared to human valves with simple insertion patterns (Figure 2.6). Even though the same six chordae tendineae were carefully selected for C-ring implantation, their size and ramification varied from valve to valve. MV leaflet size and coaptation geometry also varied from valve to valve. Coaptation line location and geometry also varied from valve to valve although a standard normal position was used. Because of this natural variability and the reduced population, the standard deviations for the results were high.

The left ventricle heart simulator has several limitations, but it has successfully been used in several pioneering studies [18] [42] [59]. Although the pressure and flow conditions generated in this loop are physiological, it does not reproduce phenomenon such as ventricular, atrial, or papillary muscle contractions as it is a rigid model. Therefore, tension measurements, in particular on the basal chords, may have different magnitudes compared to those presented in this study. The lack of ventricular motion is of particular importance because it has been shown to be directly related to several pathological conditions that affect the mitral valve.

Measurement of tensions using the C-ring transducers had some technical limitations. The weight of these transducers even if minimal compared to other transducers may affect readings of absolute tension on the chords. However, for dynamic changes in tension, the variation generated by the weight of the transducers is not significant especially in chords with high loads. The crosstalk range is high for these transducers when measuring the forces on marginal chords. Although the crosstalk margin persisted, acquiring data over ten cardiac cycles and averaging the readings over the cardiac cycle reduced high frequency noise error. Electrical drift within the C-ring amplifier box also

114

limited the results in these studies, as drift changes the voltage baseline for measurements.

CHAPTER VIII

CONCLUSIONS

Although not all conditions of mitral annular mechanics were replicated, this study simulated the effect of changing annular geometry and motion on chordae tendineae force distribution and mitral regurgitation due to PM displacement. In addition, the effects of PM displacement on chordal force distribution were also elucidated.

A saddle shaped geometry reduces mitral annulus orifice area by decreasing the septal-lateral diameter of the valve. However, annular shape alone does not significantly affect mitral regurgitation due to papillary muscle displacement because of the mitral valve redundant leaflet design.

Annular geometry directly affects tension on the basal chords by varying the relative distance from their insertion point to the PMs. The tension on the anterior strut chord is significantly reduced by a saddle shaped annular geometry because the secondary curvature of the anterior leaflet causes redirection of the force vectors generated by pressure. The natural configuration of the mitral annulus is that of a three dimensional saddle. In this configuration more chords are extended and a secondary curvature in the leaflets is induced. Therefore, the saddle shaped annulus redistributes the forces on the chordae tendineae leading to a more even distribution of tensions among the chords.

Although, the experiments using the flexible annulus model did not emulate all the conditions that define annular motion *in vivo*, these experiments did revealed important

characteristics of valve function. The tension on the basal chords is directly affected by annulus displacement, as these chords restrict annular motion. Basal chords maintain the mitral valve's geometrical characteristics, isolating the marginal and intermediate chords, and thus, leading to proper coaptation within a changing environment.

Experiments on chordae tendineae tension distribution under different PM positions revealed that different chords are affected in distinct ways by each type of displacement. Both the anterior strut chord and the posterior intermediate chord were mostly affected by apical displacement. The posterior intermediate chord was also significantly sensitive to posterior displacement. The marginal chords appeared to be affected mostly by lateral displacement, although the tension in these chords was to some extent uniform for all PM positions. Basal chords were quite sensitive to all types of displacement. However, larger differences were observed when the papillary muscles were moved apically. Therefore, chords that insert near the annulus are more sensitive to variations in papillary muscle position, since their function is to maintain overall valve integrity within a dynamic environment. Chords, which insert into the leaflets are less sensitive to PM position. This relative isolation from changing conditions may maintain coaptation geometry within a range of working conditions, therefore preventing regurgitation. Further research on this subject, with larger sample sizes, is warranted to obtain more information for individual chords.

The results of this study show how annular shape and displacement are not directly responsible for mitral regurgitation in pathologies such as ischemic heart disease and

dilated cardiomyopathy. However, changes in annular shape and displacement may be caused by alterations in ventricular function, which are underlying causes for mitral regurgitation.

Papillary muscle displacement severely altered chordal force distribution. Changes in force distribution of the chordae tendineae are communicated to the leaflets, inducing tenting or buldging, which has been shown to cause mitral regurgitation.

This study provides important new information on mitral valve function, which leads to a better understanding of the valve under normal and pathological conditions.

CHAPTER IX

RECOMMENDATIONS

The variable annulus shaped atrial chamber was designed to mimic geometrical conditions found during peak systole when the saddle curvature is at its maximum [3][23]. The flexible model reproduced annular motion, which has been to some extent related to mitral regurgitation [4]. However, a truly physiological annulus model which varied in location, size and shape during the cardiac cycle is required to provide more physiological conditions in these studies. In addition, animal studies aimed at measuring the tension on basal chords should be conducted as there is no data available on the subject. This study will not only provide important information on chordal force distribution allowing the construction of more accurate *in vitro* model, but it will also provide important information on PM function and its control over chordae tendineae tension.

The protocol should be modified so that the chordae tendineae cross-sectional area is measured. This will allow us to calculate the stress on the different chords and therefore obtain valuable information about chordae tendineae failure mechanics. Another important factor that should be simulated in future work is PM function including contractility. Therefore, a larger range of physiological and pathological conditions related to PM function could be studied. Ventricular motion should also be incorporated into the model since it is a crucial factor in the physiological and pathological behavior of the mitral valve. Finally, after having a broad understanding of normal MV mechanics,

abnormal valves may be studied in order to understand the mechanics of their pathologies. Surgical procedures could be reproduced *in vitro* using these diseased valves, to observe the effectiveness of the proposed correction methods.

APPENDIX A

BLUE PRINTS

This section contains the blue prints for the variable annular shape atrial chamber used in specific aim 1 and for the flexible annulus model used in specific aim 2. The blue prints include both technical drawings of the different components and the assembly layout.

TABLE OF CONTENTS

FIGURE A.1 VARIABLE ANNULAR SHAPE ATRIAL CHAMBER

A

A

Φ0.20

A-A (5 : 1)

0.50

0.90

R0.30

10.60

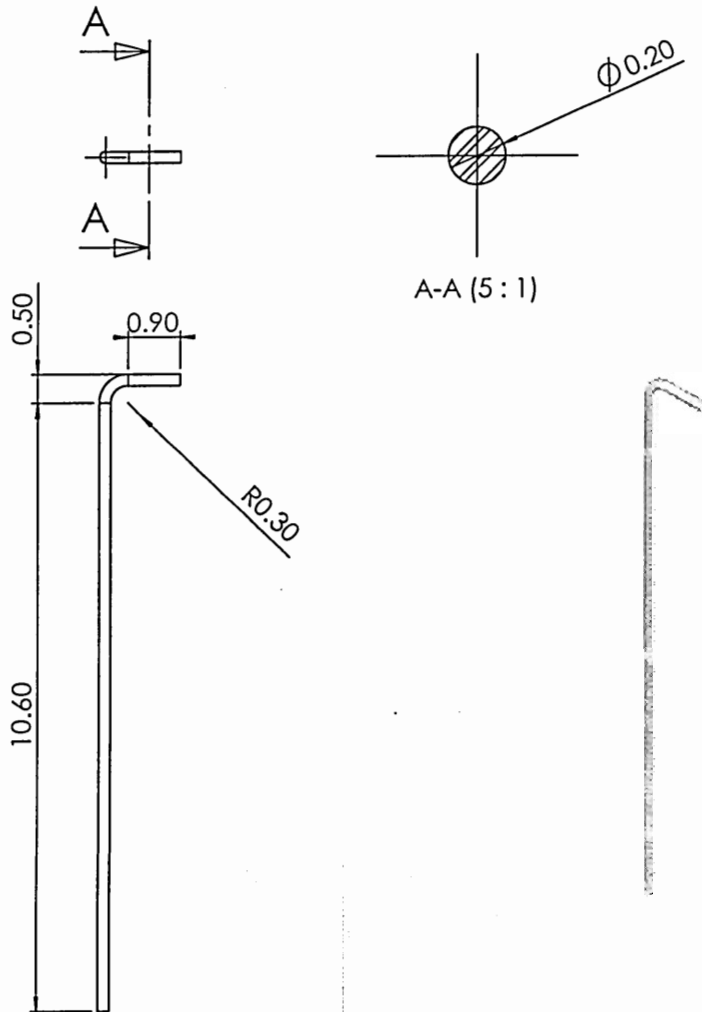| DIMENSIONS ARE IN CMS		NAME	DATE			
TOLERANCES:	DRAWN					
FRACTIONAL±	CHECKED					
ANGULAR: MACH± BEND ±						
TWO PLACE DECIMAL ±	ENG APPR.			FIGURE A.2		
THREE PLACE DECIMAL ±	MFG APPR.			CONTROL ROD		
	Q.A.					
	COMMENTS:					
FINISH				SIZE	DWG. NO.	REV.
	STEEL			A		
Drawing not to scale					WEIGHT:	Page 123

123

Ø 0.50

Ø 0.30

0.60

A-A (3 : 1)

Ø 0.40 ▽ 0.75
M5x0.8 - 6H ▽ 0.75

Ø 1.50

A   A

0.30

FIGURE A.3
CONTROL ROD GUIDE

SIZE **A** DWG. NO.   REV.

WEIGHT: Page 124

FIGURE A.4
PISTON & HOUSING

Ø0.08

2   1.92

1.80

0.30
0.40
0.40   0.30

Ø0.25

HOUSING

PISTON

DIMENSIONS ARE IN CMS		NAME	DATE		
TOLERANCES:	DRAWN				
FRACTIONAL±	CHECKED				
ANGULAR: MACH± BEND ±	ENG APPR.			FIGURE A.4	
TWO PLACE DECIMAL ±	MFG APPR.			PISTON & HOUSING	
THREE PLACE DECIMAL ±	Q.A.				
	COMMENTS:				
FINISH					
	BRASS		SIZE DWG. NO.		REV.
Drawing not to scale			A	WEIGHT:	Page 125

FIGURE A.5
FRONT PANEL
VASAC
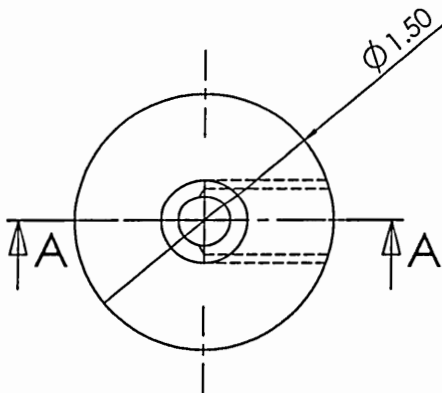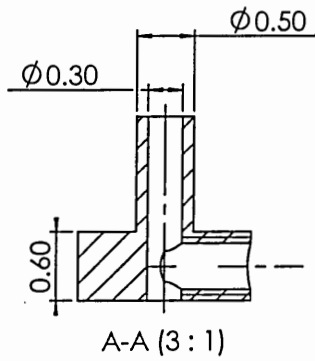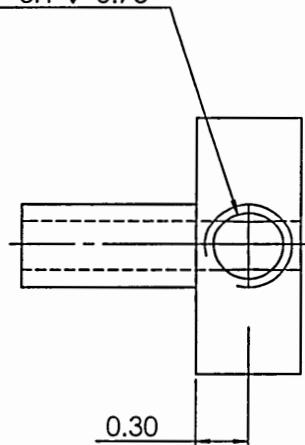
DIMENSIONS ARE IN CMS		NAME	DATE
TOLERANCES: FRACTIONAL± ANGULAR: MACH± BEND ± TWO PLACE DECIMAL ± THREE PLACE DECIMAL ±	DRAWN		
	CHECKED		
	ENG APPR.		
	MFG APPR.		
	Q.A.		
	COMMENTS:		
FINISH	Acrylic		
Drawing not to scale			

11

R0.50
Ø0.60
7
2
1
5.50
3.40
3.90
2.20
0.70
0.60
3.20
1
10
0.30

SIZE DWG. NO. REV.
A
WEIGHT: Page 126

Ø 0.50 ▼ 1.10
M6x1 - 6H ▼ 1.10

Ø0.20
2.25

Ø0.60

A

3.40

3.90

Ø2.50
1.25
Ø2

2

Ø4.50

1.30

5.30

10

9

4

Ø2.60

5.70 2.50
A-A

A

1

0.30

0.70

11

7

2

0.70

5

0.30

1.20

Ø3

1.30

DIMENSIONS ARE IN CMS		NAME	DATE			
TOLERANCES:	DRAWN					
FRACTIONAL±						
ANGULAR: MACH± BEND ±	CHECKED					
TWO PLACE DECIMAL ±	ENG APPR.					
THREE PLACE DECIMAL ±	MFG APPR.			FIGURE A.6		
	Q.A.			VASAC ATRIAL CHAMBER		
	COMMENTS:					
FINISH	Acrylic			SIZE A	DWG. NO.	REV.
DRAWING NOT TO SCALE					WEIGHT:	Page 127

127

FIGURE A.7 FLEXIBLE ANNULUS
MODEL ASSEMBLY

11

R0.50
Ø0.60

7

1

3.40

3.90

3.90

0.70

6

3

1

2

10

0.50

FIGURE A.9
MEMBRANE HOLDER

11
8.80
0.80
1
1
0.60
0.60

R0.50
Ø0.60
7
2
1
3.40
3.90
0.70
6
1
1.10
1
Ø 0.50 ⊽ 1.50
M6x1 - 6H ⊽ 1.20

2.70
3.60
2.60
2.60
10
2.10

DIMENSIONS ARE IN CMS		NAME	DATE
TOLERANCES:			
FRACTIONAL±	DRAWN		
ANGULAR: MACH± BEND ±	CHECKED		
TWO PLACE DECIMAL ±	ENG APPR.		
THREE PLACE DECIMAL ±	MFG APPR.		
	Q.A.		
	COMMENTS:		
FINISH			
Drawing not to scale			

ACRYLIC

FIGURE A.9
MEMBRANE HOLDER

SIZE A | DWG. NO. | REV.
WEIGHT: | Page 130

DIMENSIONS ARE IN CMS		NAME	DATE		
TOLERANCES:	DRAWN				
FRACTIONAL±	CHECKED				
ANGULAR: MACH± BEND ±	ENG APPR.			FIGURE A.10	
TWO PLACE DECIMAL ±	MFG APPR.			FLEXIBLE MODEL	
THREE PLACE DECIMAL ±	Q.A.			ATRIL CHAMBER	
	COMMENTS:				
FINISH	Acrylic		SIZE DWG. NO.		REV.
			A		
DRAWING NOT TO SCALE			WEIGHT:	PAGE 131	

APPENDIX B

C-RING FORCE TRANDUCERS

Materials and Assembly

The C-transducer uses the well-known Wheatstone bridge to measure the force. Half of the Wheatstone bridge is active with two uni-axial strain gauges (SG) (the two R_G's in Figure B.1) and the other bridge-completing half consist of two passive resistors with the same nominal resistance as the active SG's. The passive resistors are located inside an in-house built signal conditioner (R_1 and R_2 in Figure B.1).

R_1 and R_2 are adjustable with potentiometers coupled in parallel to the passive resistors. As mentioned below, the SG's nominal resistance (350 Ohms) will change slightly when they are glued, soldered, and coated. For optimum performance, the Wheatstone bridge needs to be balanced. The balance can be achieved by adjusting the aforementioned potentiometers. A serial connected resistor, Rs in Figure B.1, is used to reduce the power dissipation in the SG's. One SG is attached to the inner surface and the other SG is attached to the outer surface of the C-frame. The C-frame is shown in Figure B.2. When the ends of the C are pulled from each other, the outer SG will compress decreasing its resistance ($-\Delta R$), whereas the inner SG will elongate so its resistance will increase ($+\Delta R$). The variation in resistance will change the output voltage, V_O, which can be measured. As long as the C-frame is not deformed plastically and the applied force is below 6N, the output voltage, V_O, will change linearly with force.

Changes in temperature can be a problem when using SG's, however, assuming that the temperature changes are identical in the two gauges, the ratio of their resistance does not change, and the output voltage, V_O, will not change with fluctuations of temperature . The resistance changes in the SG's are quite small. Amplification of the Wheatstone bridge output voltage is required for further data acquisition.

Strain gauge input modules (SCM5B38-03, Dataforth) are made especially for data acquisition and to be used with strain gauges in a Wheatstone half bridge. Their output range is ±5 Volts, which is a range compatible with most data acquisition cards. They provide a stable, fully isolated excitation voltage (V_{EX} on Figure B.1) of 3.333 V when assembled in half bridges with bridge resistors in the range of 100 Ω to 10 kΩ.
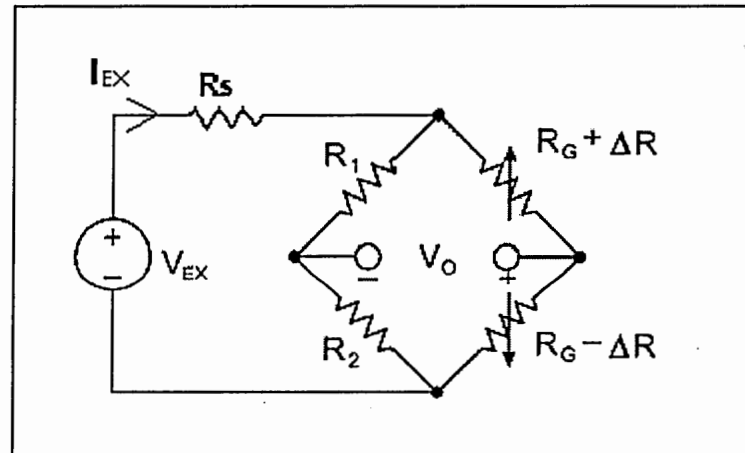
Figure B.1. Diagram of the bridge circuit with series resistor, R_S. Each of the other resistors has a nominal value of 350Ω. V_{EX} is the Wheatstone bridge excitation voltage and is provided by the SG input modules. V_O is the output voltage of the bridge.

The C-frame is made of brass as it is a ductile and corrosion resistant metal within the specified working environment. Furthermore, stresses generated by chordal forces are within the elastic range of brass. Therefore, for this geometry, brass is mechanically appropriate.

The frame for the C-transducer is cut out from a brass pipe with an outer diameter of 6.0mm and inner diameter of 5.0mm. The pipe is sawed into rings, each with a width of 2.0mm. Four holes are drilled (diameter: 0.9mm) in each brass ring. This is accomplished by drilling through the ring twice, perforating two sets of holes, each set opposite of each other. A notch is cut in between the two holes in each end of the C-frame. Rough edges are filed down providing a smooth surface all over the plate.

Figure B.2. C-frame made of brass.

After the C-shaped brass frame has been constructed, it is cleaned with degreaser (CSM-1A Measurement Group©, Raleigh, NC, USA), which is applied with a cotton swab.

After the surface has been degreased the area where the SG will lay, is conditioned using M-Prep Conditioner A (Measurement Group©, Raleigh, NC, USA). The last cleaning step of the SG surface area serves to chemically neutralize it by applying M-Prep

Neutralizer 5A (Measurement Group©, Raleigh, NC, USA). The mounting area to which the SG's will be attached to is now chemically clean and pH neutral.

To ensure an adequately smooth surface at the attachment sites for the SG's and to ensure electric insulation, the areas are bonded using M-Bond 43 B (Measurement Group©, Raleigh, NC, USA). The bonding solution is applied to the area between the two inner holes on the concave and the convex surfaces. To cure the bonding material properly, the C- frames with the bonding solution are heated for an hour at approximately 125°C. Three coats of the solution are applied and cured sequentially. No external element should be in contact with the bonding area during curing.

When the brass frame has been bonded three times, the surface area is smooth enough for SG attachment. The miniature SG's utilized are model EA-06-031DE-350 (Measurement Group©, Raleigh, NC, USA). Their nominal resistance of 350 Ohms is appropriate for the 3.333 Volt Wheatstone bridge excitation voltage considering sensitivity, power dissipation, and noise. The SG's are attached to a foil. The foil is 2 mm x 4 mm, however; the actual gauge area is only 1 mm x 3 mm. Therefore, cutting the area around the actual gauge area is necessary using a scalpel or scissors.

An appropriate amount of ordinary super glue is applied to the area where the SG will be placed on the brass frame. The SG is held down to the surface with tweezers and when in contact with the super glue it is adjusted to the right location (The middle of the gauge is on the middle of the brass frame). When the SG is moved to the right location, thin metal thread (for example the 134-AWP Single Conductor from Measurement Group ©, Raleigh, NC, USA) is held against the SG. Making sure that when the glue is drying the SG follows the curve of the C-shaped brass frame tightly without air bubbles in between

the C-frame and the SG foil (Figure B.3). The thin metal thread is moved gently from side to side while the glue is drying to minimize the chance of it getting glued onto the surface if excessive glue has been applied to the SG foil. The SG's are glued as close as possible to the middle of the C-frame. This is the location where the largest deformation of the C-frame will occur, when longitudinal forces are applied to the C-transducer. Furthermore, the SG's should not be to close to the two innermost holes in the C-frame, which will be evident later.
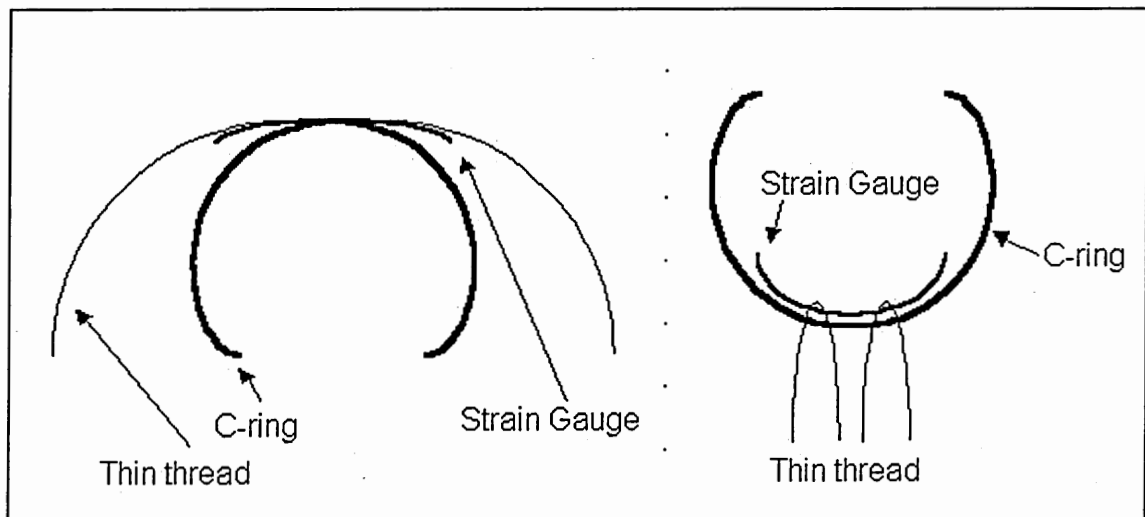
Figure B.3. Left: How the SG is held tightly to the convex surface of the SG while the super glue is drying. Right: How the SG is held to the concave surface while the super glue is curing. The threads are moved from the middle of the SG towards the ends to push out any air bubbles from underneath the SG.

After the superglue has dried, the SG's are interconnected by soldering one end of a thin conducting wire (134-AWP Single Conductor, Measurement Group©, Raleigh, NC, USA) to the leftmost terminal on the outer SG and the other end to the leftmost terminal

on the inner SG when using left/right convention as in Figure B.4. In Figure B.4 the location of the interconnection is where the black conductor is soldered to the outer SG terminal. The thin conducting wire goes around the edge of the C-frame. This interconnection is necessary to complete the Wheatstone half-bridge.

One end of approximately 2 meters of the 336-FTE wire with 3 conducting cables (Measurement Group©, Raleigh, NC, USA) is attached to three of the SG's four solder terminals. The wire is oriented in the C-frame's longitudinal direction. The conducting cable has 3 conductors color coded black, red and white. The insulation around the 3 conductors is made of Teflon. The length of the 3 conductors is adjusted to match the solder terminals on the SG's as shown in Figure B.4. The black conductor follows the edge and the arch in the middle of the C-frame. The Teflon insulation makes the wire stronger mechanically and chemically compared to wires with other insulation materials. This makes it possible to use the very thin and delicate 36 gauge 336-FTE wire. In applications where the C-transducers are sutured to chordae tendineae (CT); thin, light, and flexible wires are used, so the motion of the wires caused by saline flow in the left heart simulator does not affect the CT significantly. Approximately 1.5mm of the Teflon insulation is stripped by holding the end of the conductors into a flame thereby melting the Teflon so it retracts from the end of the metal conductor. The conductors are swiftly soldered to their corresponding solder terminals on the SG. Melting the solder more than a couple of seconds increases the risk of melting the SG foil or destroying the bonding between the SG and the C-frame.
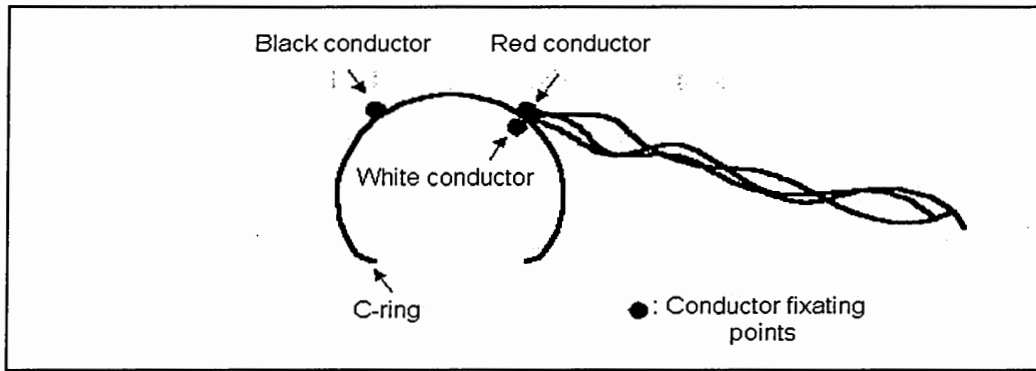
Figure B.4. Attachment sites for the three conductors on the C-frame.

The solder job is tested with an ohmmeter. The soldering will inevitably change the resistance in the SG. If the resistance remains in the range $350\pm5\Omega$ it is considered good enough to provide a stable Wheatstone bridge.

The solder terminals are very fragile. Tying the 3-conductor cable down to the C-frame reduces stress on individual solder terminals. Therefore, the wire consisting of all three conductors are braced to the C-frame with a 2-0 suture (TI-CRON, coated braided polyester suture, USS DG Sutures) to the right of where the red and white conductors are soldered to the SG terminals in Figure B.4. The suture is placed between the SG and the nearest hole in the C-frame.

The electrical circuit requires a highly resistant coating that seals properly and prevents leakage currents as well as mechanical protection.

The area between the two innermost holes on the C-frame is bonded with the same bonding material as mentioned above, M-Bond 43 B. Furthermore, about 2cm of the three conductors are bonded also providing stability around the bracing site with the suture. Again, the bonding is cured as described above. The bonding is repeated three times. The areas around the SG's, solder terminals, and bracing site are now stiffened and

sealed. To maintain a good seal and to protect the sensitive areas, another coating is applied. M-Coat B Nitrile Rubber Coating (Measurement Group©, Raleigh, NC, USA) is applied on top of where the bonding material was applied. The nitrile rubber is applied cold (refrigerator temperature) since this reduces the viscosity. If it is too viscous, it will not cover the conductors, solder terminals, SG's, or the surrounding area properly. Figure B.5 shows a finished C-transducer with wires soldered to the SG's and with the nitrile rubber coating.
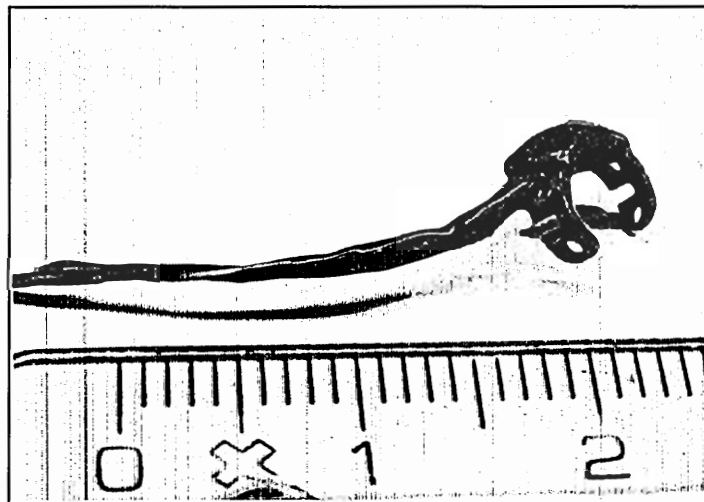
Figure B.5. A C-transducer shown next to a ruler with cm units

The coating is applied once, cured at room temperature for about two hours. Then a second layer is applied followed by 24 hours of cure at room temperature. To further improve chemical resistance, the C-transducer is cured in an oven for one hour at 95 °C. A connector that matches the in-house built signal conditioner is soldered on to the other end of the Teflon wire, which was soldered to the C-frame.

Attachment of Force transducer to the Chordae Tendineae

The CT is attached to the C-transducers by placing the CT in both slits and then suturing it to each end of the C by pulling suture through the holes, through the CT, and tying the suture around the CT finishing with three or four knots. When the CT is attached in both ends, the CT is cut in between allowing the CT tension to be measured by the C-transducer (Figure B.6).
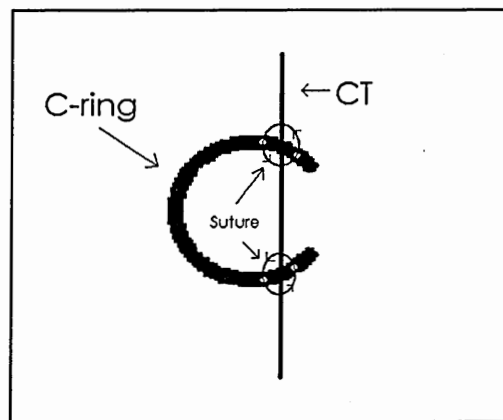
Figure B.6. Diagram of chordal attachment method to the transducer.

Sensitivity

After the C-transducer has been constructed, its sensitivity is measured. The sensitivity is calculated by reading the output voltages from the signal conditioner at known loads. The C-transducer is suspended by the thin wire mentioned before (134-AWP Single Conductor, Measurement Group ©, Raleigh, NC, USA) by pulling the wire through the two leftmost holes (left/right convention as in Figure B.4) it hangs freely about 30cm above a given surface. Another piece of the wire is pulled through the right two holes according to the left/right convention in Figure B.4. Several weights up to a maximum

load of approximately 500g are hung in the latter wire. The corresponding SG input module output voltage is measured. This linear relationship yields a slope coefficient typically around 0.6 Volts per Newton.

Linearity

We have measured sensitivities with weights up to 542g. The maximum force measured in any CT has been close to 3 N. The C-transducers all have a good linear output voltage relationship with loads below the aforementioned 542g. No hysteresis was observed in the force range 0-6 N.

Figure B.7 C-transducer linearity graph with a trend line superimposed on the average of the data points.

The accuracy differs between the C-transducers and depends greatly on variation in sensitivity caused by uneven construction. The best way of describing their accuracies is by looking at their linearity.
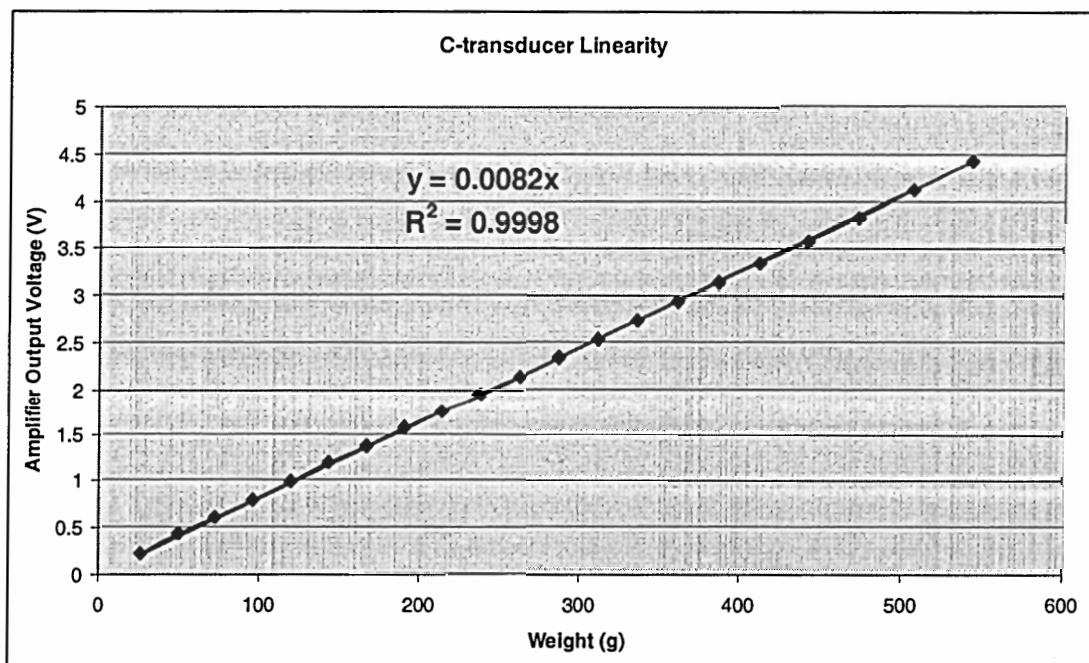
Twenty-one weights, each weighing between 23g and 36g were used to find the linearity. One by one the weights were added and the output voltages were measured from the signal conditioner in between.

The accumulated weight was 542g. Linearity was measured three times. The output voltages measured in each of the three measurements were averaged and the standard deviations were calculated. The highest standard deviation was 0.025V. A trend line was found and the data point furthest away from the trend line was 1.9% from the linear equation of the trend line. The trend was linear giving $R^2 = 0.9998$ (Figure B.7)

The sensitivity range of all C-transducers varies with time. As the C-transducers age, they also tend to become more sensitive. We believe this is due to changes in mechanical resistance and strength of the bonding and coating materials on the C-transducers. The sensitivity typically starts in new C-transducers to be close to 0.5 V/N and for the older C-transducer specimens the sensitivity is closer to 0.7 V/N. The changes in the sensitivities do not happen fast. The change from ~0.5 V/N to ~0.7 V/N is a long process that comes from months of use, if used approximately once per week.

Noise

The forces measured by the C-transducer are averaged over ten heart cycles almost eliminating noise completely. However, with the in-house built signal conditioner that has a low pass filter of order 6 cutting off at 10 kHz and another 2nd order low pass filter

at 500 Hz has a noise level close to that which is below the critical quantization level of the 12 bit analog-to-digital converter (ADC). The quantization level is one half of the least significant bit (½LSB), so in this application with the SG input module voltage output of ±5V it corresponds to 1.22 mV. The highest noise measured with a TrueRMS multimeter (Hewlett Packard 34401A) was 2.1 mV.

Some drift of the C-transducers has been observed. The baseline shifts gradually over hours, in saline solution as well as in free air. The maximum baseline shift that has been observed was not more than 10 mV over a time of 3 hours. Before the C-transducers are used in an experiment, their offset is adjusted with the aforementioned potentiometers. The drift is so slow that it has no impact on experimental results, as cardiac cycles are typically 860ms.

Frequency Response

The frequency response was tested using a random noise test in a model at the Engineering College of Aarhus [68]. The frequency response curve was flat from 0 to 80-120 Hz, which is sufficient for measuring the CT forces. 30 Hz is considered the upper limit of interest for intra cardiac measurements [69].

Lifespan

The C-transducers are quite small and delicate in nature. Their average life is about 90 days under weekly use. We believe that this is due to the cyclic stress on the delicate connections where the conducting wires are soldered onto the SG soldering terminals,

which have a small area. This causes open circuits in the Wheatstone bridge, leading to C-transducer malfunction..

The C-transducers have been used in applications where the environment has limited space and is chemically hostile. However, the technology behind the C-shaped transducers can be used in many different applications. The C-transducers are very good at measuring longitudinal forces because of their attractive properties like low noise, good linearity, and ability to work in harsh environments. The weakest part of the C-transducers is probably the connection between the wires and the soldering terminals. If the C-transducers are used in another application where they are allowed to be bigger, the problem with this weak connection would be circumvented.

APPENDIX C

REPRESENTATIVE GRAPHS

This section contains chordal force distribution and trans-mitral pressure graphs during the cardiac cycle for representative valves of specific aims 1, 2, and 3.

TABLE OF CONTENTS

Figure C.1. Chordal force distribution and trans-mitral pressure for valve 1 in the flat annulus configuration
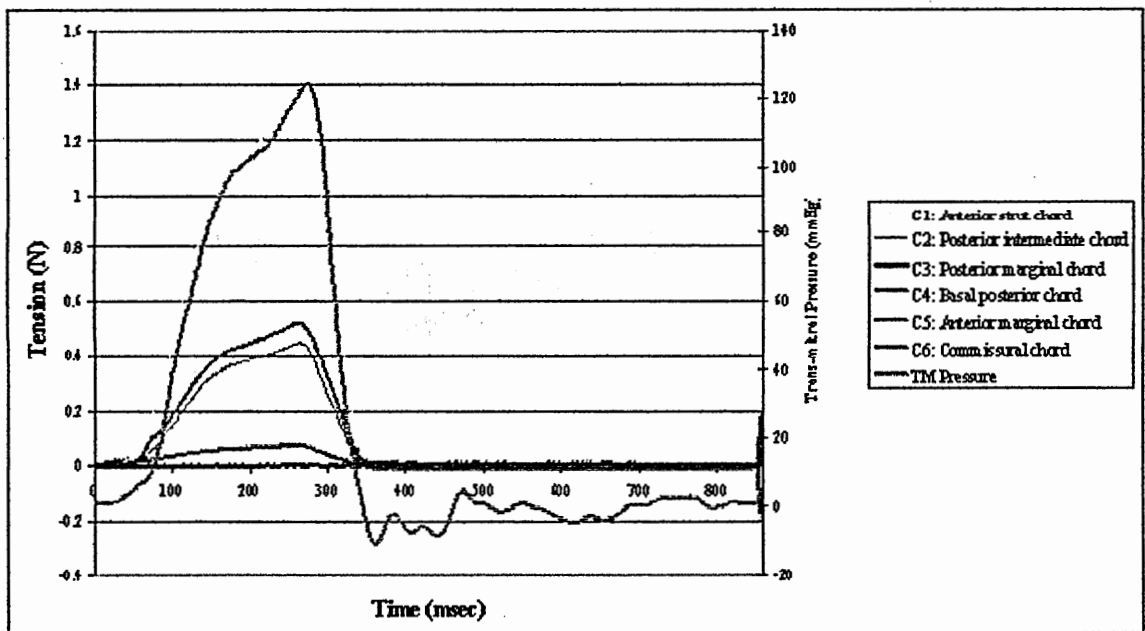
Figure C.2. Chordal force distribution and trans-mitral pressure for valve 1 in the saddled annulus configuration

146
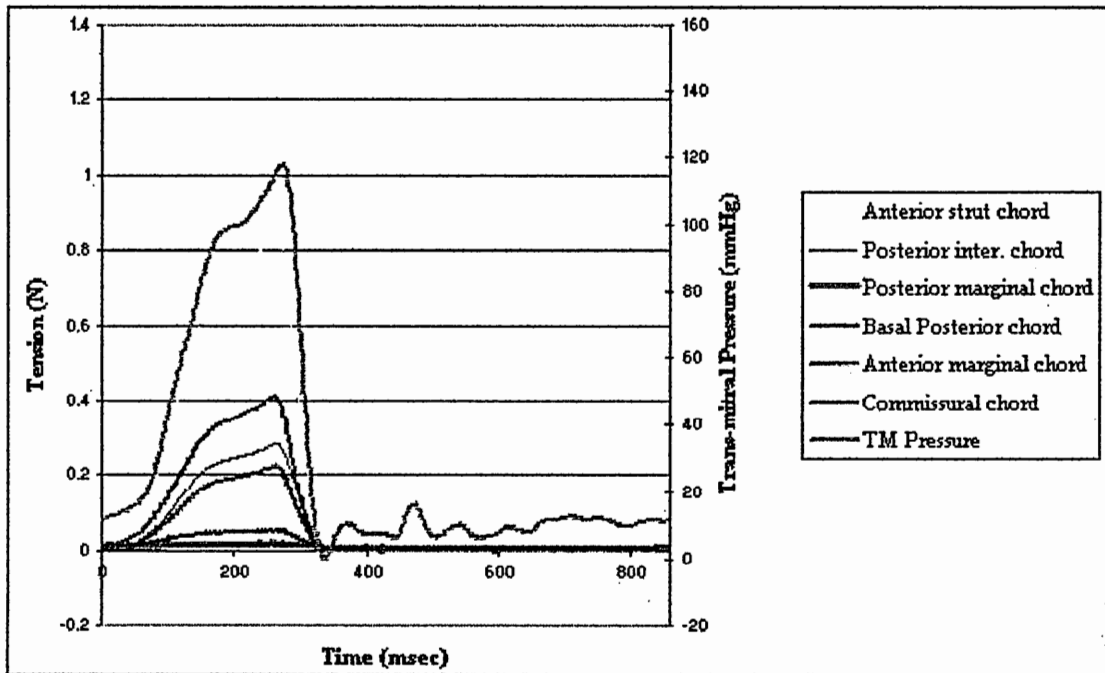
Figure C.3. Chordal force distribution and trans-mitral pressure for valve 2 in the flat annulus configuration
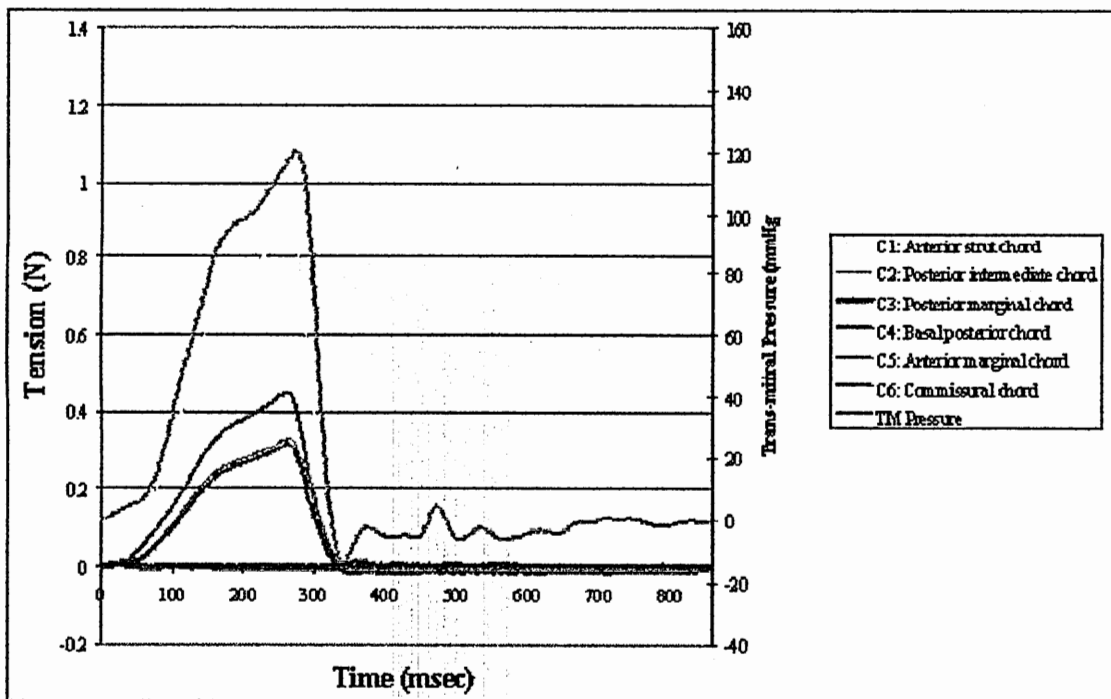
Figure C.4. Chordal force distribution and trans-mitral pressure for valve 1 in the saddled annulus configuration
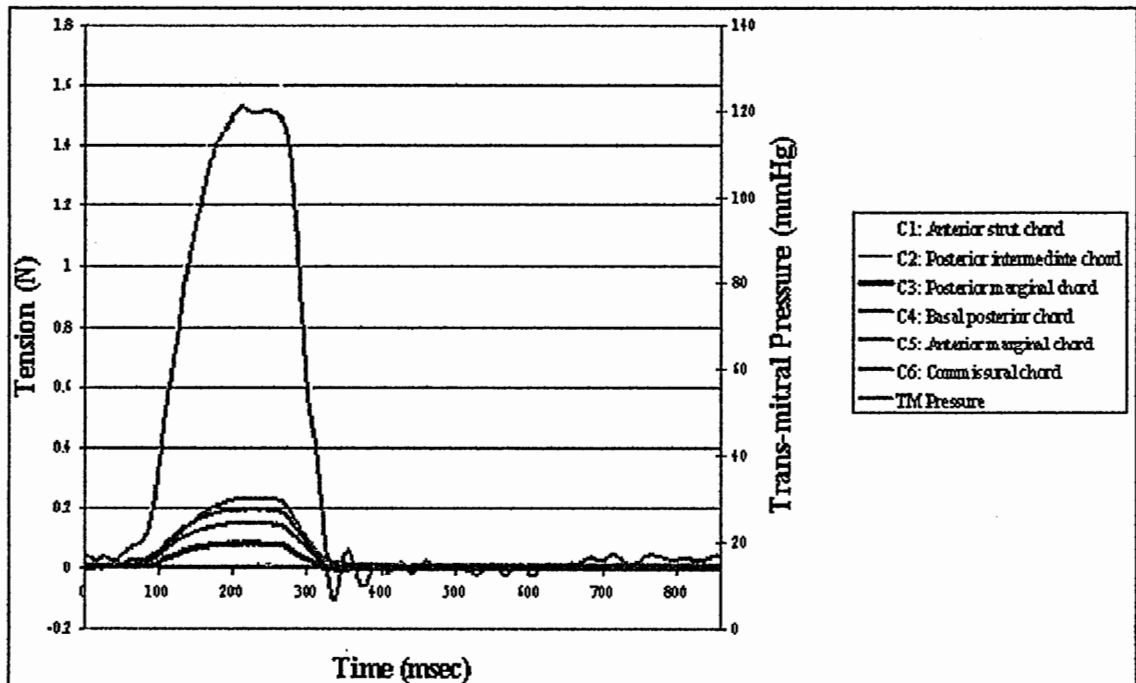
Figure C.5. Chordal force distribution and trans-mitral pressure for valve 5 in the flat annulus configuration
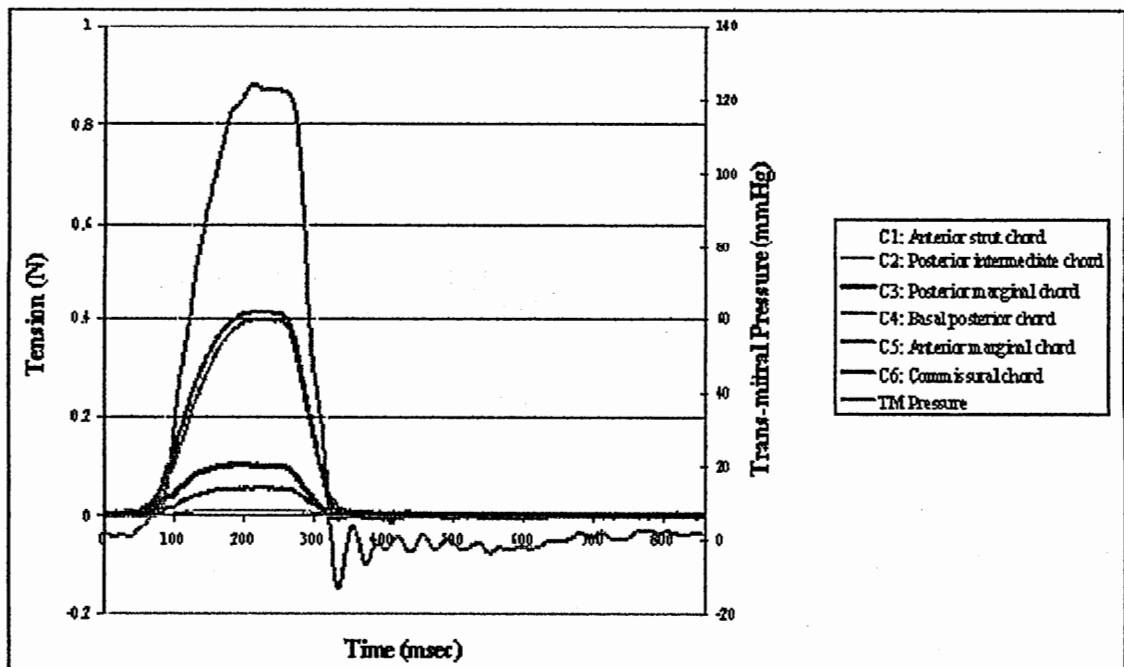
Figure C.6. Chordal force distribution and trans-mitral pressure for valve 1 in the saddled annulus configuration
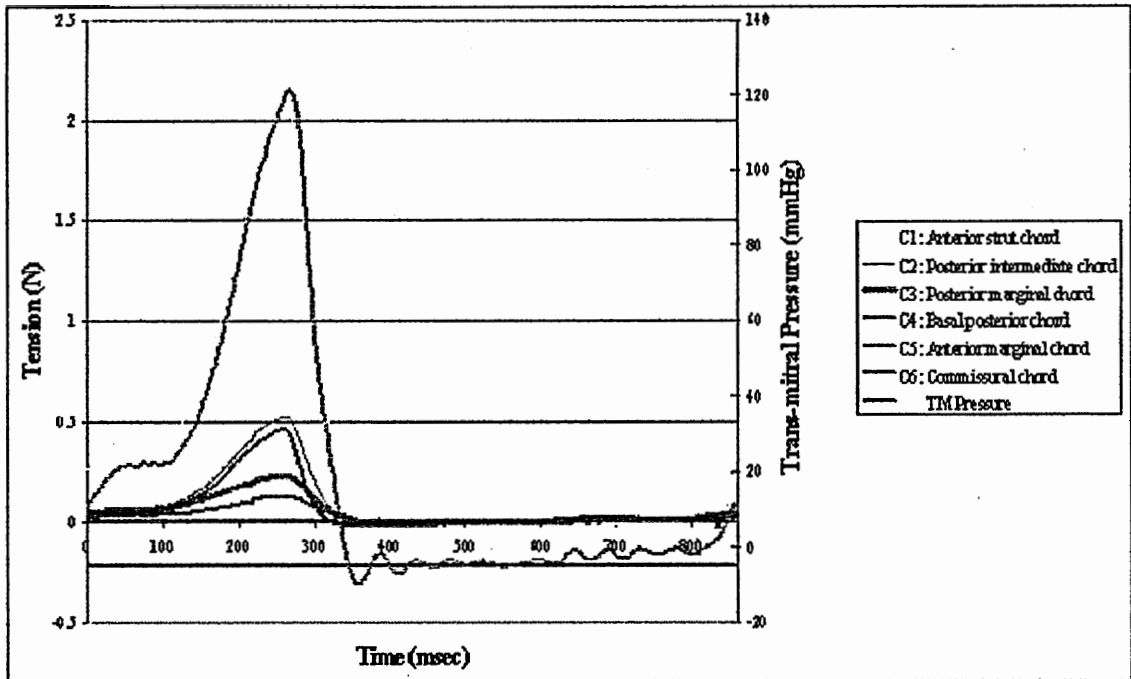
Figure C.7. Chordal force distribution and trans-mitral pressure for valve 1 using the flexible annulus model
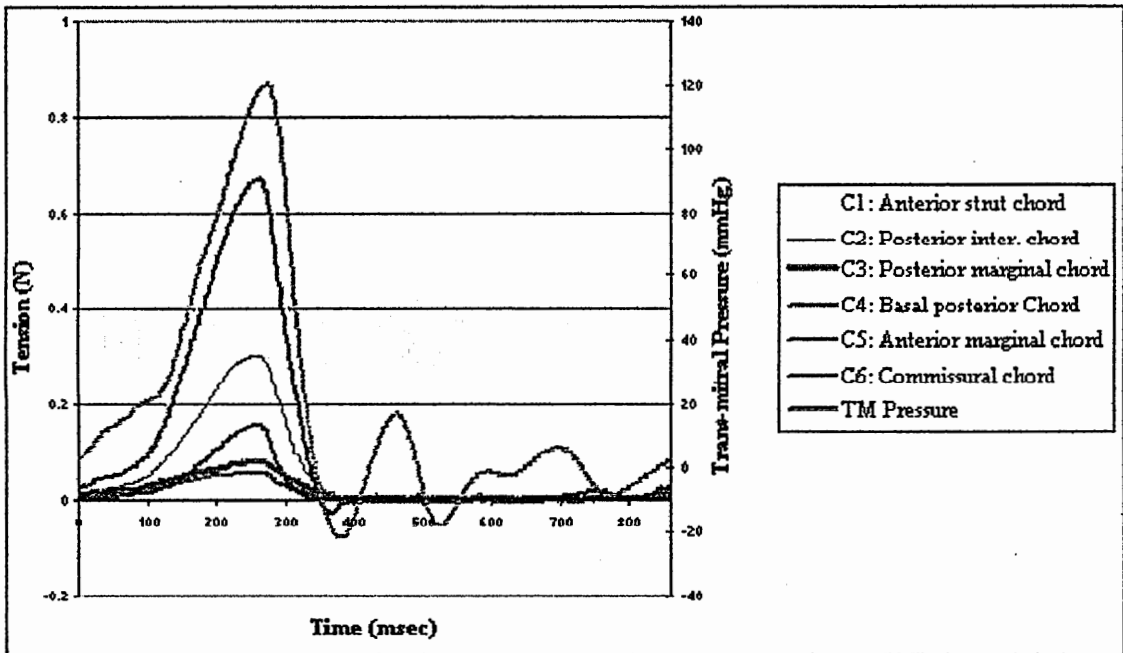
Figure C.8. Chordal force distribution and trans-mitral pressure for valve 4 using the flexible annulus model
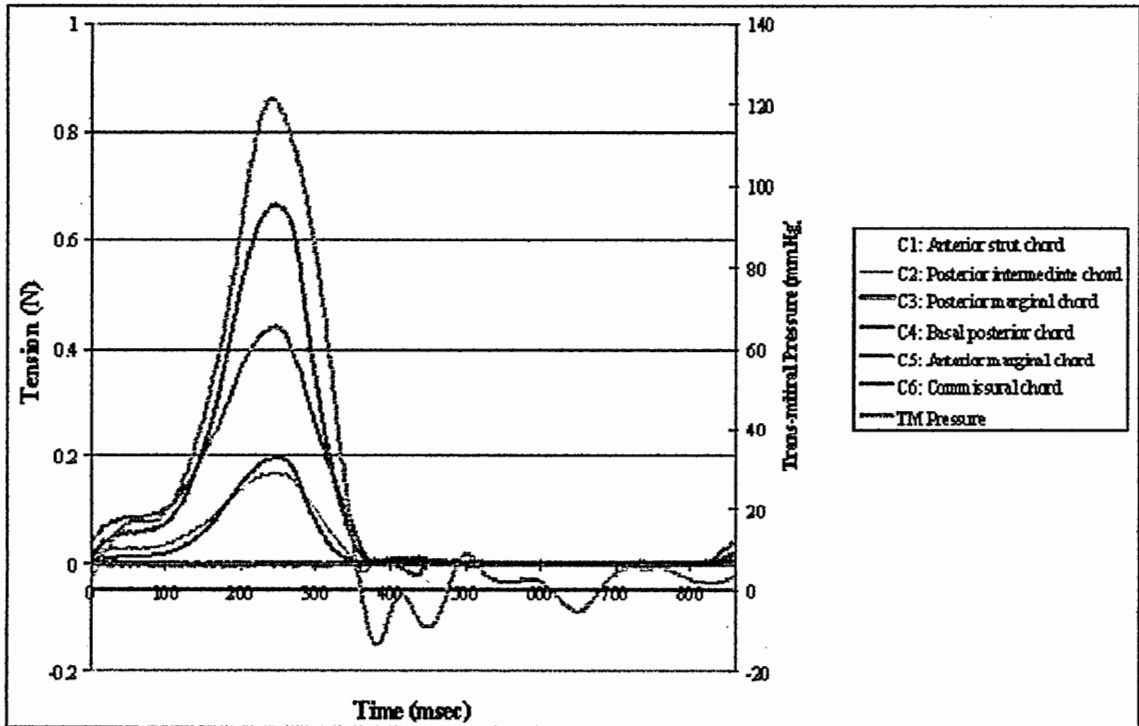
Figure C.9. Chordal force distribution and trans-mitral pressure for valve 5 using the flexible annulus model

150
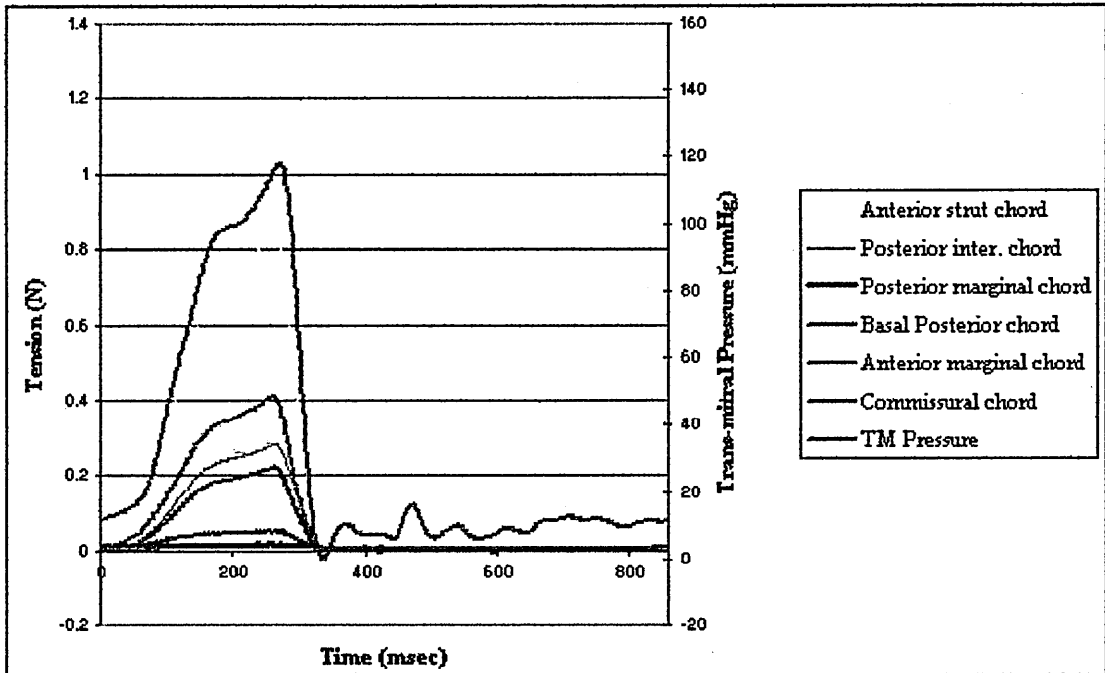
Figure C.10. Chordal force distribution and trans-mitral pressure for valve 3 in the 000 papillary muscle position.
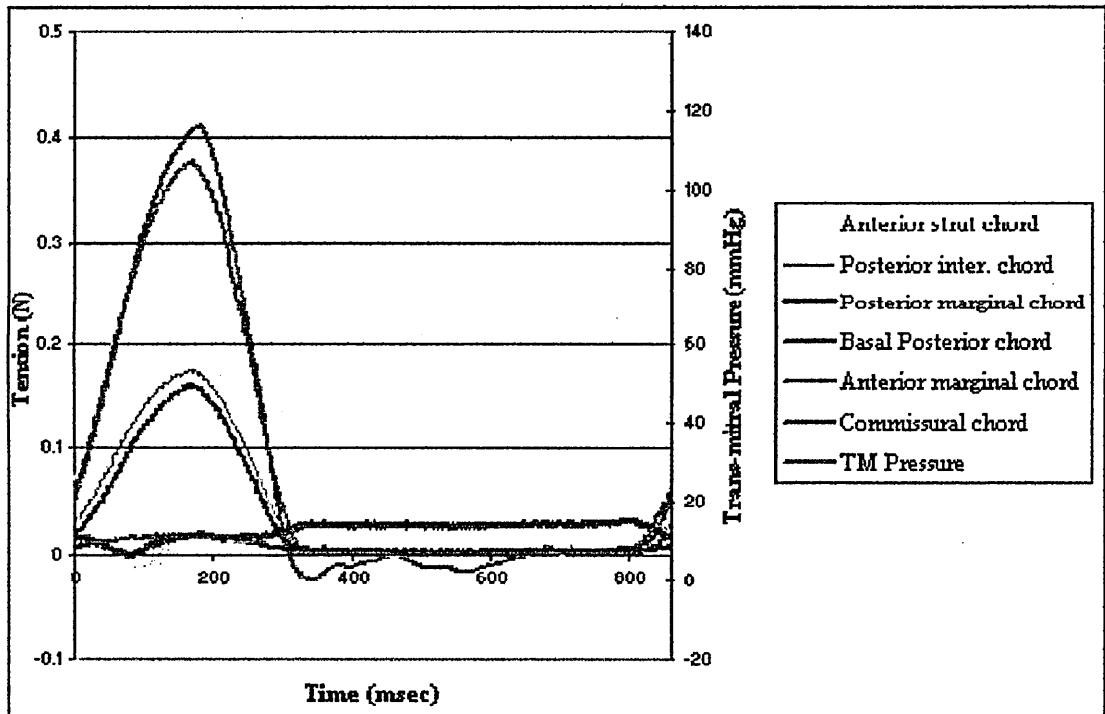
Figure C.11. Chordal force distribution and trans-mitral pressure for valve 3 in the 005 papillary muscle position.
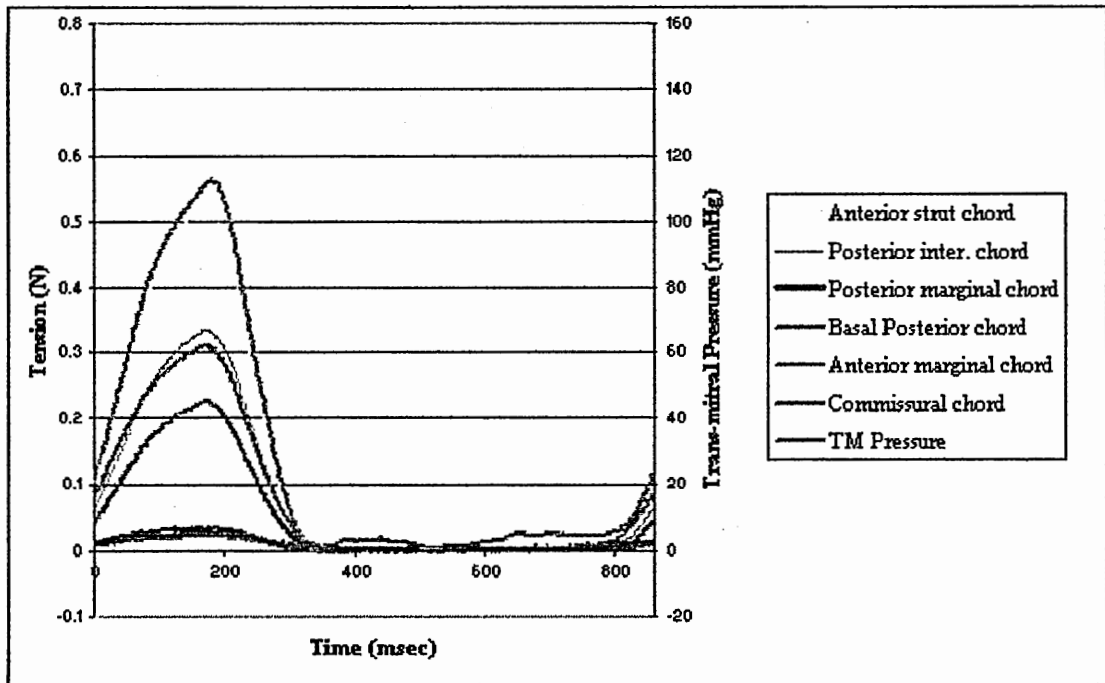
Figure C.12. Chordal force distribution and trans-mitral pressure for valve 3 in the 050 papillary muscle position.
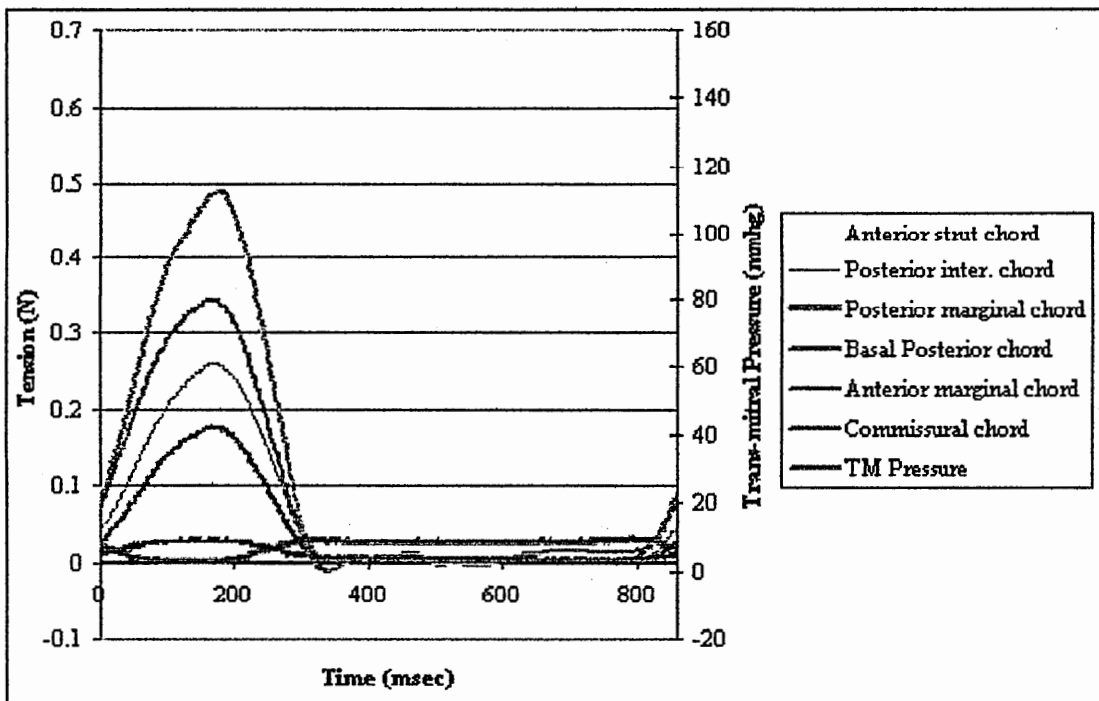
Figure C.13. Chordal force distribution and trans-mitral pressure for valve 3 in the 055 papillary muscle position.
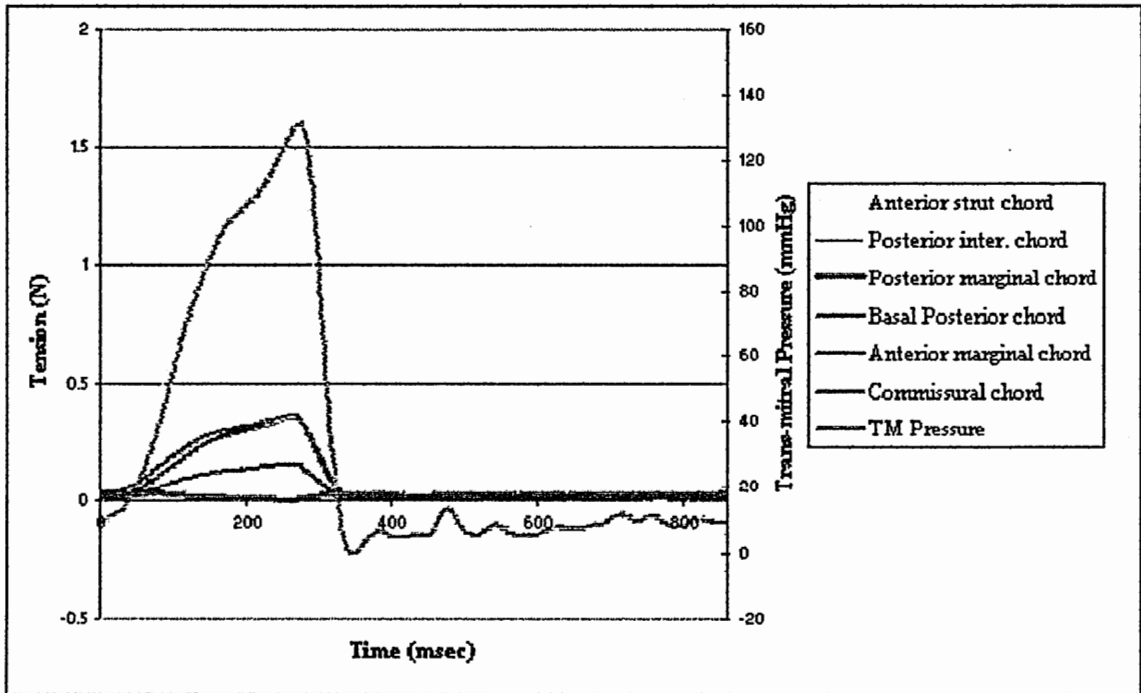
Figure C.14. Chordal force distribution and trans-mitral pressure for valve 3 in the 500 papillary muscle position.
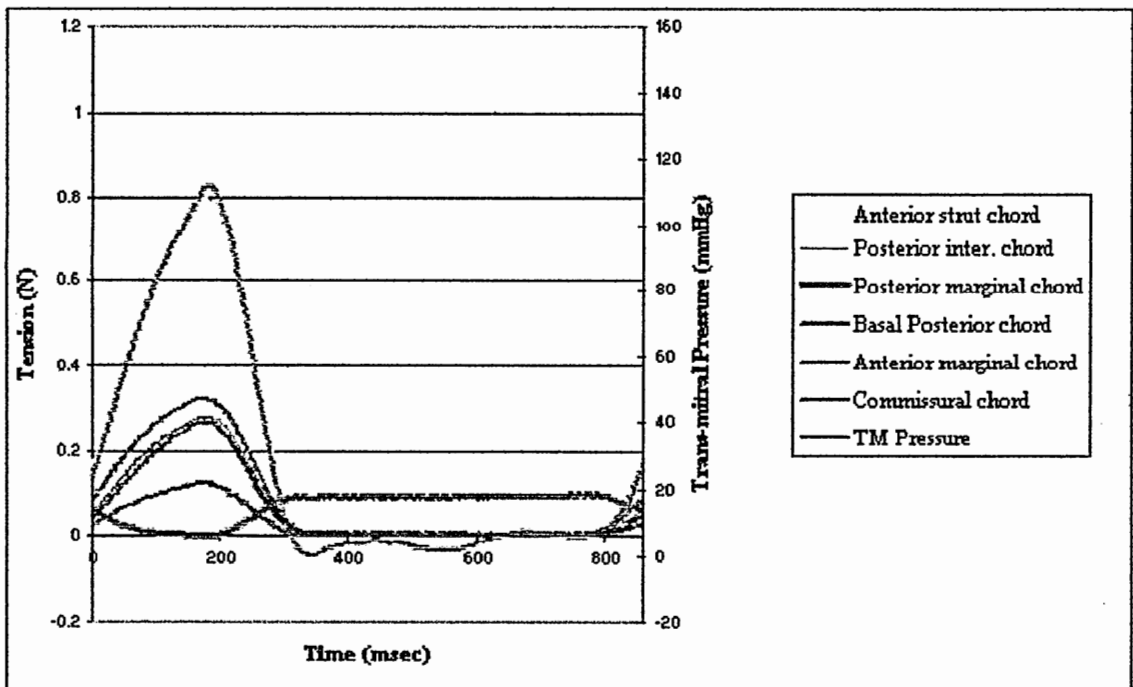
Figure C.15. Chordal force distribution and trans-mitral pressure for valve 3 in the 505 papillary muscle position.

153
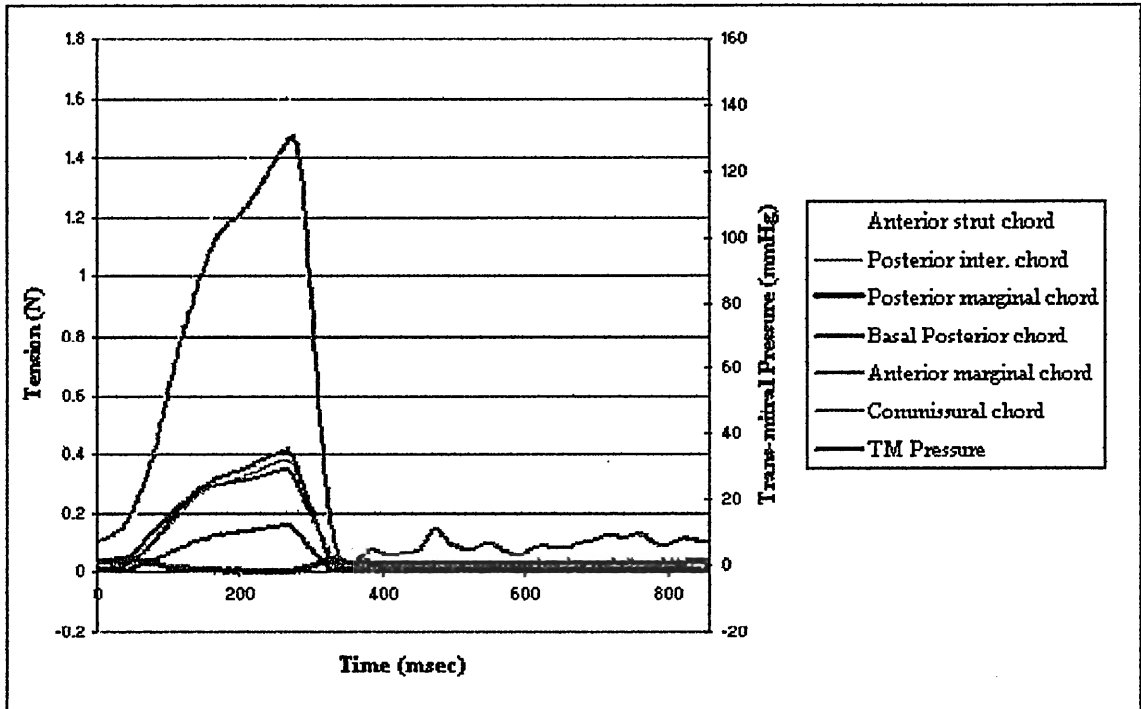
Figure C.16. Chordal force distribution and trans-mitral pressure for valve 3 in the 550 papillary muscle position.
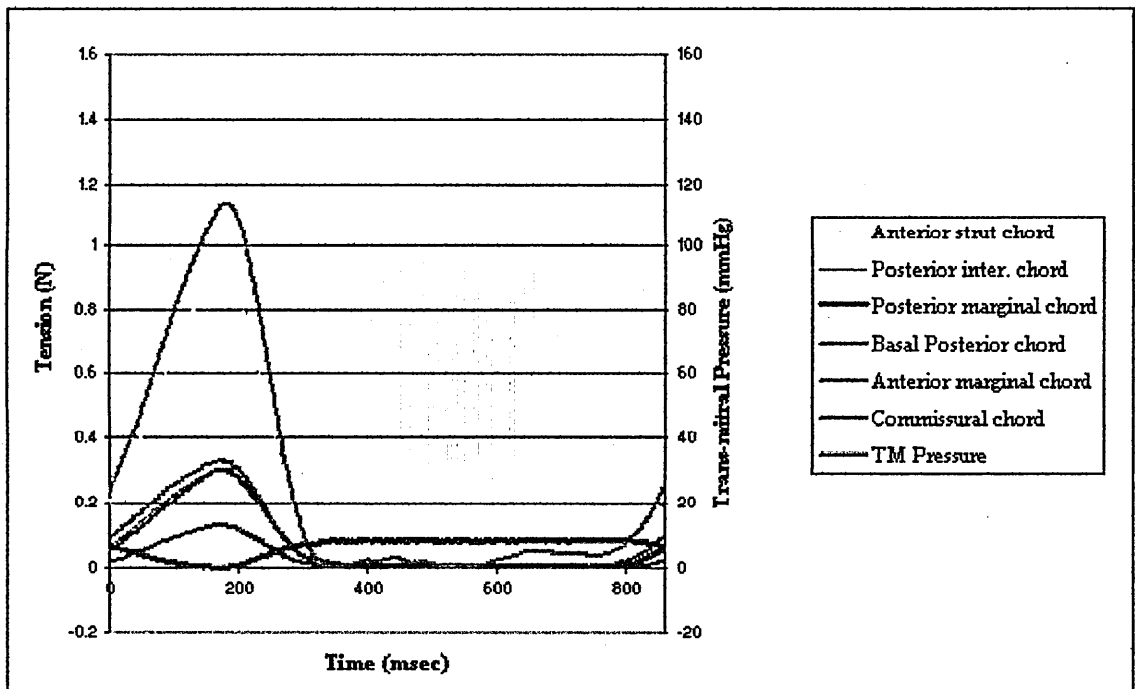
Figure C.17. Chordal force distribution and trans-mitral pressure for valve 3 in the 555 papillary muscle position.

154
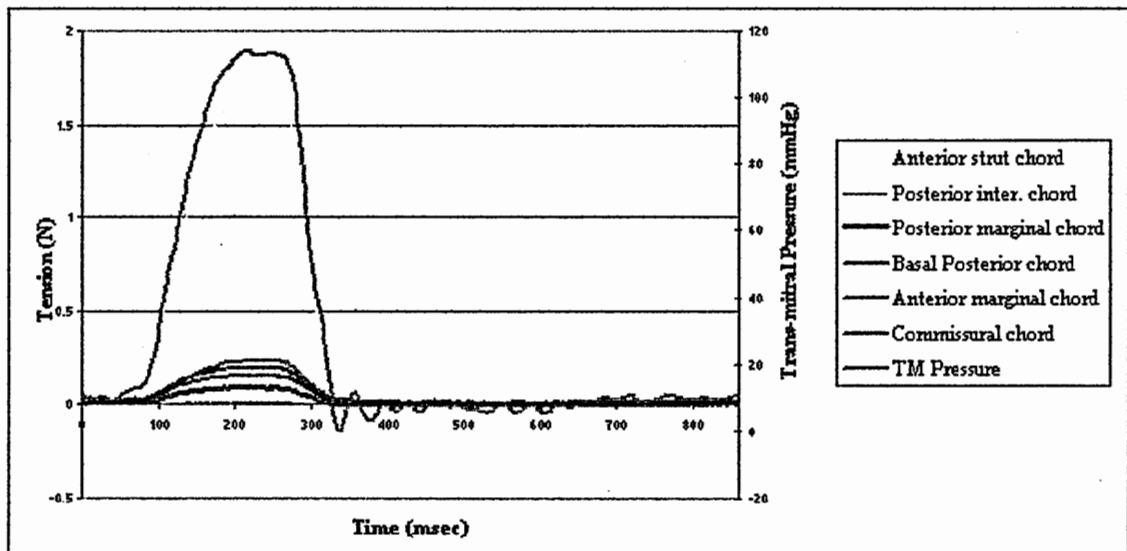
Figure C.18. Chordal force distribution and trans-mitral pressure for valve 10 in the 000 papillary muscle position.
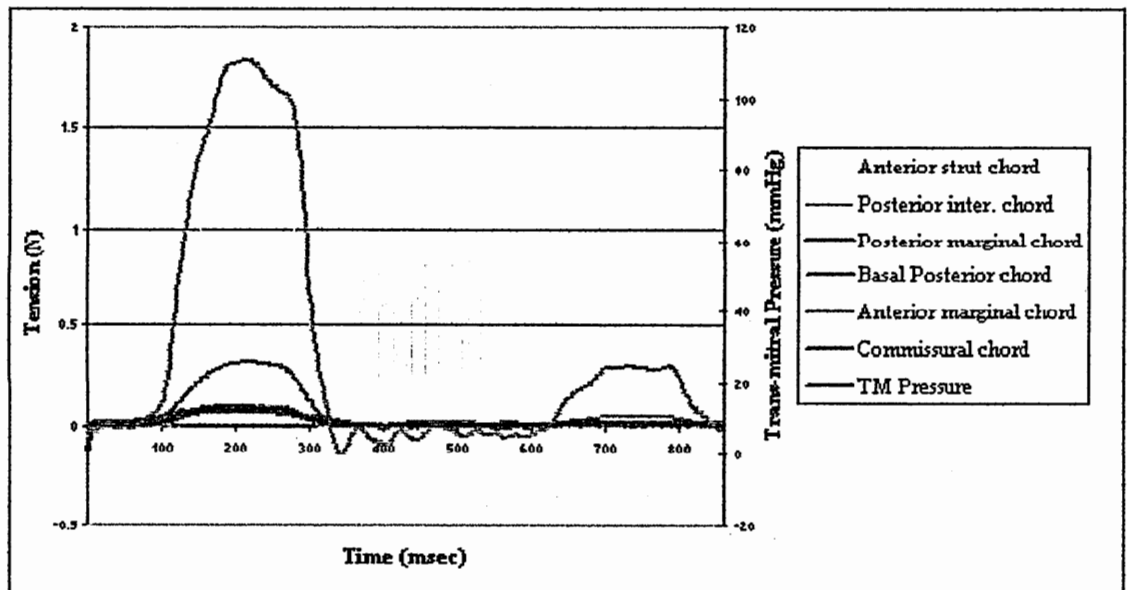
Figure C.19. Chordal force distribution and trans-mitral pressure for valve 10 in the 005 papillary muscle position.
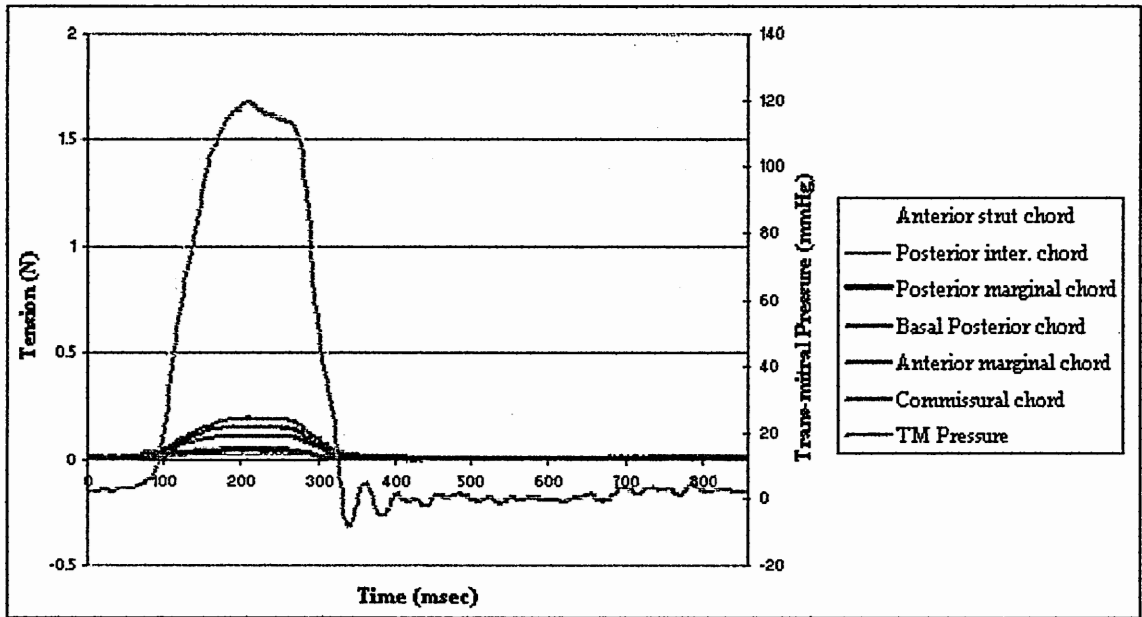
Figure C.20. Chordal force distribution and trans-mitral pressure for valve 10 in the 050 papillary muscle position.
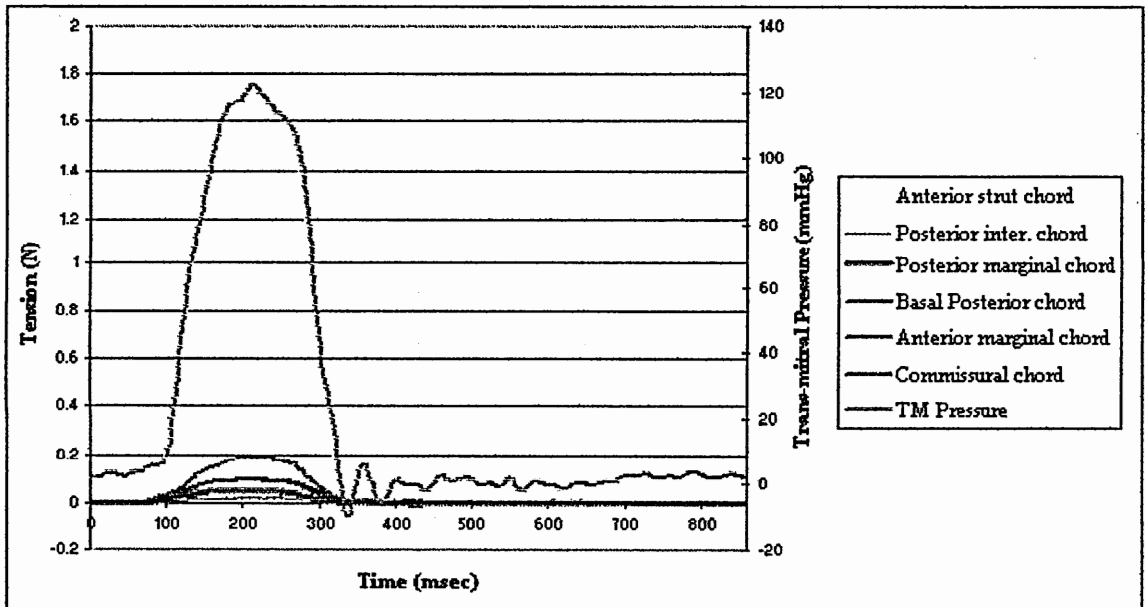
Figure C.21. Chordal force distribution and trans-mitral pressure for valve 10 in the 055 papillary muscle position.

156
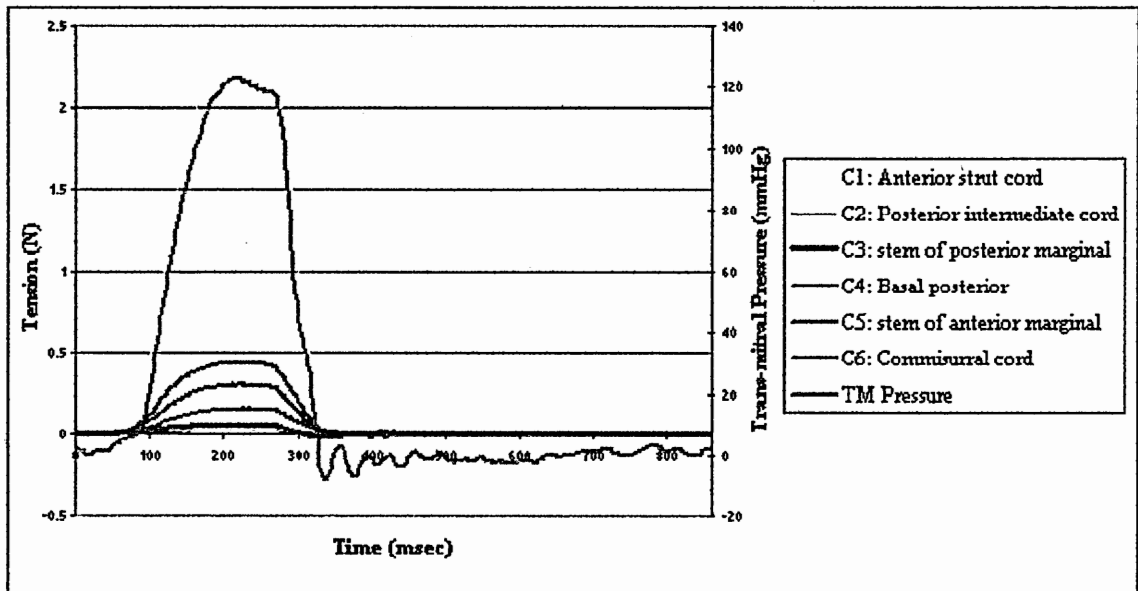
Figure 22. Chordal force distribution and trans-mitral pressure for valve 10 in the 500 papillary muscle position.
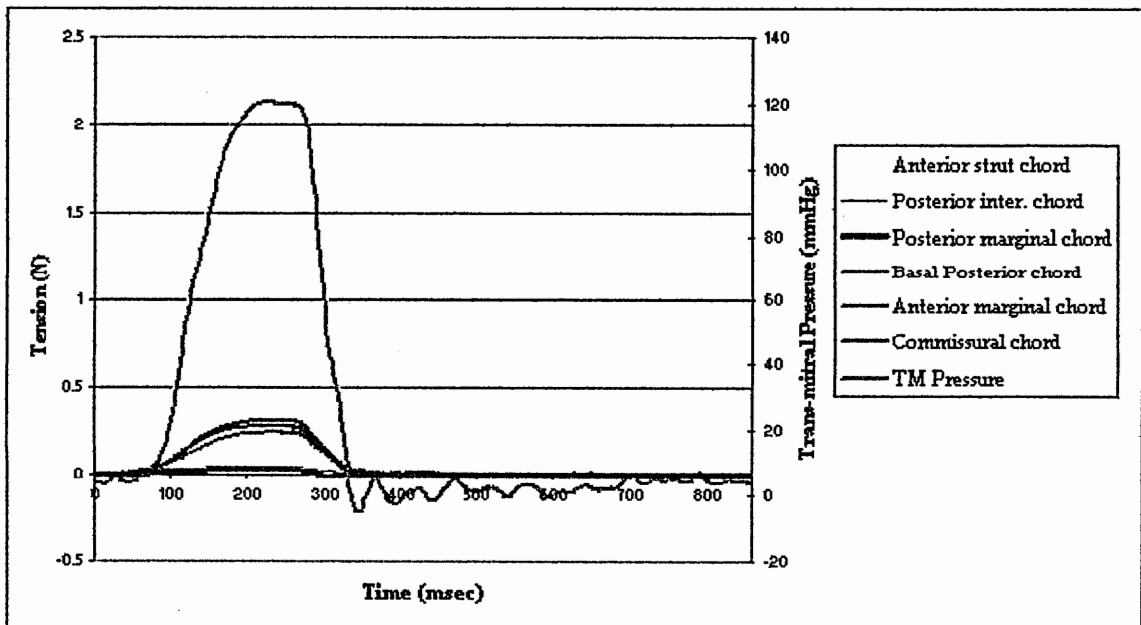
Figure 23. Chordal force distribution and trans-mitral pressure for valve 10 in the 505 papillary muscle position.

157
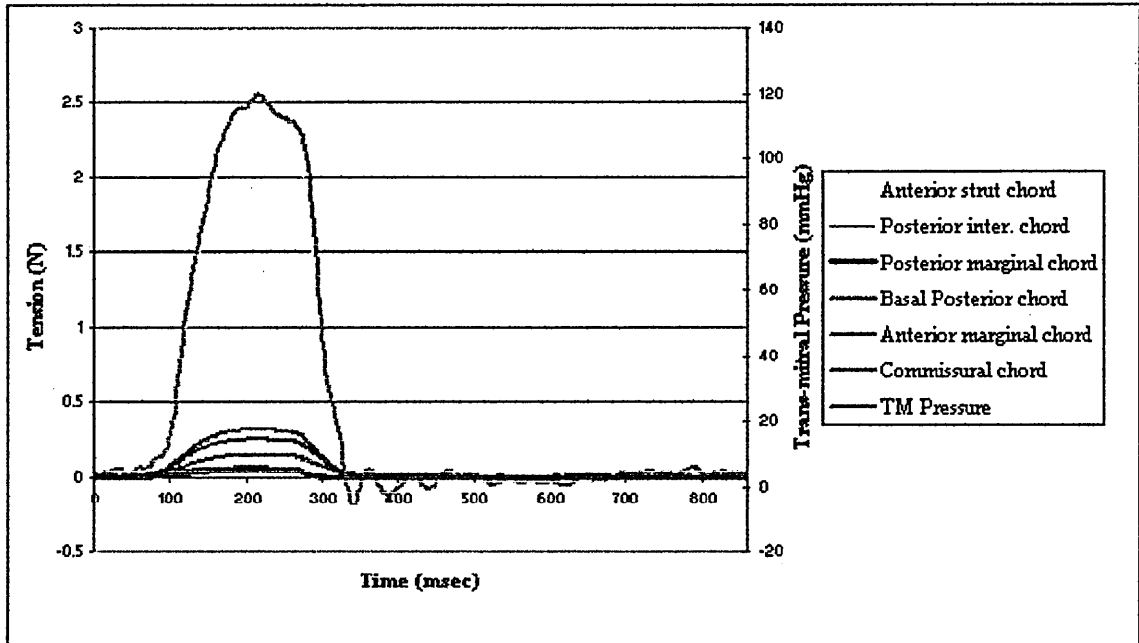
Figure 24. Chordal force distribution and trans-mitral pressure for valve 10 in the 555 papillary muscle position.

APPENDIX D

DATA

This section contains data on peak systolic tension, regurgitation volumes, and annulus displacement for all the experiments in specific aims 1, 2, and 3.

160

Regurgitation Volumes For Experiments in Specific Aim 1
With Papillary Muscle Displacement

Table D.1. Regurgitation Volumes in the displaced papillary muscle position
Values include closing volumes and leakage

Valve Number	Saddle Annulus Regurgitation Volume (ml/beat)	Saddle Annulus Regurgitation Volume (ml/beat)
1	11.2	11.5
2	9.8	10.9
3	10.8	7.8
4	7.2	9.2
5	14.4	15.8
6	16.6	13.9
7	11.2	14.6
8	2.6	4.8
9	7.6	13.1
10	9.7	11.9
11	6.4	6.3
Mean	9.8	10.9
Standard Deviation	4.1	3.5

Peak Systolic Tensions For Experiments In Specific Aim 1

Table D.2. Peak systolic tension (PST) for individual chords in the flat annulus configuration

Valve Number	Experiment Date	Trans-mitral Pressure (mmHg)	Anterior Strut PST (N)	Post. Intermediate PST (N)	Post. Marginal PST (N)	Basal Posterior PST (N)	Anterior marginal PST (N)	Commissural PST (N)
1	18-Jun	117.4	1.620	0.302		0.060	0.445	0.006
2	21-Jun	119.8	0.966	0.313	0.017	0.245	0.459	0.057
3	28-Jun	120.7	1.449	0.003	0.007	0.242	0.444	0.031
4	9-Aug	120.6	0.485	0.356	0.006	0.091	0.273	0.109
5	29-Aug	119.6	1.864	0.009	0.095	0.215	0.247	0.168
6	30-Oct	120.4	0.911	0.254	0.017	0.297	0.018	0.487

Table D.3. Peak systolic tension (PST) for individual chords in the saddle annulus configuration

Valve Number	Experiment Date	Trans-mitral Pressure (mmHg)	Anterior Strut PST (N)	Post. Intermediate PST (N)	Post. Marginal PST (N)	Basal Posterior PST (N)	Anterior marginal PST (N)	Commissural PST (N)
1	18-Jun	124.2	1.384	0.449		0.075	0.516	0.008
2	21-Jun	120.4	0.879	0.332	0.019	0.315	0.450	0.005
3	28-Jun	119.6	1.310	0.003	0.015	0.738	0.392	0.010
4	9-Aug	120.7	0.436	0.443	0.007	0.040	0.306	0.042
5	29-Aug	120.8	0.919	0.011	0.101	0.404	0.386	0.053
6	30-Oct	120.8	0.752	0.273	0.088	0.298	0.068	0.463

Data in grey was discarded because it was below the 0.01N threshold

Peak Systolic Tensions Comparison Between the
Saddle and Flat Annulus Configurations

Table D.4. Anterior strut chord peak systolic tension (PST) values for the flat and saddle annular configurations

Valve Number	Flat Annulus PTS (N)	Saddled Annulus PTS (N)	Difference (N)	Difference (%)
1	1.62	1.38	0.24	14.59
2	0.97	0.88	0.09	8.98
3	1.45	1.31	0.14	9.58
4	0.49	0.44	0.05	10.16
5	1.86	0.92	0.95	50.72
6	0.91	0.75	0.16	17.47
mean	1.22	0.95	0.27	18.58
Standard Deviation	0.52	0.35	0.34	16.09

Table D.5. Posterior intemediate chord peak systolic tension (PST) values for the flat and saddle annular configurations

Valve Number	Flat Annulus PTS (N)	Saddled Annulus PTS (N)	Difference (N)	Difference (%)
1	0.30	0.45	-0.15	-48.64
2	0.31	0.33	-0.02	-6.22
4	0.36	0.44	-0.09	-24.32
5	0.01	0.01	0.00	-25.00
6	0.25	0.27	-0.02	-7.67
mean	0.25	0.30	-0.05	-22.37
Standard Deviation	0.14	0.18	0.06	17.16

Table D.6. Posterior marginal chord peak systolic tension (PST) values for the flat and saddle annular configurations

Valve Number	Flat Annulus PTS (N)	Saddled Annulus PTS (N)	Difference (N)	Difference (%)
2	0.02	0.02	0.00	-16.00
3	0.01	0.02	-0.01	-117.86
5	0.09	0.10	-0.01	-6.44
6	0.02	0.09	-0.07	-410.79
mean	0.03	0.06	-0.02	-137.77
Standard Deviation	0.04	0.04	0.03	188.87

Table D.7. Basal posterior chord peak systolic tension (PST) values for the flat and saddle annular configurations

Valve Number	Flat Annulus PTS (N)	Saddled Annulus PTS (N)	Difference (N)	Difference (%)
1	0.06	0.07	-0.02	-25.21
2	0.25	0.31	-0.07	-28.22
3	0.24	0.74	-0.50	-205.08
4	0.09	0.04	0.05	56.43
5	0.21	0.40	-0.19	-88.30
6	0.30	0.30	0.00	-0.45
mean	0.19	0.31	-0.12	-48.47
Standard Deviation	0.09	0.25	0.20	89.86

Table D.8. Anterior marginal chord peak systolic tension (PST) values for the flat and saddle annular configurations

Valve Number	Flat Annulus PTS (N)	Saddled Annulus PTS (N)	Difference (N)	Difference (%)
1	0.44	0.52	-0.07	-16.10
2	0.46	0.45	0.01	2.06
3	0.44	0.39	0.05	11.63
4	0.27	0.31	-0.03	-12.21
5	0.25	0.39	-0.14	-56.60
6	0.02	0.07	-0.05	-279.63
mean	0.31	0.35	-0.04	-58.47
Standard Deviation	0.17	0.16	0.07	110.84

Table D.9. Commissural chord peak systolic tension (PST) values for the flat and saddle annular configurations

Valve Number	Flat Annulus PTS (N)	Saddled Annulus PTS (N)	Difference (N)	Difference (%)
2	0.06	0.00	0.05	91.47
3	0.03	0.01	0.02	68.73
4	0.11	0.04	0.07	60.92
5	0.17	0.05	0.12	68.76
6	0.49	0.46	0.02	4.93
mean	0.17	0.11	0.06	58.96
Standard Deviation	0.18	0.20	0.04	32.29

Table D.10. Regurgitation Volumes using the flexible annulus model for the normal and diplaced papillary muscle positions

Valve Number	Normal Papillary muscle position Closing Volume (ml/beat)	Displaced Papillary muscles Regurgitation Volume (ml/beat)
1	11.3	17.6
2	14.2	
3	14.7	16.3
4	14.5	18.3
5	14.8	
6	14.9	14.9

Mean	14.1	16.8
Standard Deviation	1.4	1.5

Table D.11. Annular displacement for the normal and displaced papillary muscle positions

Valve Number	Normal Papillary muscle position Apico-basal Displacement (mm)	Displaced Papillary muscles Apico-basal Displacement (mm)
1	3.3	2.2
2	4.1	2.5
3	3.3	2.4
4	4.6	3.4
5	3.9	

Mean	3.8	2.6
Standard Deviation	0.6	0.6

Peak Systolic Tensions For Experiments In Specific Aim 2
and Comparison to Results form Specific Aim 1

Table D.12 . Peak systolic tension (PST) for individual chords using the flexible annulus model

Valve Number	Experiment Date	Trans-mitral Pressure (mmHg)	Anterior Strut PST (N)	Post. Intermediate PST (N)	Post. Marginal PST (N)	Basal Posterior PST (N)	Anterior marginal PST (N)	Commissural PST (N)
1	21-Aug	121.1	2.06	0.52	0.23		0.12	0.46
2	15-Jul	118.7	0.81	0.30		0.12		0.10
3	20-Sep	119.6	1.27	0.29	0.01	0.33	0.22	0.55
4	23-Apr	120.3	0.77	0.30	0.08	0.67	0.05	0.15
5	3-Apr	121.1	0.67	0.17	0.00	0.66	0.44	0.19
6	7-Mar	121.1		0.14		0.63	0.05	0.92
Mean		120.3	1.11	0.29	0.08	0.48	0.18	0.40
Standard Deviation		1.0	0.57	0.14	0.11	0.25	0.16	0.31

Table D.13 . Peak systolic tension (PST) for the different types of chords in the different annulus configurations (Specific aims 1 and 2)

Chordal type and Annulus Type	Intermediate Chords			Marginal Chords			Basal Chords		
	Flexible Annulus PST (N)	Flat Annulus PST (N)	Saddled Annulus PST (N)	Flexible Annulus PST (N)	Flat Annulus PST (N)	Saddled Annulus PST (N)	Flexible Annulus PST (N)	Flat Annulus PST (N)	Saddled Annulus PST (N)
Peak Systolic Tension (N)	2.06	1.62	1.38	0.12	0.44	0.52	0.46	0.06	0.00
	0.81	0.97	0.88	0.22	0.46	0.45	0.10	0.03	0.01
	1.27	1.45	1.31	0.05	0.44	0.39	0.55	0.11	0.04
	0.77	0.49	0.44	0.44	0.27	0.31	0.15	0.17	0.05
	0.67	1.86	0.92	0.05	0.25	0.39	0.19	0.49	0.46
	0.52	0.91	0.75	0.23	0.02	0.07	0.92	0.06	0.07
	0.30	0.30	0.45	0.01	0.02	0.02	0.12	0.25	0.31
	0.29	0.31	0.33	0.08	0.01	0.02	0.33	0.24	0.74
	0.30	0.36	0.44	0.00	0.09	0.10	0.67	0.09	0.04
	0.17	0.01	0.01		0.02	0.09	0.66	0.21	0.40
	0.14	0.25	0.27				0.63	0.30	0.30
Mean	0.66	0.78	0.65	0.14	0.20	0.23	0.44	0.18	0.22
Standard Deviation	0.57	0.63	0.43	0.14	0.20	0.19	0.27	0.13	0.24

Peak Systolic Tension Results for Experiments in Specific Aim 3

Table D.14. Average peak systolic tension (PST) for the individual chords in the eight different papillary muscle positions

Papillary muscle position	Anterior strut chord PST(N)	Post. intermediate chord PST(N)	Post. marginal chord PST(N)	Basal Post. chord PST(N)	Ant. Marginal chord PST(N)	Commussural chord PST(N)
000	1.12 ± 0.54	0.34 ± 0.29	0.26 ± 0.24	0.21 ± 0.18	0.36 ± 0.22	0.15 ± 0.21
005	0.59 ± 0.49	0.09 ± 0.08	0.19 ± 0.25	0.08 ± 0.04	0.25 ± 0.09	0.04 ± 0.04
050	1.10 ± 0.69	0.21 ± 0.15	0.21 ± 0.24	0.10 ± 0.06	0.25 ± 0.10	0.05 ± 0.04
055	1.06 ± 0.74	0.20 ± 0.13	0.24 ± 0.24	0.06 ± 0.05	0.28 ± 0.11	0.06 ± 0.04
500	1.42 ± 0.78	0.30 ± 0.22	0.27 ± 0.34	0.29 ± 0.19	0.28 ± 0.13	0.15 ± 0.10
505	0.93 ± 0.87	0.18 ± 0.15	0.19 ± 0.27	0.21 ± 0.07	0.18 ± 0.07	0.26 ± 0.24
550	1.50 ± 0.73	0.53 ± 0.51	0.29 ± 0.36	0.38 ± 0.29	0.22 ± 0.13	0.15 ± 0.10
555	1.52 ± 0.94	0.37 ± 0.36	0.27 ± 0.34	0.24 ± 0.20	0.27 ± 0.19	0.25 ± 0.22

167

Table D.15. Peak systolic tensions (PST) for individual chords in the normal papillary muscle position

Valve Number	Experiment Date	Valve Type	Anterior strut chord PST(N)	Post. intermediate chord PST(N)	Post. marginal chord PST(N)	Basal Post. chord PST(N)	Ant. Marginal chord PST(N)	Commussural chord PST(N)
1	6-Jun	porcine	1.43	0.27	0.50	0.06	0.39	0.07
2	18-Jun	human	1.82	0.27	0.40	0.03	0.63	0.12
3	21-Jun	human	0.85	0.28	0.01	0.22	0.41	0.05
4	9-Aug	human	0.41	0.29	0.51	0.08	0.22	0.14
5	6-Sep	human	0.59	0.52	0.61	0.36	0.78	
6	24-May	porcine	1.32	0.97		0.61	0.13	0.09
7	14-Jun	porcine			0.07	0.06	0.43	0.03
8	28-Jun	human	1.46		0.01	0.25	0.45	0.03
9	7-Aug	porcine	0.32	0.05		0.10	0.09	0.04
10	29-Aug	human	1.65	0.01	0.08	0.19	0.22	0.15
11	30-Oct	human	1.37	0.44	0.13	0.41	0.17	0.74
Mean			1.12	0.34	0.26	0.21	0.36	0.15
Standard Deviation			0.54	0.29	0.24	0.18	0.22	0.21

Table D.16. Peak systolic tensions (PST) for individual chords for papillary muscle position 005

Valve Number	Experiment Date	Valve Type	Anterior strut chord PST(N)	Post. intermediate chord PST(N)	Post. marginal chord PST(N)	Basal Post. chord PST(N)	Ant. Marginal chord PST(N)	Commussural chord PST(N)
3	21-Jun	human	0.32	0.14	0.01	0.14	0.32	0.01
4	9-Aug	human	0.33	0.18	0.48	0.06	0.25	0.04
9	7-Aug	porcine	0.37	0.04		0.06	0.13	0.02
10	29-Aug	human	1.33	0.01	0.08	0.07	0.32	0.09
Mean			0.59	0.09	0.19	0.08	0.25	0.04
Standard Deviation			0.49	0.08	0.25	0.04	0.09	0.04

Table D.17. Peak systolic tensions (PST) for individual chords for papillary muscle position 050

Valve Number	Experiment Date	Valve Type	Anterior strut chord PST(N)	Post. intermediate chord PST(N)	Post. marginal chord PST(N)	Basal Post. chord PST(N)	Ant. Marginal chord PST(N)	Commussural chord PST(N)
1	6-Jun	porcine	1.54	0.25	0.50	0.05	0.29	0.06
2	18-Jun	human	1.79	0.23	0.29	0.02	0.46	0.10
3	21-Jun	human	0.42	0.27	0.02	0.18	0.22	0.02
4	9-Aug	human	0.37	0.44	0.58	0.07	0.23	0.08
7	14-Jun	porcine			0.04	0.04	0.29	0.01
8	28-Jun	human	1.29		0.01	0.15	0.23	0.02
9	7-Aug	porcine	0.41	0.07		0.11	0.12	0.03
10	29-Aug	human	1.90	0.03	0.05	0.15	0.18	0.11
Mean			1.10	0.21	0.21	0.10	0.25	0.05
Standard Deviation			0.69	0.15	0.24	0.06	0.10	0.04

Table D.18. Peak systolic tensions (PST) for individual chords for papillary muscle position 055

Valve Number	Experiment Date	Valve Type	Anterior strut chord PST(N)	Post. intermediate chord PST(N)	Post. marginal chord PST(N)	Basal Post. chord PST(N)	Ant. Marginal chord PST(N)	Commussural chord PST(N)
1	6-Jun	porcine	1.60	0.29	0.55	0.04	0.33	0.08
2	18-Jun	human	1.83	0.25	0.34	0.00	0.48	0.13
3	21-Jun	human	0.40	0.22	0.01	0.15	0.27	0.02
4	9-Aug	human	0.37	0.35	0.47	0.05	0.23	0.07
7	14-Jun	porcine			0.05	0.04	0.32	0.01
9	7-Aug	porcine	0.40	0.06		0.07	0.14	0.03
10	29-Aug	human	1.75	0.02	0.05	0.09	0.18	0.10
Mean			1.06	0.20	0.24	0.06	0.28	0.06
Standard Deviation			0.74	0.13	0.24	0.05	0.11	0.04

Table D.19. Peak systolic tensions (PST) for individual chords for papillary muscle position 500

Valve Number	Experiment Date	Valve Type	Anterior strut chord PST(N)	Post. intermediate chord PST(N)	Post. marginal chord PST(N)	Basal Post. chord PST(N)	Ant. Marginal chord PST(N)	Commussural chord PST(N)
1	6-Jun	porcine	2.03	0.47	0.71	0.13	0.37	0.10
3	21-Jun	human	1.48	0.35	0.01	0.36	0.35	0.15
4	9-Aug	human	0.63	0.53	0.69	0.19	0.24	0.30
7	14-Jun	porcine			0.15	0.08	0.48	0.07
8	28-Jun	human	1.61		0.02	0.61	0.30	0.07
9	7-Aug	porcine	0.39	0.12		0.20	0.09	0.09
10	29-Aug	human	2.37	0.02	0.06	0.44	0.16	0.30
Mean			1.42	0.30	0.27	0.29	0.28	0.15
Standard Deviation			0.78	0.22	0.34	0.19	0.13	0.10

Table D.20. Peak systolic tensions (PST) for individual chords for papillary muscle position 505

Valve Number	Experiment Date	Valve Type	Anterior strut chord PST(N)	Post. intermediate chord PST(N)	Post. marginal chord PST(N)	Basal Post. chord PST(N)	Ant. Marginal chord PST(N)	Commussural chord PST(N)
3	21-Jun	human	0.63	0.22	0.04	0.22	0.24	0.09
4	9-Aug	human	0.51	0.37	0.51	0.13	0.16	0.59
9	7-Aug	porcine	0.36	0.11		0.17	0.08	0.09
10	29-Aug	human	2.24	0.04	0.03	0.30	0.23	0.27
Mean			0.93	0.18	0.19	0.21	0.18	0.26
Standard Deviation			0.87	0.15	0.27	0.07	0.07	0.24

Table D.21. Peak systolic tensions (PST) for individual chords for papillary muscle position 550

Valve Number	Experiment Date	Valve Type	Anterior strut chord PST(N)	Post. intermediate chord PST(N)	Post. marginal chord PST(N)	Basal Post. chord PST(N)	Ant. Marginal chord PST(N)	Commussural chord PST(N)
1	6-Jun		2.04	0.45	0.73	0.14	0.26	0.08
3	21-Jun		1.60	0.38	0.00	0.41	0.35	0.15
4	9-Aug		0.64	0.75	0.76	0.18	0.26	0.29
6	24-May		1.68	1.43		0.96	0.03	0.20
7	14-Jun				0.12	0.07	0.41	0.07
8	28-Jun		1.72		0.03	0.56	0.22	0.05
9	7-Aug		0.40	0.14		0.24	0.09	0.09
10	29-Aug		2.42	0.03	0.08	0.48	0.12	0.29
Mean			1.50	0.53	0.29	0.38	0.22	0.15
Standard Deviation			0.73	0.51	0.36	0.29	0.13	0.10

Table D.22. Peak systolic tensions (PST) for individual chords for papillary muscle position 555

Valve Number	Experiment Date	Valve Type	Anterior strut chord PST(N)	Post. intermediate chord PST(N)	Post. marginal chord PST(N)	Basal Post. chord PST(N)	Ant. Marginal chord PST(N)	Commussural chord PST(N)
1	6-Jun		2.21	0.40	0.72	0.05	0.33	0.10
3	21-Jun		0.72	0.23	0.02	0.24	0.24	0.11
4	9-Aug		0.61	0.48	0.69	0.15	0.22	0.56
6	24-May		1.73	1.12		0.69	0.07	0.24
7	14-Jun				0.13	0.10	0.39	0.06
9	7-Aug		0.37	0.12		0.16	0.11	0.08
10	29-Aug		2.39	0.04	0.06	0.31	0.14	0.24
11	30-Oct		2.62	0.19	0.00	0.19	0.65	0.63
Mean			1.52	0.37	0.27	0.24	0.27	0.25
Standard Deviation			0.94	0.36	0.34	0.20	0.19	0.22

Table D.23. Peak systolic tension (PST) for human valves in the normal papillary muscle position.

Valve Number	Experiment Date	Valve Type	Anterior strut chord PST(N)	Post. intermediate chord PST(N)	Post. marginal chord PST(N)	Basal Post. chord PST(N)	Ant. Marginal chord PST(N)	Commussural chord PST(N)
2	18-Jun	human	1.82	0.27	0.40	0.03	0.63	0.12
3	21-Jun	human	0.85	0.28	0.01	0.22	0.41	0.05
4	9-Aug	human	0.41	0.29	0.51	0.08	0.22	0.14
5	6-Sep	human	0.59	0.52	0.61	0.36	0.78	
8	28-Jun	human	1.46		0.01	0.25	0.45	0.03
10	29-Aug	human	1.65	0.01	0.08	0.19	0.22	0.15
11	30-Oct	human	1.37	0.44	0.13	0.41	0.17	0.74
Mean			1.16	0.30	0.25	0.22	0.41	0.21
Standard Deviation			0.55	0.18	0.25	0.14	0.23	0.27

Table D.24. Peak systolic tension (PST) for porcine valves in the normal papillary muscle position.

Valve Number	Experiment Date	Valve Type	Anterior strut chord PST(N)	Post. intermediate chord PST(N)	Post. marginal chord PST(N)	Basal Post. chord PST(N)	Ant. Marginal chord PST(N)	Commussural chord PST(N)
1	6-Jun	porcine	1.43	0.27	0.50	0.06	0.39	0.07
6	24-May	porcine	1.32	0.97		0.61	0.13	0.09
7	14-Jun	porcine			0.07	0.06	0.43	0.03
9	7-Aug	porcine	0.32	0.05		0.10	0.09	0.04
Mean			1.02	0.43	0.29	0.21	0.26	0.06
Standard Deviation			0.61	0.48	0.30	0.27	0.18	0.03

APPENDIX E:

CD CATALOG

The following appendix contains the file name protocol for CD1. This CD contains the raw data and the processed excel spreadsheets for all the experiments. In addition, this CD contains videos of the mitral valves, and echocardiographic recordings for the experiments in specific aims 1 and 2. All video and echo files are in AVI format.

CD Main Directory

Directory	Description
Videos	This folder contains the video files for the experiments in specific aim 1 and specific aim 2
Processed	This folder contains the excel spread sheets of all the experiments. The excel spread sheets contain the averaged data for mitral flow, trans-mitral pressure and chordal force during one complete cardiac cycle. Each spread sheet has a graph of the different variables against time.
Raw	This folder contains the raw data output from DAQ-ANAL for all the experiments. Each data set stores the measurements of individual variables for ten cardiac cycles.

Video Sub-Directory

This subdirectory is divided into three main folders according to annulus type (flat, saddled, flexible). In each of these folders the files have the following name format:

VX_XXX_XXX.avi

File names have three parts separated by underscores "_".

No.1 "VX" denotes the valve identification number "V1".

No.2 "XXX" denotes the papillary muscle position used in the experiment.

No.3 "XXX" denotes the type of movie: "vid" video images of the valve, "2DE" two dimensional echocardiographic images, and "DOP" color Doppler images.

Processed Sub-Directory

This sub directory is divided into three main folders according to the three specific aims of this study. In each of these folders the files have the following name format:

VX_XXXXX_XXX_XXX.xls

File names have three parts separated by underscores "_".

No.1 "VX" denotes the valve identification number "V1".

No.2 "XXXXX" describes the date on which the experiment was conducted "MAY23".

No.3 "XXX" describes the annulus type used in the experiment: "FLT" flat, "SAD" saddled, and "FLX" flexible annulus.

No.4 "XXX" denotes the papillary muscle position used in the experiment.

Raw Sub-Directory

This sub directory is divided into three main folders according to the three specific aims of this study. In addition, each sub-directory is divided into folders according to annulus type (flat, saddled, flexible). In each of these folders the files have the following name format:

VX_XXXXX

File names have three parts separated by underscores "_".

No.1 "VX" denotes the valve identification number "V1".

No.2 "XXXXX" describes the date on which the experiment was conducted "MAY23".

REFERENCES

1) World Health Organization. The world health report 2002. (http://www.who.int/whr/en/)

2) American Heart Association. Heart disease and stroke statistics Update 2003. (http://www.americanheart.org/presenter.jhtml?identifier=3000090)

3) Kaplan SR, Bashein G, Sheehan FH, Legget ME, Munt B, Ning Li X, Sirvarajan M, Bolson EL, Zeppa M, Martin RW. Three-dimensional echocardiographic assessment of annular shape changes in the normal and regurgitant mitral valve. Amer Heart Jour 2000; 139: 243-250

4) Toumanidis ST, Sideris, DA Papamichael CM, Moulopoulos SD. The role of mitral annulus motion in left ventricular function. Acta Cardiologica 1992;4:331-348

5) Flachskampf FA, Chandra S, Gaddipatti A, Levine RA, Weyman AE, Amelig W, Hanrath P, Thomas JD. Analysis of shape and motion of the mitral annulus in subjects with and without cardiomyopathy by echocardiographic 3-dimensional reconstruction. Am Soc Echocardiogr 2000;13:277-287

6) Madu EC, Baugh DS, Cruz IA, Johns C. Left ventricular papillary muscle morphology and function in left ventricular hypertrophy and left ventricular dysfunction. Med Sci Monit 2001;7(6):1212-1218

7) Tibayan FA, Lai DT, Timek TA, Dagum P, Liang D, Zasio MK, Daughters GT, Miller DC, Ingels NB. Alterations in left ventricular curvature and principal strains in dilated cardiomyopathy with functional mitral regurgitation. J Heart Valve Dis 2003; 12:292-299

8) Gorman JH III, Gorman RC, Jackson Bm, Hiramatsu Y, Gikakis N, Kelley ST, Sutton MG, Plappert T, Edmunds LH. Distortions of the mitral valve in acute ischemic mitral regurgitation. Ann Thorac Surg 1997; 64:1026-31

9) Carabello BA. The mitral valve apparatus: Is there still room to doubt the importance of its preservation? J Heart Valve Dis 1993; 2:250-252

10) Messas E, Guerrero JL, Handschumacher MD, Conrad C, Chow C, Sullivan S, Yoganathan AP, Levine RA. Chordal cutting, a new therapeutic approach for ischemic mitral regurgitation. Circulation 2001; 104:1958-1963

11) Lomholt M, Nielsen SL, Hansen SB, Andersen NT, Hasenkam JM. Differential tension between secondary and primary mitral chordae in acute in-vivo porcine model. J Heart valve Dis. 2002; 11:337-345

12) Bronzino JD. The biomedical handbook. CRC Press, Inc. 1995; Chapter 1, 3-14

13) Guyton AC, Hall JE. Human Physiology and Mechanisms of disease. W.B. Saunders Company 1997; six edition, Chapter 3: 85-114

14) Harjula A. Introduction Lecture to Cardiovascular Hemodynamics -from Modeling to Clinical Application. Inter J of Bioelectromagnetism 2001; Vol.3:Abstract 2 (Finlandhttp://ee.tut.fi/rgi/ijbem/volume3/number2/harjula/)

15) Reul H, Talukder N, Muller EW. Fluid mechanics of the natural mitral valve. J Biomech 1981;14(5):361-372

16) Jensen MO. Stentles mitral valve fixation: impact on hemodynamic performance. M.Sc. Thesis, Department of Biomedical Engineering, Georgia Institute of Technology, USA, 2000

17) Kalmanson D. The mitral valve a pluridisciplinary approach. Publishing science group, Inc. 1976; Chapter 1-5: 3-45

18) He S, Lemmon JD, Weston MW, Jensen MO, Levine RA, Yoganathan AP. Mitral valve compensation for annular dilation: *In vitro* study into the mechanisms of functional mitral regurgitation with an adjustable annulus model. J Heart Valve Dis 1999; 8:294-302

19) Arts T, Meerbaum S, Reneman R. Stresses in the closed mitral valve: A model study. J Biomech. 1983;16:539-547

20) He Z; Sacks MS; Baijens L; Wanant S; Shah P; Yoganathan AP. Effects of papillary muscle position on in-vitro dynamic strain on the porcine mitral valve. J Heart Valve Dis 2003; 12(4): 488-494

21) Sacks MS; He Z; Baijens L; Wanant S; Shah P; Sugimoto H; Yoganathan AP. Surface strains in the anterior leaflet of the functioning mitral valve. Ann Biomed Eng 2002; 30(10): 1281-1290

22) Chester AH, Misfeld M, Yacoub MH. Receptor- mediated contraction of aortic valve leaflets. J Heart Valve Dis 2000; 9: 250-255

23) Timek TA, Miller DC. Experimental and clinical assessment of mitral annular area and dynamics: what are we actually measuring? Ann Thorac Surg 2001; 72:966-974

24) Davis PKB, Kinmonth JB. The movements of the annulus of the mitral valve. J Cardiovasc Surg 1963; 4:427-431

25) Ormison JA, Shah P, Tei C, Wong M. Size and motion of the mitral valve annulus in man. Circulation 1981;64:113-120

26) Pai RG, Tanimoto M, Jintapakorn W, Azevedo J, Pandian NG, Shah PM. Volume-rendered three-dimensional dynamic anatomy of the mitral annulus using transesophageal echocardiographic technique. J Heart Valve Dis 1995; 4:625-627

27) Komoda T, Hetzer R, Uyama C. Mitral annular function assessed by 3D imaging for mitral valve surgery. J Heart Valve Dis 1994; 3:483-90

28) Aikawa K, Sheehan FH, Otto CM, Coady K, Basheim G, Bolson L. The severity of functional mitral regurgitation depends on the shape of the mitral apparatus: A three-dimensional echo analysis. J Heart Valve Dis 2002; 11:627-636

29) Glasson JR, Komeda M, Daughters GT, Niczyporuk MA, Bolger AF, Ingels NB, Miller DC. Three-dimensional regional dynamics of the mitral annulus during left ventricular ejection. J Thorac Cardiovasc Surg 1996; 111:574-585

30) Gorman JH III, Krishanu BG, Streicher JT, Gorman RC, Jackson Bm, Ratcliffe MB, Bogen DK, Edmunds LH. Dynamic three-dimensional imaging of the mitral valve and left ventricle by rapid sonomicrometry array localization. J Thorac Cardiovasc Surg 1996; 112:712-26

31) Gorman JH III, Jackson Bm, Gorman RC, Kelly ST, Gikakis N, Edmunds H. Papillary muscle discoordination rather than increased annular area facilitates mitral regurgitation after acute posterior myocardial infaction. Circulation 1997; 96[suppl II]:124-127,

32) Boltwood CM, Wong M, Shah PM. Quantitative echocardiography of the mitral complex in dilated cardiomyopathy: The mechanism of functional mitral regurgitation. Circulation 1983; 68:498-508,

33) Levine RA, Triulizi MO, Harrigan P, Weyman AE. The relationship of the mitral annular shape to the diagnosis of mitral valve prolapse. Circulation 1987; 75 (IV):756-767

34) Mikami T, Hashimoto M, Kudo T, Sugawara T, Sakamoto S, Yasuda H. Mitral valve and its ring in hypertrophic cardiomyopathy, A mechanism creating surplus mitral leaflet involved in systolic anterior motion. Jap Circ J 1998; 52:597-602

35) Salgo IS, Gorman JH III, Gorman RC, Jackson BM, Bowen FW, Plappert T, Sutton MG, Edmunds LH. Effect of annular shape on leaflet curvature in reducing mitral leaflet stress. Circulation 2002; 106:711-717,

36) Rusted IE, Schiefley CH, Edwards JE. Studies of the mitral valve: I. Anatomical features of the normal mitral valve and associated structures. Circulation 1952; 6,(6):825-831

37) Duran C. Distribution of chordae tendineae tension in the porcine mitral valve. J Heart Valve Dis 2002; 11:335-336

38) Sedransk KL, Allen JG, Vesely I. Failure mechanics of mitral valve chordae tendineae. J Heart Valve dis. 2002; 11:644-650,

39) Liao J, Vesely I. A structural basis for the size-related mechanical properties of mitral valve chordae tendineea. J of Biomech 2003; 36(8):1125-1133.

40) Kunzelman KS, Cochran RP, Verrier ED, Eberhart RC. Anatomic basis for mitral valve modelling. J Heart Valve Dis 1994;3(5):491-496

41) He S, Fontaine AA, Schwammental E, Yoganathan AP, Levine RA. Integrated mechanism for functional mitral regurgitation: leaflet restriction versus coaptation force: in vitro studies. Circulation 1997; 16;96(6):1826-1834

42) Nielsen SL, Nygaard H, Fontaine AA. Chordal force distribution determines systolic mitral leaflet configuration and severity of functional mitral regurgitation. J am Coll Cardiol 1999; 33(3):843-853

43) Nazari S, Carli F, Bnfi C, Aluffi A, Mourad Z, Buniva P, Rescigno G. Patterns of systolic stress distribution on mitral valve anterior leaflet chordal apparatus. J Cardiovasc Surg 2000; 41:193-202

44) He S, Jimenez JH, He Z, Yoganathan AP. Mitral leaflet geometrical perturbations with papillary muscle displacement and annular dilation: An in-vitro study of ischemic mitral regurgitation. J Heart Valve Dis 2003;12(3):300-307

45) Dagum P, Timek TA, Green R, Lai D, Daughters GT, Liang DH, Hayse M, Ingels NB, Miller DC. Coordinate- free analysis of mitral valve dynamics in normal and ischemic hearts. Circulation 2000; 102[suppl III]:III-62-III-69

46) Kunzelman KS, Cochran RP, Chuong C, Ring WS, Verrier ED, Eberhart RD. Finite element analysis of the mitral valve. J Heart Valve Dis 1993;2:326-340

47) He S, Weston MW, Lemmon J, Jensen M, Levine RA, Yoganathan AP. Geometric distribution of chordae tendineae: An important anatomic feature in mitral valve function. J Heart Valve Dis 2000;9:495-501

48) Einstein DR, Kunzelman KS, Reinhall PG, Nicosia MA, Cochran RP. Nonlinear fluid-coupled computational model of the mitral valve. J Heart Valve Dis 2003 (In press)

49) Lembo NJ, Dell LJ, Crawford MH, Miller JF, Richards KL, O'Rourke RA. Mitral valve prolapse in patients with prior rheumatic fever. Circulation 1998; 77(4):830 -836

50) Dagum P, Timek TA, Green R, Lai D, Daughters GT, Liang DH, Ingels NB, Miller DC. Three-dimensional geometric comparison of partial and complete flexible mitral annuloplasty rings. J Thorac Cardiovasc Surg 2001; 11:665-673

51) Glasson JR, Green R, Nistal JF, Dagum P, Komeda M, Daughters GT, Bolger AF, Foppiano LE, Ingels NB, Miller DC. Mitral annular size and shape in sheep with annuloplasty rings. J thorac Cardiovasc surg 1999;117:302-309

52) Nielsen Sl, Timek TA, Lai DT, Daughters GT, Liang D, Hasenkam JM, Ingels NB, Miller DC. Edge-to-edge mitral repair, tension on the approximating suture and leaflet deformation during acute ischemic mitral regurgitation in the ovine heart. Circulation 2001; 104 [supple I]: I-29-I-35

53) Nielsen SL, Nygaard H, Fontaine, Hasenkam JM, He S, Yoganathan AP. Papillary muscle misalignment causes multiple regurgitation jets: An ambiguous mechanism for functional mitral regurgitation. J Heart Valve Dis 1999;8:551-564

54) Kinney EL, Frangi MJ. Value of two-dimensional echocardiographic detection of incomplete mitral leaflet closure. Am Heart J 1985;109:87-90

55) Kaul S, Pearlman JD, Touchstone DA, Esquival L. Prevalence and mechanism of mitral regurgitation in absence of intrinsic abnormalities of the mitral leaflets. Am Heart J 1989;118: 963-972

56) Kaul S, Spotnitz WD, Glasheen WP, Touchstone DA. Mechanism of ischemic mitral regurgitation: An experimental evaluation. Circulation 1991; 84:2167-2180

57) Perloff Jk, Roberts WC. The mitral apparatus. Functional anatomy of mitral regurgitation. Circ 1972; 46:227-239

58) Kono T, Sabbah HN, Rosman H, Alam M, Jafri S, Goldstein S. Left ventricular shape is the primary determinant of functional mitral regurgitation in heart failure. J Am Coll Cardiol 1992; 20:1594-1598

59) Ojtsuji Y, Handshumacher MD, Schwammenthal E, Jiang L, Song JK, Vlahakes Gj, Levine RA. Insights from three-dimensional echocardiography into the mechanism of functional mitral regurgitation: Direct in vivo demonstration of altered leaflet tethering geometry. Circ 1997; 96:1999-2008

60) Gorman JH III, Gorman RC,Plappert T, Jackson B, Hiramatsu Y, St. John-Sutton MG, Edmunds H. Infarct size and location determine development of mitral regurgitation in sheep model. J Thorac Cardiovasc Surg 1998;115:615-622

61) Liel-Cohen N, Guerrero JL, Otsuji Y. Design of a new surgical approach for ventricular remodeling to relieve ischemic mitral regurgitation: insights from three-dimensional echocardiography. Circ. 2000; 101:2756-2763

62) Moanie SL, Guy S, Gorman JH, Plappert T, Jackson B, St. John-Sutton MG, Edmunds HL, Gorman RC. Infarct restraint attenuates remodeling and reduces chronic ischemic mitral regurgitation after postero-lateral infarction. Ann Thorac Surg 2002; 74:444-449

63) Jensen MO, Fontaine, A., and Yoganathan, A.P. Improved In Vitro Quantification of the Force Exerted by the Papillary Muscle on the Left Ventricular Wall Three Dimensional Force Vector Measurement System ABME 2000;10:111-124

64) Friederg CK. Diseases of the Heart. Philadelphia, Saunders Co. 2nd edition 1956: 640pp.

65) Glasson JR, Komeda M, Daughters GT, Bolger AF, MacIsaac A, Oesterle SN, Ingels NB, Miller DC. Three-dimensional dynamics of the canine mitral annulus during ischemic mitral regurgitation. Ann Thorac Surg 1996; 62:1059-68,

66) Athanasuleas CL, Stanley AW, Buckberg GD, Dor V, DiDonato M, Blackstone EH. Surgical anterior ventricular endocardial restoration (SAVER) in the dilated remodeled ventricle after anterior myocardial infarction. J Am Coll Cardiol 2001; 37:1199-1209

67) Soerensen DD, Christensen BN. Chordal force balance effect on mitral valve configuration. B.Sc. Thesis, Faculty of Electrical Engineering, University of Aarhus, Denmark, 2002

68) Nielsen SL. The Impact of Chordal Force Distribution on Functional Mitral Regurgitation – In Vitro Studies. M.Sc. Thesis, Faculty of Health Sciences, University of Aarhus, Denmark, 1999

69) Nichols WW, O'Rourke MF. The nature of flow of a fluid, in Nichols WW, O'Rourke MF (eds): McDonald's Blood flow in arteries. Theoretical, experimental and clinical principles. Philidelphia, Lea & Febiger 1999: 12-53.